A Novel Wideband 140 GHz Gyrotron Amplifier

by

Colin D. Joye

M.S. (EECS), Massachusetts Institute of Technology (2004)

B.S. (ECE), Villanova University (2002)

Submitted to the
Department of Electrical Engineering and Computer Science
in partial fulfillment of the requirements for the degree of

Doctor of Philosophy in Electrical Engineering

at the

MASSACHUSETTS INSTITUTE OF TECHNOLOGY

September 2008

Author .....
Department of Electrical Engineering and Computer Science
August 1, 2008

Certified by .....
Richard J. Temkin
Senior Research Scientist, Department of Physics
Thesis Supervisor

Certified by .....
Jagadishwar R. Sirigiri
Research Scientist, Plasma Science and Fusion Center
Thesis Supervisor

Accepted by .....
Professor Terry P. Orlando
Chairman, Committee on Graduate Students
Department of Electrical Engineering and Computer Science

A Novel Wideband 140 GHz Gyrotron Amplifier

by

Colin D. Joye

M.S. (EECS), Massachusetts Institute of Technology (2004)

B.S. (ECE), Villanova University (2002)

Submitted to the Department of Electrical Engineering and Computer Science
on August 1, 2008, in partial fulfillment of the
requirements for the degree of
Doctor of Philosophy in Electrical Engineering

Abstract

The theory, design and experimental results of a wideband 140 GHz, 1 kW pulsed gyro-traveling wave amplifier are presented. The gyro-TWA operates in the HE(0,6) mode of a novel cylindrical confocal waveguide using a gyrating electron beam. The electromagnetic theory, interaction theory, design processes and experimental procedures have been described in detail. The experiment has produced over 820 W peak power, 34 dB linear gain, and a -3 dB bandwidth of over 1.5 GHz (1.1%) from a 37 kV, 2.7 A electron beam having a beam pitch factor of 0.6, radius of 1.9 mm and calculated perpendicular momentum spread of approximately 9%. The gyro-amplifier was nominally operated at a pulse length of 2 microseconds, but was tested to amplify pulses as short as 4 nanoseconds with no noticeable pulse broadening. Internal reflections in the amplifier were identified using these short pulses by time-domain reflectometry. A novel internal mode converter was designed for this device that transforms the confocal HE(0,6) fields into a fundamental Gaussian beam for ultra-low loss transmission of the millimeter wave output power through a corrugated transmission line. The demonstrated performance of this amplifier shows that it can be applied to Dynamic Nuclear Polarization (DNP) and Electron Paramagnetic Resonance (EPR) spectroscopy.

Thesis Supervisor: Richard J. Temkin
Title: Senior Research Scientist, Department of Physics

Thesis Supervisor: Jagadishwar R. Sirigiri
Title: Research Scientist, Plasma Science and Fusion Center

Acknowledgments

A great deal of my academic, personal and spiritual development I attribute to my time at MIT. While in Cambridge, I took up interest in musical instruments from around the world, even taking lessons on drums from India and Nigeria. I learned Korean and married my wonderful wife, Hyun Young ("Heidi"), from Busan, South Korea. Together, we traveled to Korea, Japan, Slovakia, Austria, Czech-Republic, Mexico, and the Philippines. I led and co-led a few Bible studies on campus. I maintained the historic pipe organ at the First Korean Church of Cambridge where we both taught Sunday school, tuned its over 1,300 pipes, and held a concert and seminar. I developed my abilities to improvise in the jazz style on the piano. I took up an interest in photography. But most importantly, I committed myself to a body of work worthy of the title Doctor of Philosophy that has taught me skills that transfer to many aspects of life, in addition to giving me a career direction.

I am most grateful to my Lord and Savior, Jesus Christ, without whom all of my labor is without meaning. Throughout all of my difficult days at MIT, many of which started before 5:00 AM with prayer, God was the only one I could turn to for my daily strength. My whole existence belongs to God and for His grace and mercy, I am eternally thankful. I pray that the MIT Graduate Christian Fellowship might continue to enrich the lives of grad students for decades to come.

Secondly, I'd like to thank my parents, Dr. Donald and Claudia Joye, who educated my brothers (Gavin and Chris) and I for twelve years each at home so we could learn the values and virtues not taught in the schools. They sacrificed much of their time and comfort to help us and several hundred other homeschooling families bring their children up in the way they thought was best. I'd also like to thank Heidi's parents, Yong Won and Eun Sook Kang for their unceasing prayers during this time.

From my lab, I'm deeply grateful to my advisor, Dr. Rick Temkin, for walking with me through thick and thin, as well as Dr. Jagadishwar Sirigiri who provided much help on this project and is gifted with the ability to make things work and Dr. Michael Shapiro for his skills and insights in electromagnetics and mode conversion.

Contents

List of Figures

List of Tables

Chapter 1

Introduction

1.1 Millimeter Wave Applications

The entire electromagnetic spectrum encompasses an astounding amount of modern-day technologies. From the inception of AM radio (around 1 MHz) and television receivers (100s MHz) in the early twentieth century to the rise of the cellular phone in the 1990s (900 MHz to 2.4 GHz), and more recently to wireless personal networks (60 GHz), the generation, transmission and detection of electromagnetic waves has grown to lead a ubiquitous role in our daily lives. We use infrared lasers to transmit information over vast distances via fiber-optic cable at extremely high data rates, and X-ray security scanners are mandatory at virtually every airport in the world.

Until recently, there has been a paucity of sources capable of generating electromagnetic power from about 100 GHz to 100 THz. This phenomenon has been known as the terahertz (THz) gap. Across the electromagnetic spectrum there has been virtually no deficiency of sources except in this range. Recently, as sources and techniques became available, it became clear that a large number of potential applications were hidden exactly in those missing bands. The band from approximately 30 GHz to 300 GHz is known as the millimeter wave (MMW) band because the wavelength of the electromagnetic wave is on the order of a millimeter. Likewise, sub-millimeter waves occupy the band from 300 GHz to perhaps a few THz.

One can now imagine a dental imaging device that could provide a harmless

alternative to X-rays using THz radiation, or "T-rays" [1, 2]. Such an imaging method would break through the traditional practice of taking an X-ray photo and later following it by a procedure; instead, a procedure could be performed while THz imaging simultaneously reveals the actual progress on a monitor. THz technology is now being used to inspect critical components for defects in NASA systems [3]. It has also been done with MMW [4].

An order of magnitude improvement in resolution was reported for the MIT Lincoln Labs Haystack ultra-wideband satellite imaging radar after the addition of 94 GHz gyro-amplifier tubes [5], clearly illustrating the potential for high power MMW devices in long range imaging applications.

Airport security systems utilizing everything from MMW to infrared are becoming more popular alternatives to pat-searching and give much more information than the metal detector. L-3 Communications released a MMW scanner capable of revealing hidden weapons in under 2.5 seconds [6]. Many other MMW-based security systems have been developed for stand-off weapons detection [7], and for biological and chemical agent detection [8].

Wide bandwidth satellite communications are dominated by high-efficiency Traveling Wave Tube (TWT) vacuum electron devices [9, 10]. At higher frequencies, not only is more bandwidth available, but the dimensions of the antenna required decrease in proportion to the wavelength, leading to smaller, more efficient satellites. In the MMW range, there is moderate atmospheric absorption in general above 35 GHz [11], with transparent windows at 94 GHz and 220 GHz [12]. Higher frequencies in the THz suffer from strong absorption due to water, so the MMW frequency range may well be the final frontier as far as satellite communications are concerned.

Research has exploded into fields such as radar [13], target tracking, imaging [14], cloud physics [15, 16], spectroscopy experiments utilizing Dynamic Nuclear Polarization (DNP) [17, 18, 19], ceramics sintering [20], biomedical applications [21], and the military Active Denial System [22]. A gyrotron operating with a pulsed 21 T magnet has recently broken the 1 THz frequency barrier using the second harmonic of the cyclotron frequency [23].

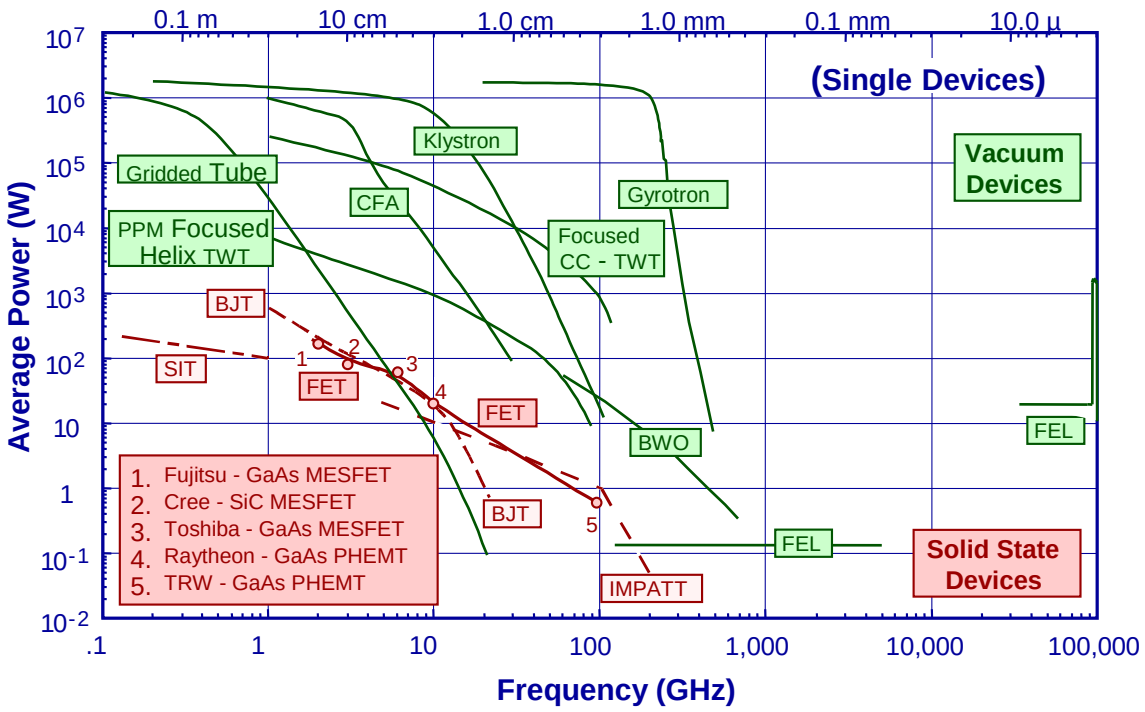

Figure 1-1: Recent advances in vacuum electron device technology showing gyro-devices pushing the frontier to higher power and higher frequency. *(Courtesy of Bruce Danly, NRL)*

1.1.1 Available MMW Sources

Fig. 1-1 is a graph showing the frontiers of available source technologies in terms of the average output power and frequency [24]. Among the competitors for the microwave band are conventional microwave tubes such as klystrons, magnetrons, traveling wave tubes (TWTs), backward-wave oscillators (BWOs) and other linear beam slow-wave devices. In the millimeter band, the competition thins out, leaving only gyro-devices to push the frontier curve into the THz gap at higher average power. BWO's have successfully demonstrated 10's of milliwatts of peak output power in the 600-650 GHz range recently [25], which is a very promising advance, but still orders of magnitude below what a gyro-device could be capable of producing. Non-relativistic orotrons [26] and even some solid state devices [27] are capable of producing small amounts of power at the millimeter wavelengths, but currently produce only very small amounts of radiation at the sub-millimeter wavelengths. Accelerator-based relativistic sources, such as relativistic orotrons, have also been used to produce very high peak power millimeter-wave and THz radiation for ultra-short pulse applications [28], but are limited to low average powers. The large size and high complexity of these kinds of sources are likely to limit them to specialized facilities.

1.2 Spectroscopy at MIT

The MIT Francis Bitter Magnet Laboratory (FBML) has been a world leader in Dynamic Nuclear Polarization enhanced Nuclear Magnetic Resonance (DNP/NMR), Electron Paramagnetic Resonance (EPR) and other spectroscopy techniques [29]. Moderate power continuous-wave (CW) gyrotron oscillators have been used to polarize the electrons in a solution containing free radicals [30]. The electron polarization is transferred to the nucleus and results in signal-to-noise enhancement factors of 50-400 [31, 32].

Table 1.1: MIT Gyrotrons for DNP

Source	140 GHz [33, 34]	250 GHz [19]	460 GHz [36]
CW Power	14 W	8 W	16 W
Operating mode	$TE_{0,3,1}$	$TE_{0,3,2}$	$TE_{11,2,1}$
Beam voltage	12.2 kV	12.2 kV	13.0 kV
Beam Current	32 mA	25 mA	100 mA
Magnetic Field	5.12 T	9.16 T	8.42 T

1.2.1 Gyrotron-based DNP Experiments

The current DNP/NMR 140 GHz test bed at the FBML consists of a 140 GHz fixed-frequency gyrotron oscillator, waveguides, a DNP probe and another superconducting magnet. The gyrotron delivers up to approximately 14 W in the TE_{01} mode at the gyrotron output. This power is transformed to the TE_{11} mode by a snake mode converter before it propagates down straight copper pipes [33, 34]. Two 90^o miter bends exist before the oversized waveguide is tapered down to fundamental waveguide. The total losses were measured previously to be approximately 6.4 dB with theoretical losses totaling 3.7 dB [35]. At the probe, approximately 1 to 2 watts of power is delivered into the sample.

In addition to this 140 GHz gyrotron oscillator, a second gyrotron oscillator operating at 250 GHz (380 MHz nuclear frequency) has been in operation since 1998 [37], with hundreds of hours of non-stop CW operation time to date. This gyrotron is also used to run NMR spectroscopy experiments. The 250 GHz gyrotron oscillator operates in the fundamental TE_{03} mode at 9.2 T from a 12 to 16 kV electron beam, and is capable of generating up to 25 W CW at 250 GHz at an efficiency of 4% [19].

A 460 GHz, second harmonic gyrotron oscillator [36, 38, 39] has been rebuilt for better performance and preliminary measurements indicate that it is now capable of over 16 W CW power from a 13 kV, 100 mA beam with very stable operation in the $TE_{11,2}$ mode. It uses an 8.4 T magnetic field at the second cyclotron harmonic to save construction costs on the superconducting magnet. It will be used for sub-millimeter wavelength spectroscopy experiments with a 700 MHz nuclear frequency. A table of the operating parameters of these three gyrotrons is given in Table 1.1.

1.2.2 Short-pulse DNP/NMR Spectroscopy

Modeled after these DNP/NMR experiments that use a gyrotron oscillator, a new short-pulse EPR experiment will be installed utilizing the 140 GHz gyro-TWT amplifier described in this thesis. A series of amplifiers is envisioned at 250 GHz and 460 GHz following the success of the 140 GHz EPR system, thus scalability is a desirable feature of this work. This amplifier should deliver 100 W in the form of a fundamental HE_{11} mode into a low-loss corrugated waveguide line. The amplifier features ease of frequency tunability, where previously only a single frequency was possible, and it also allows for wide-band, nanosecond-scale short pulses to be sent to the samples for short pulse EPR measurements.

High magnetic fields are needed in spectroscopy to efficiently separate chemical shifts, but this means the spectra of the radical solutions can easily be several hundred MHz wide. A short pulse of 1 ns allows the entire enhanced radical spectrum to be measured at once. Additionally, it is estimated that such a 1 ns pulse will achieve polarization an order of magnitude faster than CW radiation techniques, thus 2-D chemical shift maps become rather easy to generate. A pulsed experiment using a MMW amplifier permits phase, frequency, pulse duration and amplitude modulations, giving new dimensions of control to the spectroscopy.

Current pulsed EPR is performed at the FBML using a 30 mW IMPATT diode, but to achieve enhancement, the pulse length is 50 ns, too broad to capture the entire radical spectrum by itself. By decreasing the pulse length and lowering the spectrometer cavity Q, wider bandwidth pulses are generated, but this requires an increase in pulse power. It is estimated that approximately 100 W at 1 ns will achieve the desired effects at 140 GHz. So far, only a gyro-amplifier is capable of meeting these goals. No amplifier is presently available commercially or otherwise to fulfill these needs, therefore it is the aim of this thesis to provide such a device.

There is another device called the Extended Interaction Klystron (EIK) that is capable of generating peak powers of up to 50 W at even 220 GHz, but these devices generally suffer from limited average power and lifetimes estimated at only 1,000

hours, whereas the gyrotron lifetime is expected to exceed 100,000 hours. The EIK is also not scalable to the higher frequencies of 250 GHz and 460 GHz and is therefore not an attractive solution compared to the legacy of the gyro-amplifier. Thus the gyro-amplifier is chosen as the best solution for this application.

1.3 Overview of Gyro-Devices

The gyro-Traveling Wave Amplifier (gyro-TWA) is a high frequency vacuum electron device used to amplify millimeter wavelength electromagnetic waves to higher power levels. The gyro-TWA is part of a larger class of gyro-devices that utilize the electron cyclotron resonance maser (CRM) instability to extract energy from helically gyrating electrons in a cavity supporting a particular electromagnetic mode. The possibility of an electron beam interacting with an electromagnetic wave to produce gain was known by the end of the 1950s, laying the foundation for all gyro-devices [40, 41, 42]. In particular, the gyrotron oscillator research that has been going on since the 1970s has focused primarily on applications for plasma heating in the millimeter band range of 28 GHz to 170 GHz, at power levels typically greater than hundreds of kilowatts and up to tens of megawatts [43]. The recent demonstration of a gyro-amplifier capable of 10 kW average power (92 kW peak power) at 33 dB gain [44] has fueled development of these devices, particularly for radar applications.

In gyro-devices, a weakly relativistic ($\gamma \lesssim 1.25$) electron beam gives up energy to millimeter-wave (MMW) electromagnetic fields in the cavities where the electrons emit or absorb radiation as they experience forces from the electromagnetic fields. The term *fast wave* comes about because the phase velocity of the electromagnetic wave in the interaction structure is faster than the speed of light. In this regime, the cavity structures are typically several wavelengths in each dimension and the energy is extracted from the perpendicular component of the electron momentum. In contrast, the interaction structure of the slow wave device keeps the MMW phase velocity below the speed of light by features a fraction of a wavelength in size so that the electrons travel in near synchronism with the MMW fields. When this happens,

electromagnetic radiation is emitted by interaction with the parallel component of the electron's velocity instead of the perpendicular component. The tiny features required to slow the MMW phase velocity severely restrict the allowable power density. In both slow wave and fast wave devices, the transverse dimensions of the interaction structure scale inversely with frequency, which limits the power that can be safely generated in the structure due to the increased ohmic losses. Fast wave devices can, however, operate in higher order modes very efficiently. This allows the dimensions of the interaction structures to be larger, making it possible to generate higher power while limiting the thermal losses in the structure. The efficiency of slow wave devices is generally poor at higher order modes and thus the fast wave devices have a distinct advantage at the millimeter wave frequencies and above.

In the typical gyro-device, an electron beam is emitted from an indirectly heated cathode and guided along a precision magnetic field through a single cavity, series of cavities, or a long gyro-TWA section. The electron beam consists of many electrons gyrating around the magnetic field lines in a small helix with a cyclotron frequency near the operating frequency of the device (or a integral multiple harmonic thereof) as they traverse the tube from the cathode side of the tube to the collector side. These small helicies are densely packed around the azimuth of a larger hollow annular beam.

If the Larmor orbits of the electrons are smaller than the guiding center radius (average radius of the hollow annulus), then the device is called a small orbit device. On the other hand, if the Larmor radius is greater than or equal to the guiding center radius, the device is said to be a large orbit device. A small orbit beam can be easily generated by a Magnetron Injection Gun (MIG); and this is the type of beam being utilized in this work. The generation of a large orbit beam is more complicated and is usually achieved by imparting a kick to a linear beam by either a magnetic cusp or a microwave kicker [45]. Such devices are theoretically capable of higher efficiency and operation at high harmonics [46], but the generation of the electron beam poses significant challenges.

Energy is extracted in the gyrotron interaction by the relativistic cyclotron resonance maser instability in which the weakly relativistic electrons are phase bunched

in the azimuthal direction due the MMW fields. The bunches grow in the presence of the interaction circuit, and if the operating frequency is slightly higher than the cyclotron frequency of the electrons, the bunches end up in the decelerating phase of the electromagnetic fields and give up energy to them [47]. Only the transverse energy is extracted from the electron beam during a CRM fast wave interaction, hence an electron beam with significant transverse energy is chosen in a gyrotron device. Typically the *pitch factor*, the ratio of the transverse velocity to the longitudinal velocity of an electron beam varies from 0.5 to 2.0 and is given the symbol α. At α-values below 0.5, there is simply not enough energy available to overcome losses; while at values above 2.0, the electron beam tends to reflect due to a lack of axial energy, which is needed to overcome the steep magnetic hill caused by the beam compression.

At the end of the interaction, the beam has lost a significant amount of its original energy to the MMW fields in the cavities and is collected by a thermally cooled collector. In the case that the duty cycle of the device is very low, it is not necessary to cool the collector. The remaining amplified MMW fields are extracted from the tube and sent through waveguides to the desired application. The particular variation of the interaction circuit falls into several categories [48]:

1.3.1 Gyrotron Oscillator

The gyrotron oscillator consists of a short cylindrical resonant cavity section bounded on either side by a downtaper and uptaper (Fig. 1-2a). The downtaper functions to prevent the electromagnetic power from leaking toward the electron gun region. The energy is extracted from the uptaper section and often sent through an internal mode converter to transform the complicated high order mode into a fundamental Gaussian beam for low loss transmission in high power gyrotrons [49]. High power gyrotrons usually operate in a high order mode, such as the $TE_{22,6}$ mode so that a larger cavity and electron beam diameter may be used. The larger cavity reduces the problem of ohmic heating of the cavity walls, and the larger electron beam reduces the problem of space charge associated with high beam currents [50]. The gyrotron oscillator is generally not tunable over a wide range due to the high Q-factor of the cavity. Due

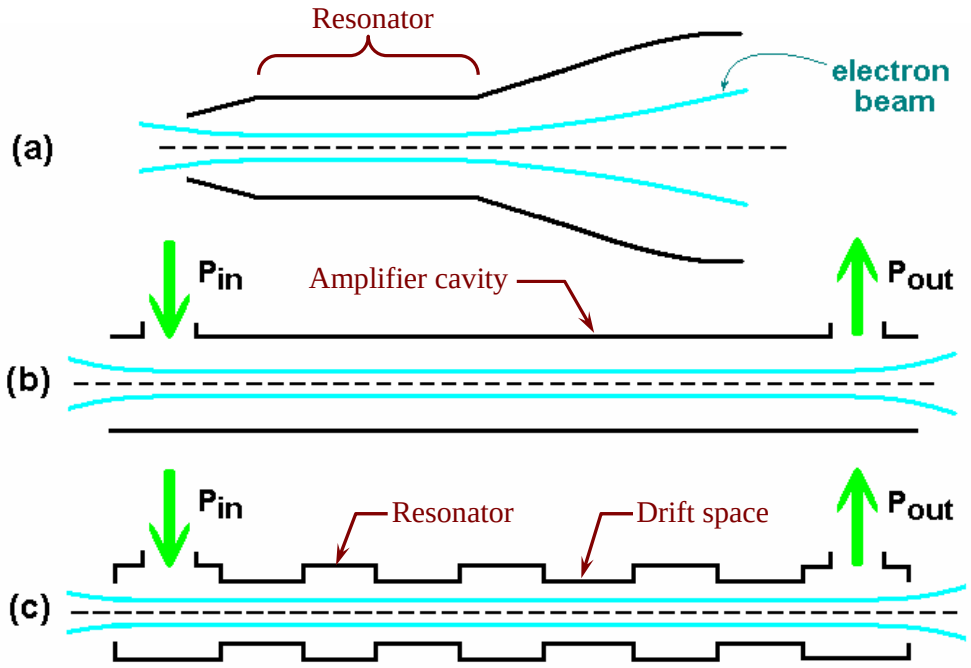

Figure 1-2: Common gyro-device cavity profiles with an electron beam: (a) gyrotron oscillator; (b) gyro-TWT; (c) gyroklystron.

to the large number of modes an overmoded gyrotron cavity can support, however, there has been interest in step-tunable gyrotrons [51, 52].

1.3.2 Gyro-TWA

The gyro-TWA amplifies MMW via a focused electron beam traveling through an interaction circuit that supports a specific electromagnetic mode. It is the fast wave extension of the traveling wave tube (TWT), which is a slow wave device used for generating microwaves. The gyro-TWA (also referred to as a gyro-TWT or gyro-TWTA) is known for its wide bandwidth, moderate efficiency and ability to provide high power in a frequency band that is out of reach for both slow wave and laser devices

Gyro-TWAs (Fig. 1-2b) are capable of very high gain and large bandwidth due to a near matching of the waveguide mode and cyclotron mode and because the group velocity is very close to the electron beam velocity. The interaction structure

is most simply a waveguide with no resonant structures, so the bandwidth can be quite large. Velocity spread in the electron beam is typically the limiting factor for how long a structure can be. The gyro-TWT often suffers from problems with instabilities and self-oscillation due to spurious backward waves, although the more recent use of heavily-loaded, lossy TWT waveguides was found to be a good way of controlling these problems [53, 54, 55]. Gyro-TWTs have not been built at very low beam voltages because gain, bandwidth and output power reduce rapidly with decreasing beam power.

This gyro-TWA experiment makes use of a diffractive loss mechanism to stabilize against oscillations while completely avoiding the need for expensive, fragile and often temperature-sensitive lossy ceramic materials. The geometry of the confocal system is shown in Fig. 1-3. The large gap on either side of the waveguide lowers the total Q by diffraction, allowing the amplifier to be stabilized without ceramic loading. In addition, the diffractive losses from the open sidewalls suppresses lower-order modes. Thus the confocal structure in a gyro-TWA allows operation in higher-order modes without mode competition. This in turn allows the use of an interaction structure with larger transverse dimensions and hence higher power handling capability. The all-copper circuit is very attractive for devices that must run in CW mode and, in principle, it could be tuned mechanically in vacuum. On the down side, part of the annular electron beam sees no RF fields, so efficiency is lower than the full cylindrical gyro-TWA (that is, until a confocal electron gun is built!). The confocal gyro-TWA was first successfully demonstrated at MIT and achieved 30 kW output power and 29 dB gain at 70 kV and 4 A [56, 57].

The current state of the art for gyro-TWAs is shown in Table 1.2 for fundamental devices. Several advances in the gyro-TWA field include: A wide bandwidth W-band gyro-TWT [58], an ultra-high gain W-band lossy wall gyro-TWT [59], the use of helically corrugated interaction circuits to widen bandwidth and increase output power [60], theory for a vane-loaded gyro-TWT [61], and an ultra-high bandwidth Ka-band gyro-TWT [62]. A 30 kW confocal gyro-amplifier at 140 GHz was demonstrated at MIT by Dr. J. Sirigiri [57], which achieved 29 dB gain and over 2 GHz bandwidth

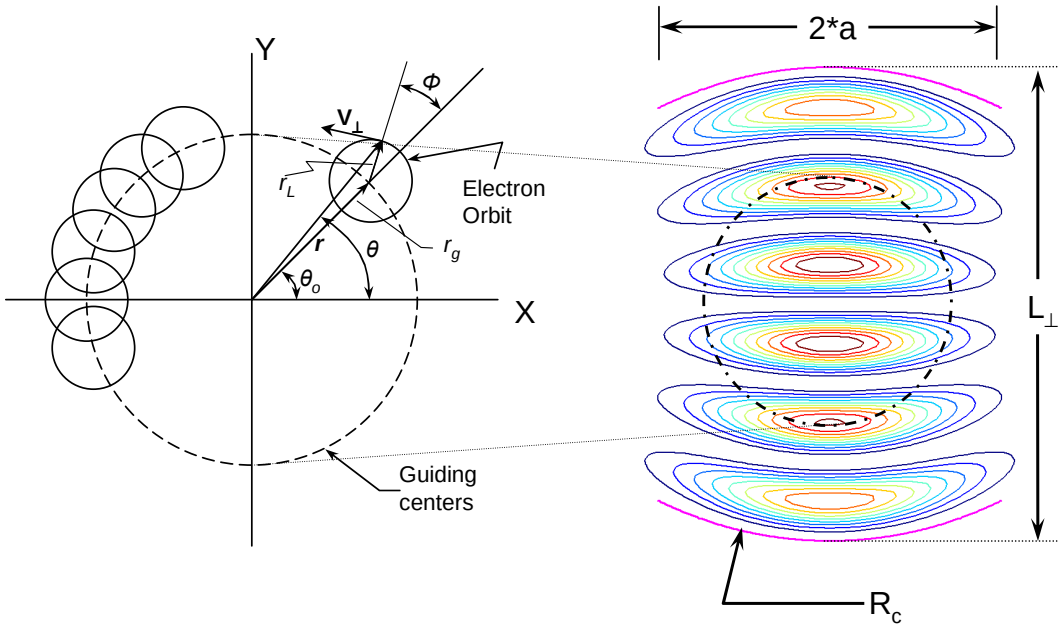

Figure 1-3: (left) Geometry of the electron beam showing guiding center beam radius r_g and Larmor radii r_L. (right) Confocal interaction geometry showing mirror aperture half-width a, radii of curvature R_c and mirror separation $L_\perp$ with power contours for the HE_{06} mode superimposed. Transverse electric field vectors are also shown. The electron beam interacts primarily with the second and fourth maxima.

Table 1.2: Gyro-TWT Achievements

Source	Mode	V_0[kv]	I_0[A]	P_o[kW]	eff	f_0[GHz]	BW[GHz]	$gain$[dB]
CPI [58]	TE_{01}	30	1.8	1.5	3%	95	7.3 (7.4%)	>43
UCD [59]	TE_{01}	91	7.0	140	22%	94	>2 (2%)	61
NRL [62]	TE_{01}	33	1.6	6	11%	35	11 (33%)	20
NRL [63]	TE_{01}	70		3.2	1.5%	35	0.7 (2%)	42
NTHU [64, 65]	TE_{11}	100	3.5	93	26.5%	35	3.0 (8.6%)	70
MIT, 2003 [57]	HE_{06}	70	4.0	30	12%	140	2.3 (1.6%)	29
MIT, 2008	HE_{06}	37	2.7	0.82	1%	140	1.5 (1.1%)	34

from a 70 kV, 4 A electron beam. The present work builds on that success, but faces major new challenges since the amplifier must operate at lower beam power (37 kV, 2.7 A versus 70 kV, 4 A), while still providing high bandwidth and gain.

1.3.3 Gyroklystron

A gyroklystron consists of a series of nearly isolated prebuncher cavities, each of which bunches the electrons such that gain occurs in each cavity (Fig. 1-2c). In theory, the gyroklystron can have as much as 18 dB of power gain per cavity in the linear regime [66], lending gyroklystron devices to relatively short circuits. A small RF signal is coupled into the first cavity, then amplified in each cavity and finally extracted at the end. Gyroklystrons typically have very good linearity, less sensitivity to velocity spread and can have fairly wide bandwidth even at low beam voltages. Since the gyroklystron typically has a more narrow bandwidth than the gyro-TWT, it is also less noisy. This device, however, is more difficult to build, since several cavities have to be tuned very accurately and the alignment of the cavities with the electron beam can be difficult. Furthermore, the drift spaces, where ideally no fields exist, are susceptible to a plethora of modes and resonances in practice.

A common method for adjusting the Q factor of each cavity in the gyroklystron is to use lossy ceramics. However, other possibilities exist, such as lossy tunable slots in the cavity that would lower the Q by diffracting some power out. Large slots could be used in the drift sections to allow the fields to leak out and be absorbed by larger lossy ceramics. Lossy ceramics have been readily characterized at 35 GHz and

94 GHz, but there is little data available at 140 GHz or higher frequencies.

The gyroklystron could be a good choice for a low-voltage tube, because the gyroklystron provides a series of cavities that can be tuned to different resonant frequencies to widen the bandwidth at the expense of amplifier gain, a method known as stagger tuning [67]. The cluster cavity [68] technique can theoretically widen the bandwidth without losing gain if the cavities are uncoupled, but this has yet to be achieved in practice. Some recent gyroklystron design advances and variations include a dual-cavity coaxial gyroklystron [69], a third-harmonic gyroklystron [70], and sub-millimeter second-harmonic designs [71]. In addition, many advances have been made in the theory of gyroklystrons, such as the optimization of gyroklystron efficiency [66], AC space charge analysis [72], the effects of penultimate cavity position and tuning [73], the theory of stagger tuning [74], and the calculation of phase shifts in gyroklystron amplifiers [75].

1.3.4 Gyrotwystron

A gyrotwystron is a hybrid device consisting of a gyroklystron section followed by a gyro-TWT section. Utilizing this configuration rather than a plain gyroklystron alone, higher bandwidth can be achieved. Another version is the inverted gyrotwystron, where the traveling wave section appears first. The gyrotwystron is typically more susceptible to oscillations than the gyroklystron. A W-band, 5-section gyrotwystron operating in the TE_{01} mode was recently demonstrated [76].

1.3.5 Gyro-BWO

In a gyro-BWO, the output frequency is directly adjusted by the operation voltage, but higher magnetic fields are required for the gyro-BWO than for other gyro-devices because of a negative Doppler shift, making the gyro-BWO less desirable at very high frequencies. Gyro-BWOs also suffer from a relatively low efficiency and low output power. A gyro-BWO would not likely be capable of meeting the requirements for nanosecond-scale pulses due to the difficulties associated with switching high voltage

electron beams on and off at such short timescales.

1.4 Motivations for the Gyro-TWA

Since the gyro-TWA being described in this thesis will be incorporated into short-pulse electron paramagnetic resonance (EPR) spectroscopy measurements, it is important that it be capable of amplifying nanosecond-scale short pulses. The short-pulse capability requires a fairly wide bandwidth and a high amount of phase stability [77]. The gyro-TWA is inherently capable of wide bandwidth, high gain, short pulses and high phase stability. The phase stability performance of a gyro-TWA is limited almost entirely by the flatness of the voltage pulse that the power supply can generate. In addition, this amplifier is the first in a series of amplifiers proposed at successively higher frequency as upgrades to the current oscillator-based 140, 250 and 460 GHz systems. The operating principle of this amplifier is scalable to higher frequencies, whereas other approaches, such as slow-wave devices, would not be able to scale with frequency at the required power levels and thus not meet the needs of the system. The prime candidate for meeting all of these requirements is the gyro-TWA. A table of the requirements is given in Table 1.3.

There are significant challenges presented in the demonstration of this amplifier. First, no gyro-amplifiers have been built at this frequency to achieve a gain of 40 dB or more from a low-power electron beam. Gain, bandwidth, and efficiency are all adversely affected by low beam voltage and current, and for this reason it is not a trivial task to meet the requirements at low beam power. Second, the use of a high-order mode brings with it several new challenges including mode competition, oscillations, and problems with misalignment; but it also brings the ability to filter out unwanted modes, tune in vacuum and stabilize the amplifier without ceramic absorbers. In principle, this all-copper structure could run in continuous-wave (CW) mode because there are no lossy absorbers. Ceramic absorbers are prone to overheating in high power applications and to shifts in their electrical properties as they heat up. An overmoded, all-copper amplifier is therefore an extremely attractive solution for high

Table 1.3: Gyro-TWT Specifications

Maximum output power	>100 W peak
Minimum pulse width	1 ns
Minimum Bandwidth	1 GHz
Saturated gain	40 dB

power and high frequency applications. In addition, there is limited ceramic absorber characterization at 140 GHz and above, requiring a trial-and-error process of finding and measuring the right materials before the design process can even begin. The ability to create an amplifier devoid of lossy ceramics completely sidesteps these difficult issues.

1.4.1 Novel Features of this Design

The physics challenges associated with the construction of the gyro-TWA are maintaining high gain and wide bandwidth at the lowest possible electron beam voltage and current. The desire to use low voltage is driven in part by power supply simplicity and lab safety, and in part to maintain efficiency at reasonable levels in the 1 kW output power range. In particular, high gain is difficult to achieve due to feedback oscillations, resonances in the transmission lines and electromagnetic losses in the system. Amplifier stability is important to ensure that future EPR measurements run smoothly. Modern techniques such as loading the amplifier walls with ceramic absorbers [64] are not available due to a lack of materials characterization at frequencies as high as 140 GHz, adding to the challenge of stabilizing the amplifier. Short pulses present several hurdles due resonances and echoes that must be kept to a minimum.

1.4.2 Fundamentals of the Gyro-TWA Operation

A sketch of the essential components in this gyro-TWA is shown in Fig. 1-4. At one extreme of the vacuum tube, an indirectly heated cathode ring in the electron gun emits an annular beam of electrons by thermionic emission. The electrons adiabatically spiral around the magnetic field lines created by the magnet. The Larmor radius

of this spiral is determined by the local axial magnetic field and the relativistic mass of the electrons. The electrons are initially randomly distributed in phase over the range $(0, 2\pi)$ and are assumed to produce a uniform current density over the area of the annular ring, which has a radius of approximately 1.9 mm in the center of the magnet.

The interaction circuit consists of a long region supporting an electromagnetic mode to interact with the electron beam. The operating mode and electron beam geometry were shown in Fig. 1-3. In addition, the circuit is stabilized against self-oscillations by a diffractive loss mechanism. As the electron beam enters the beginning of this circuit, the electric field produces a force on the electrons as they spiral around the magnetic field lines. This force not only changes the phase of the electrons as their orbits are slowed down and sped up, but it alters the perpendicular momentum of the electrons in a relativistic manner, resulting in a non-uniformly distributed electron density through the process of bunching. In this process, a majority of electrons are made to gyrate coherently thus driving the fluctuating current density term in Maxwell's equations and efficiently transferring energy from the electrons to MMW fields.

As the electron beam travels down the long interaction circuit, this bunching effect grows, amplifying the electric fields. A beam that is more highly bunched becomes a larger source of fluctuating current and hence gives up more of its energy to MMW. Eventually, the electrons lose so much energy by loss of relativistic mass that their cyclotron frequency shifts and they no longer interact. Energy is no longer efficiently extracted from the beam and nonlinear saturation has set in. However, if the beam is allowed to evolve too long, or if the bunching process is forced too strongly, an overbunching may result in which the electrons again take energy from the fields in the circuit, resulting in a dramatic efficiency drop.

Finally, the spent electron beam is collected by a copper collector pipe, where the beam dissipates on a smooth wall. Since the average power is very low, no water cooling is needed. The MMW power propagates out of the interaction circuit and travels down the cylindrical collector pipe in a TE_{03}-like mode, and then passes

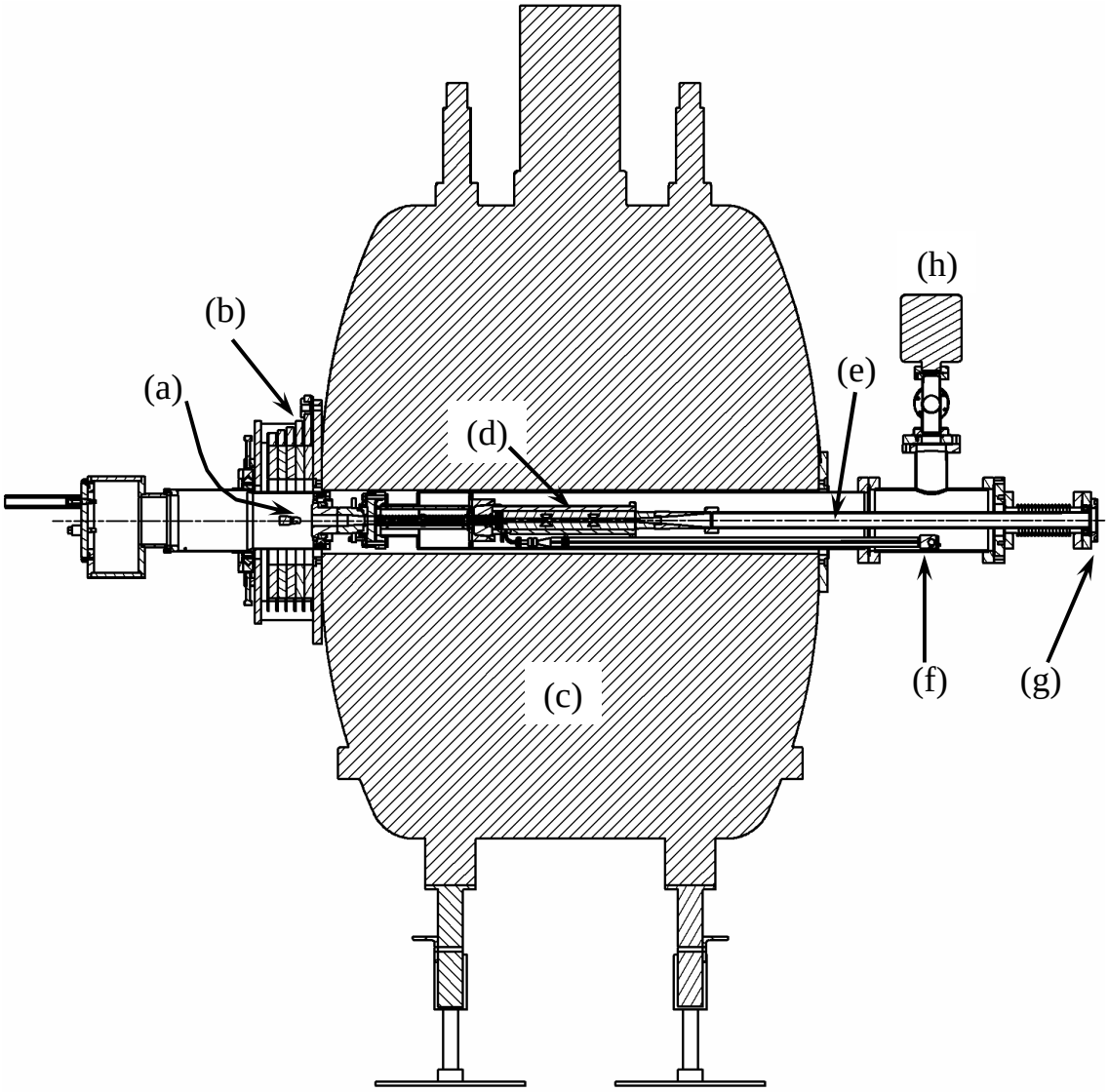

Figure 1-4: A sketch of the gyro-amplifier showing the locations of (a) the cathode of the MIG-type electron gun, (b) external copper gun coil, (c) superconducting magnets, (d) cavity circuit, (e) collector and output waveguide, (f) input waveguide, (g) output window, and (h) vacuum ion pump.

through the glass output window. Ultimately, an internal mode converter allows the operating mode to be converted into a Gaussian beam suitable for transmission through an oversized, low-loss corrugated waveguide to the EPR spectrometer system.

1.5 Thesis Outline

In the following chapters, I present the theoretical basis for this work, the results of the experiment and the conclusions. The focus is primarily on the cavity circuit and the mode converter, since these are the main components that require careful consideration in this project. In chapter 2, I introduce the theory of gyro-devices with emphasis on thorough electromagnetic mode theory as it applies to the confocal gyro-TWA. In chapter 3, the interaction of the electron beam is described in terms of linear and nonlinear theories. Instabilities are addressed and calculated. The experimental results are presented and analyzed in chapter 4, including in-depth descriptions of every major piece of the system. In chapter 5, the mode converter theory and design techniques are presented. The thesis concludes in chapter 6.

Chapter 2

Confocal Waveguide

In a gyro-device, an electron beam gyrating with relativistic cyclotron frequency $\Omega_{cyc} = eB_0/m_0\gamma$ is guided through an interaction circuit that supports a certain electromagnetic mode structure. The electron beam is guided by a strong axial magnetic flux density $\mathbf{B_0} = B_0\hat{z}$ that also causes the electrons to gyrate at cyclotron frequency Ω_{cyc}. Though $\mathbf{B_0}$ is in fact the magnetic flux density, it is commonly referred to as simply "the magnetic field" in literature. The millimeter-wave electromagnetic field components, $\tilde{\mathbf{E}}$ and $\tilde{\mathbf{H}}$, have a frequency ω such that $\omega \approx s\Omega_{cyc}$ and alter the momentum of the electron for cyclotron harmonic s according to the Lorentz force equation:

$$\frac{d\mathbf{p}}{dt} = q\tilde{\mathbf{E}} + q\mathbf{v} \times (\mathbf{B_0} + \tilde{\mathbf{B}}) \tag{2.1}$$

with $q = -e$, $\mathbf{p} = \gamma m_0 \mathbf{v}$, where γ is the relativistic constant,

$$\gamma = \frac{1}{(1 - \beta_\perp^2 - \beta_z^2)^{1/2}} \tag{2.2}$$

where $\beta_\perp = v_\perp/c$ and $\beta_z = v_z/c$.

The weakly relativistic electrons ($\gamma < 1.1$ in this experiment) can transfer their energy to the millimeter-wave (MMW) fields depending on whether they lead or lag the phase of the fields. Therefore, for efficient coupling, the frequency of the supported MMW mode structure is important, as well as the position of the field maxima in

relation to the thin, annular electron beam position.

2.1 Electromagnetic Methods

For gyro-amplifier devices, by far the most common circuit shape is a cylindrical waveguide supporting a low order transverse electric (TE) mode, such as the TE_{01} mode. Increasingly, these cylindrical waveguides are being loaded with either by a continuous application of absorber [65], or by ceramic loads applied periodically to induce a smooth resistive loss [78], or aperiodically to act as severs. Figure 2-1 shows the cylindrical and curved mirror traveling wave geometries that have been explored in literature. The cylindrical waveguide supports TE-modes according to the following dispersion relation,

$$\begin{aligned} k^2 &= k_r^2 + k_z^2 \\ k &= \frac{\omega}{c} \\ k_r &= \frac{\nu_{mp}}{R_w} \end{aligned}$$

where ν_{mp} is the p^{th} solution to the Bessel function of the first kind $J'_m(\nu_{mp}) = 0$ and R_w is the radius of the waveguide. This dispersion relation is plotted in Fig 2-2(a) along with the electron beam resonance line, which contains the Doppler-shifted cyclotron frequency $\omega = k_z v_z + s\Omega_{cyc}$, where v_z is the axial electron velocity, and s is the harmonic number. In this figure, the TE_{03} operating mode was chosen in analogy to the confocal HE_{06} mode, with $R_w = 3.62\ mm$, $\gamma = 1.059$ and $B_0/B_g = 0.997$, where the magnetic field that just grazes the operating mode line is

$$B_g = \frac{m_0}{e}\frac{\gamma}{\gamma_z}\omega_{cut} \tag{2.3}$$

where $\gamma_z = (1-\beta_z^2)^{-1/2}$, and $\omega_{cut} = k_r c$ is the cutoff frequency of the waveguide. In the regions where these lines intersect, there is the possibility of an efficient interaction.

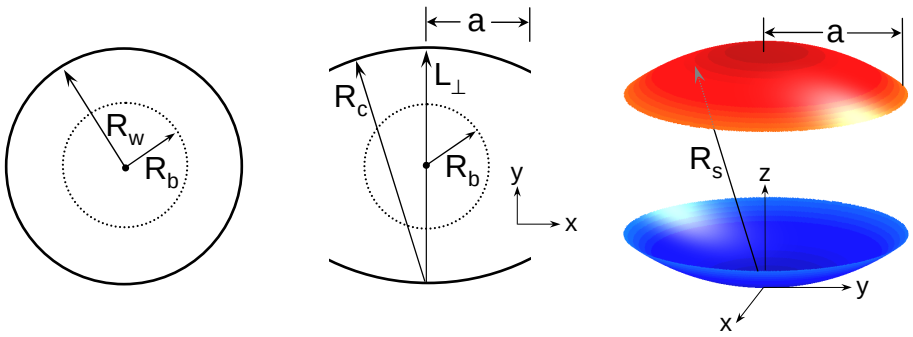

Figure 2-1: (a) Cylindrical geometry, (b) curved cylindrical mirror geometry, where two mirrors with radius of curvature R_c and aperture size a are separated by $L_\perp$. (c) Spherical mirror geometry. R_b is the radius of the electron beam. Note the coordinate systems.

2.2 Theory of Confocal Waveguide

In most amplifier circuits, it is desirable to limit the gain such that self-oscillations are avoided. In a gyro-amplifier, this is certainly no exception. The method of adding distributed loss to the circuit may be employed to stabilize the circuit against oscillations. Confocal waveguide can be constructed to have distributed loss by means of diffraction without the use of absorbers. The same mechanism can be used to filter out unwanted interaction modes, thus reducing the problems of the gyro-BWO oscillations. In applications where a pure Gaussian beam output is required, the mode converter design is simplified since the fields in the confocal waveguide are already Gaussian in one plane.

The geometries of three curved mirror systems are shown in Fig 2-1, namely, (a) cylindrical waveguide, (b) cylindrical confocal mirrors producing a 1-D Gaussian beam, and (c) a spherical confocal resonator supporting a 2-D Gaussian beam. The system of interest here is (b), the cylindrical confocal one where two mirrors of equal radii of curvature R_c are separated by the distance $L_\perp$. The half-width of the mirror, a, is called the aperture of the mirror and is related to the Fresnel diffraction parameter as $C_F = k_\perp a^2/L_\perp$, where $k_\perp$ is the transverse wavenumber. The Gaussian beam in a spherical resonator system has been well studied [79, 80].

The fields in this quasi-optical structure can be approximated as follows. Starting

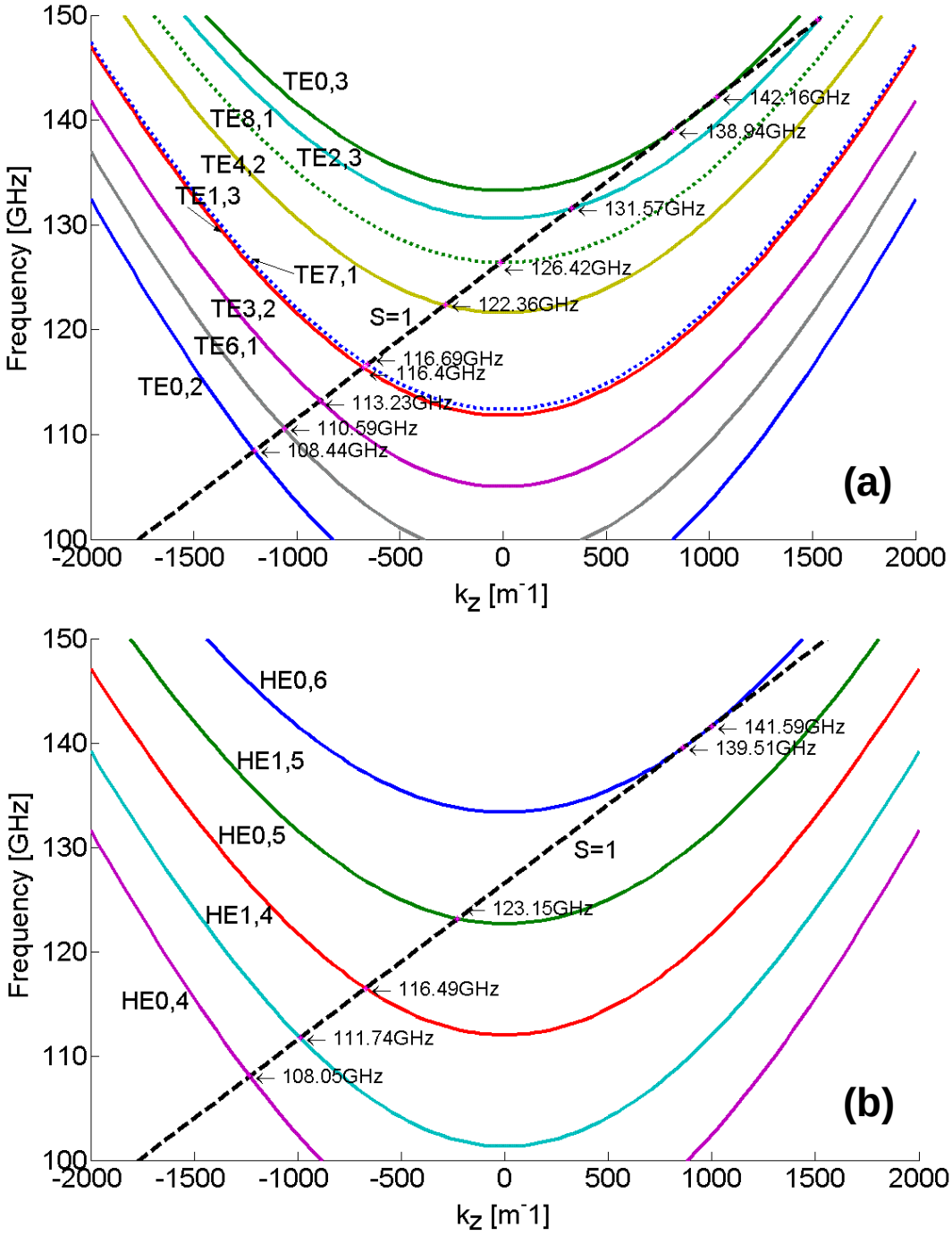

Figure 2-2: The dispersion relation for (a) cylindrical geometry showing many of the lowest order modes, with the TE_{03} mode operating around 140 GHz, and (b) the corresponding confocal modes with HE_{06} around 140 GHz (degenerate modes not shown). The doppler-shifted beam resonance lines are shown for the fundamental harmonic s=1.

from Maxwell's Equations in Cartesian coordinates and assuming only TE modes propagating in the z-direction (thus $E_z \approx 0$), the membrane equations for $\mathbf{E}$ and $\mathbf{H}$ become, at fixed z [81]:

$$
\begin{aligned}
H_z &= \Psi(x,y) && (2.4)\\
H_x &= \frac{jk_z}{k_\perp^2}\frac{\partial}{\partial x}\Psi(x,y) && (2.5)\\
H_y &= \frac{jk_z}{k_\perp^2}\frac{\partial}{\partial y}\Psi(x,y) && (2.6)\\
E_z &= 0 && (2.7)\\
E_x &= \frac{j\omega\mu_0}{k_\perp^2}\frac{\partial}{\partial y}\Psi(x,y) && (2.8)\\
E_y &= \frac{-j\omega\mu_0}{k_\perp^2}\frac{\partial}{\partial x}\Psi(x,y). && (2.9)
\end{aligned}
$$

For a rectangular waveguide, the membrane function is $\Psi(x,y) = \cos k_x x \cos k_y y$, with $k_\perp^2 = k_x^2 + k_y^2$. For cylindrical waveguide with $R = \sqrt{x^2+y^2}$ and $\phi = \arctan(y/x)$, the membrane function is $\Psi(R,\phi) = J_m(k_\perp R)e^{jm\phi}$. Now we will derive the membrane function $\Psi(x,y)$ for the cylindrical confocal waveguide ($L_\perp = R_c$).

We can write the complex $\mathbf{E}$ and $\mathbf{H}$ fields in terms of the vector potential $\mathbf{A}$ and scalar potential Φ, assuming free space permeability $\mu = \mu_0$ [82],

$$
\begin{aligned}
\mu_0\mathbf{H} &= \nabla \times \mathbf{A} && (2.10)\\
\mathbf{E} &= -j\omega\mathbf{A} - \nabla\Phi && (2.11)
\end{aligned}
$$

We relate $\mathbf{A}$ and Φ by Gauss's electric law and by choice of the Lorentz gauge,

$$
\Phi = \frac{j}{\omega\mu_0\epsilon_0}\nabla\cdot\mathbf{A}. \qquad (2.12)
$$

Introducing these into Maxwell's equations, we find that $\mathbf{A}$ and Φ are uncoupled and

independently obey the wave equation,

$$\nabla^2 \mathbf{A} + \omega^2 \mu_0 \epsilon \mathbf{A} = 0 \tag{2.13}$$

$$\nabla^2 \Phi + \omega^2 \mu_0 \epsilon \Phi = 0. \tag{2.14}$$

Therefore, we can conveniently suppose that $\mathbf{A}$ is polarized along some direction, for example $\hat{x}$ (we are assuming the direction of Poynting propagation is in the $\hat{z}$-direction),

$$\mathbf{A} = \hat{x} u_{00}(x, y, z) e^{-jkz} \tag{2.15}$$

where u_{00} stands for the fundamental paraxial solution. We find that the $\mathbf{H}$ fields can be written in the following form, using Eqn 2.10,

$$\mu_0 \mathbf{H} = \left\{ \hat{y} \left[-jk u_{00} + \frac{\partial u_{00}}{\partial z} \right] - \hat{z} \frac{\partial u_{00}}{\partial y} \right\} e^{-jkz}. \tag{2.16}$$

We can invoke the paraxial approximation to limit the size of a free space beam by assuming that the beam does not expand too rapidly. This allows us to discard the $\partial u_{00}/\partial z$ terms and therefore the solution does not exactly satisfy Maxwell's equations. A rigorous Gaussian beam-like solution that does satisfy Maxwell's equations for the spherical confocal cavity case has been carried out elsewhere [83].

Under the paraxial approximation, the $\mathbf{E}$ and $\mathbf{H}$ fields then become,

$$\mu_0 \mathbf{H} = \left[-jk\hat{y} u_{00} - \hat{z} \frac{\partial u_{00}}{\partial y} \right] e^{-jkz} \tag{2.17}$$

$$\mathbf{E} = \left[-j\omega \hat{x} u_{00} - \hat{z} \frac{\omega}{k} \frac{\partial u_{00}}{\partial x} \right] e^{-jkz} \tag{2.18}$$

assuming,

$$k_z = \sqrt{k^2 - k_x^2 - k_y^2} \simeq k - \frac{k_x^2 + k_y^2}{2k} = k - \frac{2}{k w_0^2}. \tag{2.19}$$

and the resulting paraxial wave equation (PWE) is,

$$\nabla_\perp^2 u - 2jk \frac{\partial u}{\partial z} = 0 \tag{2.20}$$

where $\nabla_\perp$ denotes gradient in the transverse $\hat{x}$-$\hat{y}$ plane for a Gaussian beam in a spherical resonator. For a 1-D Gaussian beam in a cylindrical confocal resonator, we have a simpler PWE,

$$\frac{\partial^2 u}{\partial x^2} - 2jk\frac{\partial u}{\partial y} = 0 \tag{2.21}$$

where now the gradient term is only in the x-direction, and the propagation is now in the y-direction, assuming $k_z = 0$.

2.2.1 Gaussian Beams in a Spherical Resonator

The derivation of Gaussian beam propagation in a spherical resonator can be found in Appendix A.

2.2.2 Gaussian Beams in a Cylindrical Confocal Resonator

Now we go back to Fig. 2-1(b) and review the coordinate system. Here we will form a 1-D Gaussian beam in the x-direction and develop a standing wave pattern in the y-direction. The wave will be guided in the z-direction according to k_z.

The solution to Eqn 2.21 can be found by the Fresnel Integral by convolution of the source amplitude distribution $u_0(x_0, y_0)$ with the Fresnel Kernel for a 1-D source,

$$h(x, y) = \sqrt{\frac{j}{\lambda y}} \exp\left(-jk\frac{x^2}{2y}\right) \tag{2.22}$$

which is itself a solution to the PWE. Since the PWE is invariant to translation in the y-coordinate, another solution can be written $h(x, y - y_0, z)$. Without loss of generality, we analytically continue y into the complex plane by the substitution $y \to (y + jb)$, multiply those terms through by $(y - jb)/(y - jb)$ and write the solution,

$$u_0(x, y) = \frac{\sqrt{2}}{\sqrt[4]{\pi}} \frac{1}{w(y)} \exp\left[j\frac{1}{2}\phi(y)\right] \exp\left[-\frac{x^2}{w^2(y)}\right] \exp\left[-jk\frac{x^2}{2R(y)}\right]. \tag{2.23}$$

where the term in front is a normalization, such that, for all y,

$$\int_{-\infty}^{\infty} dx|u_0(x,y)|^2 = 1. \tag{2.24}$$

Comparing the Fresnel Kernels for a spherical system (App. A) to that of the cylindrical system in Eqn 2.22, we see that there is a square root on the multiplying constant that effectively contributes a factor of 1/2 to the first phase term in Eqn 2.23. The definitions of w, R and ϕ are the same as for the Gaussian beam in a spherical resonator,

$$w^2(y) = w_0^2\left[1+\left(\frac{2y}{kw_0^2}\right)^2\right] \tag{2.25}$$

$$\frac{1}{R(y)} = \frac{y}{y^2+(kw_0^2/2)^2} \tag{2.26}$$

$$\tan\phi(y) = \frac{2y}{kw_0^2} \tag{2.27}$$

These equations define a Gaussian beam traveling in the $+y$ direction with phase front radius of curvature $R(y)$, phase $\phi(y)$ and beam waist $w(y)$ at the point where the electric field has fallen to $1/e$ of its maximum amplitude. It should be noted that others, particularly in Russia (and previous MIT theses [57, 84]), have defined w_0 to be the point where the *intensity* falls to $1/e$ (and hence the electric field falls to $e^{-1/2}$). The two are related by $w_{0(E)}^2 = 2w_{0(I)}^2$, where the E and I denote the electric field notation and intensity notation, respectively. Here, the more conventional electric field notation used by Boyd [79, 80], Haus [82] and others is used.

The minimum beam waist is given by

$$w_0 = \sqrt{\frac{2b}{k}} \tag{2.28}$$

which can be solved for the confocal parameter, $b = kw_0^2/2 = \pi w_0^2/\lambda$.

For now, we replace k in the equations with $k_\perp$ to define the wavenumber in the x,y-plane leaving the waves to be guided in the z-direction according to $k^2 = k_z^2 + k_\perp^2$. For the derivation of the membrane function, we will essentially set $k_z = 0$ and replace

k with our new $k_\perp$ that we are about to define. Propagation with non-zero k_z is treated in Sec. 5.1 on the mode converter design.

To calculate $k_\perp$, we refer back to Fig. 2-1(b) and can use Eqns 2.25-2.26 to match the radius of curvature of the phase fronts $R(y)$ to the radius of curvature of the top mirror R_c located at $y = L_\perp/2$,

$$R\left(y = \frac{L_\perp}{2}\right) = \frac{L_\perp}{2}\left[1 + \left(\frac{kw_0^2}{L_\perp}\right)^2\right] = R_c$$

Solving for w_0^2,

$$w_0^2 = \frac{L_\perp}{k}\sqrt{\frac{2R_c - L_\perp}{L_\perp}} \tag{2.29}$$

The beam radius at the mirror surface $y = L_\perp/2$ is then,

$$w\left(y = \frac{L_\perp}{2}\right) = w_0\left[1 + \left(\frac{L_\perp}{kw_0^2}\right)^2\right]^{1/2} = \sqrt{\frac{2R_c}{k}}\left(\frac{L_\perp}{2R_c - L_\perp}\right)^{1/4} \tag{2.30}$$

To obtain n standing wave peaks between the curved mirrors, we counter-propagate two Gaussian beams in the $\pm\hat{y}$-direction and superimpose them in or out of phase, noting that $w(-y) = w(y)$, $R(-y) = -R(y)$ and $\phi(-y) = -\phi(y)$,

$$u_0(x,y)e^{-jky} + u_0(x,-y)e^{+jky} = \\ = \frac{2\sqrt{2}}{\sqrt[4]{\pi}}\frac{1}{w(y)}\exp\left[-\frac{x^2}{w^2(y)}\right]\cos\left[\frac{1}{2}\phi(y) - ky - \frac{kx^2}{2R(y)}\right] \tag{2.31}$$

$$u_0(x,y)e^{-jky} - u_0(x,-y)e^{+jky} = \\ = j\frac{2\sqrt{2}}{\sqrt[4]{\pi}}\frac{1}{w(y)}\exp\left[-\frac{x^2}{w^2(y)}\right]\sin\left[\frac{1}{2}\phi(y) - ky - \frac{kx^2}{2R(y)}\right] \tag{2.32}$$

In order to create a resonant structure out of these two beams, we simply place curved mirrors at the nulls defined by,

$$\frac{kx^2}{2R(z)} = const. \tag{2.33}$$

The resonance condition on the *cos* term of Eqn. 2.31 requires an integral number of round trip wavelengths to be satisfied. We evaluate the argument of this *cos* term at $x = 0, y = L_\perp/2$ and plug in for $\phi(y)$ with Eqn. 2.29,

$$k_\perp y - \frac{1}{2}\phi(y) = k_\perp \frac{L_\perp}{2} - \frac{1}{2}\arctan\sqrt{\frac{L_\perp}{2R_c - L_\perp}} = q\pi \tag{2.34}$$

where q is an integer describing the number of maxima in the y-direction from the midplane ($y = 0$) to the mirror. We use $n = 2q$ to denote the total number of variations between a pair of confocal mirrors for the HE_{0n} mode. The resulting general wavenumber is, after simplifying the *arctan* to *arcsin*,

$$k_\perp = \frac{\pi}{L_\perp}\left(n + \frac{1}{\pi}\arcsin\sqrt{\frac{L_\perp}{2R_c}}\right) \tag{2.35}$$

which also agrees with the derivation by Nakahara [85], following Gorbau [86]. This equation also satisfies Eqn. 2.32, valid when n is odd. For the confocal case ($L_\perp = R_c$), this reduces further to simply,

$$k_\perp = \frac{\pi}{L_\perp}\left(n + \frac{1}{4}\right) \tag{2.36}$$

But we can have m variations in the x-direction as well in the more general HE_{mn} mode (the m-dependence is missing in our equation for $k_\perp$ here since we evaluated at $x = 0$). As we will see in Sec 2.2.3, modes with $m > 0$ are not confined well in the waveguide and are thus filtered out, hence this may be all the $k_\perp$ we really need. Modes with $m \geq 1$ are difficult to excite due to the null in the electric field down the center plane of the waveguide. For the sake of completeness, Weinstein [87] describes the more general resonator consisting of two identical cylindrical mirrors with radius of curvature R_c facing each other with maximum separation $L_\perp = 2l$ and n standing wave variations between the mirrors. The complex frequency $\omega = ck$ of the two-dimensional modes is given by,

$$2kl = \pi n + \chi \tag{2.37}$$

where, for large integer n,

$$\begin{aligned}\chi &= (2m+1)\alpha + 2\pi p, \quad m = 0, 1, 2, \ldots \\ \alpha &= \arcsin\sqrt{\frac{l}{R_c}} \\ p &= p' - jp''\end{aligned}$$

where $\Delta = 2\pi p'$ is a small additional phase shift, and $\Lambda = 4\pi p''$ is a measure of the diffraction losses. The full general equation for $k_\perp$ for the HE_{mn} mode becomes,

$$k_\perp = \frac{\pi}{L_\perp}\left(n + \frac{2m+1}{\pi}\arcsin\sqrt{\frac{L_\perp}{2R_c}} + \frac{\Delta}{\pi}\right) - j\frac{\Lambda}{2L_\perp} \tag{2.38}$$

For the special confocal case with $R_c = L_\perp = 2l$, this equation reduces to simply,

$$k_\perp = \frac{\pi}{R_c}\left(n + \frac{m}{2} + \frac{1}{4}\right) - j\frac{\Lambda}{2R_c} = k_{\perp r} + jk_{\perp i} \tag{2.39}$$

where the complex component Λ describing the loss is related to the radial wavefunction in prolate spherical coordinates, $R^{(1)}_{0,m}(\xi_1, \xi_2)$ as,

$$\Lambda = 2\ln\left[\sqrt{\frac{\pi}{2C_F}}\frac{1}{R^{(1)}_{0,m}(C_F, 1)}\right] \tag{2.40}$$

where $C_F = ka^2/L_\perp$ is the Fresnel diffraction parameter. The radial wavefunction in prolate spherical coordinates comes from a solution of the integral equation resulting from the application of Huygens' Principle to the recurrence of the electric field patterns on the mirrors. This homogenous Fredholm integral equation of the second kind is written for the confocal case as,

$$\begin{aligned}f(x) &= \sqrt{\frac{C_F}{2\pi}}e^{j(\chi-\pi/4)}\int_{-1}^{1} e^{-jC_F x x'} f(x')dx' \\ R^{(1)}_{0,m}(C_F, x) &= \frac{f(x)}{A}\end{aligned}$$

where A is a constant evaluated as $x \to \infty$. Loss can be understood in terms of an

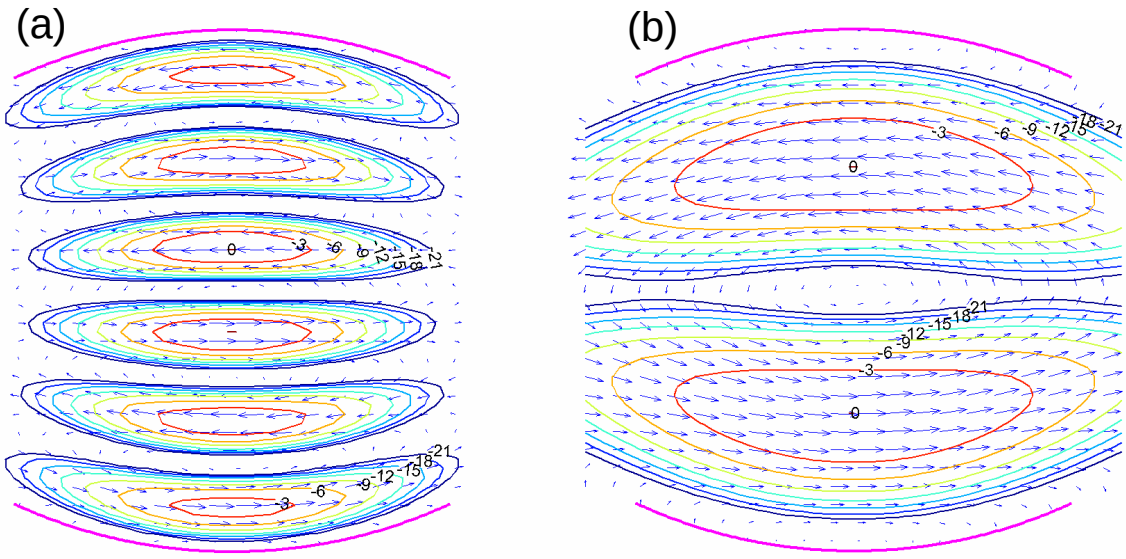

Figure 2-3: Theoretical power contours in dB of the membrane function for (a) the HE_{06} mode and (b) the HE_{02} mode in the same waveguide overlaid with electric field vectors. The HE_{02} mode leaks out much more due to its much larger footprint on the mirrors.

equivalent infinite series of identical focusing lenses, where the transverse dimension of each lens is too small to capture all of the incident power, so power is lost on each successive step. For modes with $m = 0$, the power is concentrated at the center of the lens, so only the weak edges are attenuated. For modes with $m > 0$, the bulk of the power is near the edge of the mirror and thus easily lost. For modes of low order n, the effective "footprint" of the mode on the mirror is relatively large, so more power is lost at the edges when compared to modes with large n, which have a smaller footprint. Figure 2-3 shows a plot of the theoretical membrane functions of Eqn. 2.41 for the HE_{06} and HE_{02} modes for the same waveguide to illustrate this footprint concept. Thus the confocal system effectively filters out modes with $m > 0$ as well as modes with lower n values.

As a consequence of Eqn 2.39, The HE_{mn} modes are degenerate according to $m/2 + n = const$, hence the HE_{06} mode is degenerate with five others, namely, the HE_{25}, HE_{44}, HE_{63}, HE_{82}, and $HE_{10,1}$ modes. As we will see in Sec. 2.2.3, the $m > 0$ modes are essentially filtered out of an open structure with small aperture a, leaving only the lowest order HE_{06} mode.

For the membrane function $\Psi(x,y)$, we now have the standing wave Eqns 2.31 and 2.32. If we place the mirrors confocally at $L_\perp = R_c$, and set $z = 0$, we can write the membrane function for confocal waveguide as,

$$\Psi(x,y) = \sqrt{\frac{w_0}{w(y)}} \exp\left[-\frac{x^2}{w^2(y)}\right] \cdot \begin{cases} Re\left\{\exp\left[-j\frac{k_\perp x^2}{2R(y)}\right] f(y)\right\}, & n = 2,4,6,\ldots \\ Im\left\{\exp\left[-j\frac{k_\perp x^2}{2R(y)}\right] f(y)\right\}, & n = 3,5,7,\ldots \end{cases} \tag{2.41}$$

where the profile $f(y)$ has n peaks in the standing wave distribution in the y-direction,

$$f(y) = \exp\left[j\left(k_\perp y - \frac{1}{2}\arctan\frac{2y}{R_c}\right)\right] \tag{2.42}$$

where $k_\perp(n)$ is defined in Eqn 2.39. Figure 2-3(a) shows the resulting electric fields for the HE_{06} using Eqns 2.4 through 2.9 and 2.41. Higher order modes with $m \neq 0$ can be obtained by counter-propagating two Hermite-Gaussian beams in an analogous way to the spherical solutions in Appendix A.

2.2.3 Loss Rate Estimation in Confocal Waveguides

Since the transverse wavenumber $k_\perp$ is complex according to Eqn 2.39, there is the possibility of intentionally diffracting some portion of the power out of the waveguide in order to stabilize against oscillations. Assuming the fields are guided in the z-direction according to $\exp(-jk_z z)$, we can write the loss rate in dB/cm for the confocal waveguide of aperture a and $R_c = L_\perp$ as,

$$LossRate = -0.0869 k_{zi} \tag{2.43}$$

$$k_{zi} = Im\left\{\sqrt{\left(\frac{w}{c}\right)^2 - k_\perp^2}\right\} \tag{2.44}$$

where $k_\perp = k_{\perp r} + jk_{\perp i}$ as before. To reduce the computational complexity of evaluating the radial wavefunction in prolate spherical coordinates, a series of fits were

Table 2.1: Loss rate example, $R_c = 6.9\ mm$, $a = 2.5\ mm$

Mode	Frequency	Loss Rate	Interaction
HE_{06}	140 GHz	-1 dB/cm	Forward
HE_{15}	128.8	-20	BWO
HE_{24}	117.6	-54	BWO
HE_{05}	117.6	-2	BWO

performed for the lowest order m-modes (see [88], Chap. 11),

$$\log_{10}(\Lambda) = -0.0069C_F^2 - 0.7088C_F + 0.5443, \quad m = 0 \tag{2.45}$$

$$\log_{10}(\Lambda) = -0.0226C_F^2 - 0.4439C_F + 1.0820, \quad m = 1 \tag{2.46}$$

$$\log_{10}(\Lambda) = -0.0363C_F^2 - 0.1517C_F + 1.0075, \quad m = 2 \tag{2.47}$$

where $k_{\perp i} = \Lambda/2R_c$. As an example of the loss rates encountered by various modes, Table 2.1 gives a comparison of several modes for $R_c = 6.9\ mm$ and $a = 2.35\ mm$ in a confocal waveguide at 140 GHz. Clearly, the HE_{mn} modes with index $m > 0$ are not supported in this structure, effectively eliminating them as possible interaction modes. The HE_{05} mode with a low loss rate, on the other hand, is far from its calculated cutoff frequency of 114 GHz and therefore is not easily susceptible to backward wave oscillations, but must be considered anyway. Figure 2-4 shows the calculated loss rate versus frequency for the HE_{06} mode compared to a simulation in the electromagnetic simulation code HFSS by Ansoft, Inc. [89]. The agreement is very good and tends to diverge more only at very small apertures where edge diffraction dominates and the fields are no longer approximately Gaussian.

2.2.4 General Curved Mirror Resonator Stability

In this subsection, we will show the regions of stability for a general curved mirror system assuming first an optical regime. In general, we can have two mirrors with radius of curvature R_1 and R_2 (using the definition of $R(y)$ in Eqn. 2.26), and position

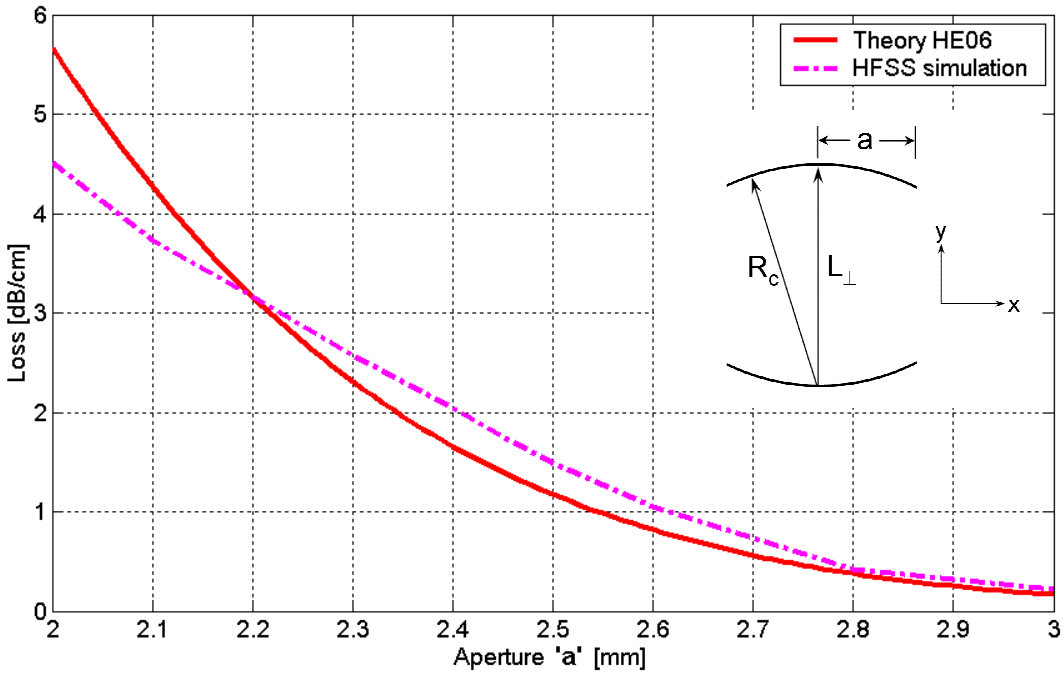

Figure 2-4: Comparison of loss rate at 140 GHz for $R_c = L_\perp = 6.9\ mm$ between theory (solid) and HFSS simulation (dash).

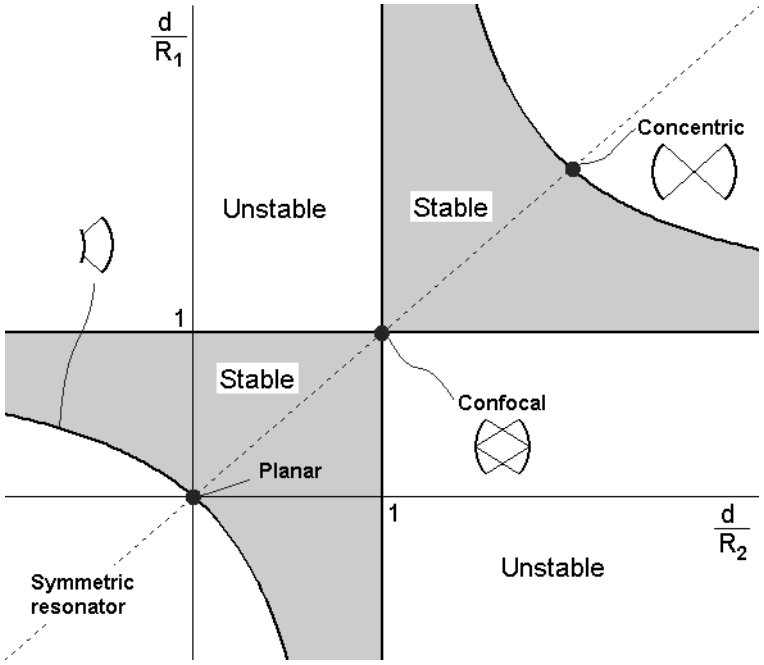

Figure 2-5: Stable and unstable regions of a resonator of curved mirrors in the optical regime.

z_1 and z_2 separated by distance d such that,

$$\begin{aligned} R_1 &= \frac{z_1}{z_1^2 + b^2} \\ R_2 &= \frac{z_2}{z_2^2 + b^2} \\ d &= z_2 - z_1 \end{aligned}$$

If we solve R_1 and R_2 for z_1 and z_2 (quadratic equations) and substitute into d, we can square the resulting equations and solve for the confocal parameter, b that defines the Gaussian beam,

$$b^2 = \frac{1}{16} \frac{R_1^2 R_2^2 - 4[d - (R_1 + R_2)/2]^2 - (R_1^2 + R_2^2)}{[d - (R_1 + R_2)/2]^2} \tag{2.48}$$

For a Gaussian beam, b must be real, so the numerator must be greater than 0. This condition implies stability boundaries parameterized by the equation,

$$0 \leq \left(1 - \frac{d}{R_1}\right)\left(1 - \frac{d}{R_2}\right) \leq 1 \tag{2.49}$$

which leads to the plot in Fig 2-5, ignoring diffraction and loss. The regions of stability and instability are blurred when diffraction and loss are included. It has been shown in the literature that the confocal case ($R_1 = R_2 = d$) is the minimal loss configuration even though it is on the boundary between stability and instability [87].

2.3 Discussion

I have derived the equations for the electromagnetic fields in the confocal waveguide system and for the wavenumber in a general curved cylindrical resonator system. The confocal interaction circuit proves to be mode selective and can stabilize the amplifier by allowing a controllable amount of diffractive loss. The loss rate theory is consistent with simulations and is used to show that potential backward HE_{mn} wave oscillations with $m > 0$ are very heavily attenuated. In the next chapter, the interaction of the electron beam with these electromagnetic fields is described in detail.

Chapter 3

Theory of Gyro-devices

We now have a complete description of the fields in the confocal structure given by Eqns 2.4 through 2.9, 2.39 and 2.41. As for the electron beam, Fig 3-1 shows the geometry of the electron orbit in the transverse plane. The electrons gyrate around the guiding center position r_g, which is equal to the average beam radius r_b, and have a Larmor radius of r_L and cyclotron frequency Ω_{cyc} given by

$$\Omega_{cyc} = \frac{eB_0}{m_0\gamma} = \frac{v_\perp}{r_L} \tag{3.1}$$

Here, it is helpful to note that the cyclotron frequency can be held constant for changes in magnetic field by compensating γ, which is a function of beam voltage (Eqn. 2.2). Another interpretation is that as the relativistic electron energy (in the form of γ) increases at constant magnetic field due to the presence of synchronized millimeter-wave (MMW) fields, the electron's cyclotron frequency decreases slightly, causing a slip in phase that enables the electron to gain energy from the wave. This view is important because the electrons must take energy from the MMW as a precondition to *bunching*, the process whereby electrons evenly distributed azimuthally are forced to form a single group or "bunch" of charge; and bunching must form before energy extraction can occur. Appendix B contains a derivation of the bunching mechanisms along with a discussion of the kinematics involved in the process. A brief summary is presented here.

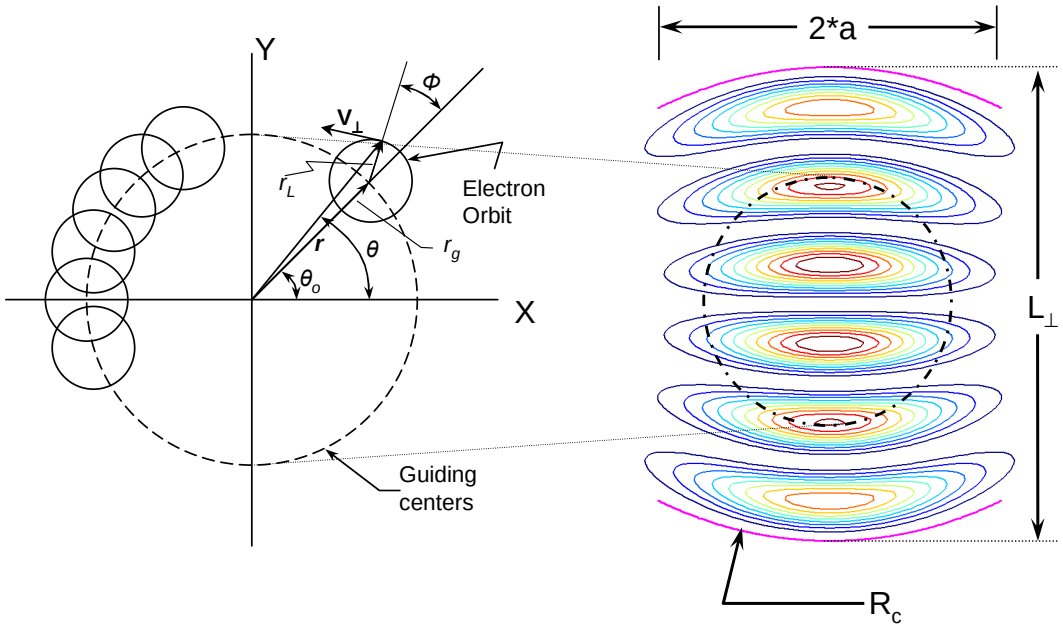

Figure 3-1: (left) Geometry of the electron beam showing guiding center beam radius r_g and Larmor radii r_L. (right) Confocal interaction geometry showing mirror aperture half-width a, radii of curvature R_c and mirror separation $L_\perp$ with power contours for the HE_{06} mode superimposed. Transverse electric field vectors are also shown. The electron beam interacts primarily with the second and fourth maxima.

The electron motion is governed by the Lorentz force Eqn 2.1, repeated here for clarity,

$$\frac{d\mathbf{p}}{dt} = -e\left[\tilde{\mathbf{E}} + \mathbf{v} \times (\mathbf{B_0} + \tilde{\mathbf{B}})\right]$$

where $\mathbf{p} = \gamma m_0 \mathbf{v}$ is the relativistic momentum. The change of electron energy can be written,

$$\frac{d\varepsilon}{dt} = q(\mathbf{E} \cdot \mathbf{v}) \tag{3.2}$$

where $\varepsilon = \gamma m_0 c^2$. Because we are dealing with modes that are predominantly transverse **E**-fields ($E_z \approx 0$ and $H_\perp$ is small), there is essentially no change in the axial velocity of the electrons due to the interaction. A proof of this situation is given in Appendix B. The amplification is due to extraction and interaction of only the perpendicular energy of the electrons.

Due to the small size of the Larmor radius with respect to the field patterns in the waveguide, the electric field over a Larmor radius is approximately constant in space and, without loss of generality, can be assumed a convenient form, for example, $\mathbf{E} = \hat{x} E_0 \exp(j\omega t)$. Then two gyrating electrons opposite a guiding center from each other ($\Delta\phi = 180°$, where ϕ is defined in Fig. 3-1) experience the same force $\mathbf{F} = q\mathbf{E}$, slowing one electron while accelerating the other. This tends to bunch the electrons together resulting in an oscillating current J that drives the $\nabla \times \mathbf{H}$ term in Ampere's law of Maxwell's equations.

3.1 Linear Dispersion Relation

Detailed derivations of the Doppler-shifted dispersion relation for a cylindrical waveguide are presented for both $TE-$ and $TM-$modes in [90] (MKS units), and for the gyro-TWT and gyro-CARM amplifiers in [91] (CGS units). Taking a form that

includes wall losses by skin depth δ,

$$D(\omega,k_z)=\frac{\omega^2}{c^2}-k_z^2-k_{mn}^2\left[1-(1+j)\left(1+\frac{m^2}{\nu_{mn}^2-m^2}\frac{\omega^2}{\omega_{cut}^2}\right)\frac{\delta}{r_w}\right]$$
$$-\frac{16\pi^2e^2}{m_ec^2r_w^2K_{mn}}\int_0^{r_w^{max}}r_g\;dr_g\int_0^{\infty}p_\perp\;dp_\perp\int_{-\infty}^{\infty}dp_z\;\frac{f_0}{\gamma}$$
$$\cdot\sum_{s=-\infty}^{\infty}\left[\frac{-\beta_{\perp0}^2(\omega^2-k_z^2c^2)H_{sm}(k_{mn}r_{g0},k_{mn}r_{L0})}{(\omega-k_zv_{z0}-s\Omega_{cyc})^2}\right.$$
$$\left.+\frac{(\omega-k_zv_{z0})T_{sm}(k_{mn}r_{g0},k_{mn}r_{L0})-k_{mn}v_{\perp0}U_{sm}(k_{mn}r_{g0},k_{mn}r_{L0})}{\omega-k_zv_{z0}-s\Omega_{cyc}}\right]=0, \quad (3.3)$$

where ω is the operating frequency, $\omega_{cut}=k_{mn}c$ is the cutoff frequency for the TE_{mn} mode ($k_{mn}=k_\perp$ used earlier), and $r_w^{max}\approx r_g+r_L$ is the outer edge of the electron locations. For the cylindrical TE_{mn} mode,

$$K_{mn}=J_m^2(\nu_{mn})\left(1-\frac{m^2}{\nu_{mn}^2}\right), \quad (3.4)$$

where J_m is the m-th order Bessel function of the First Kind of order m, $J_m'(\nu_{mn})=0$, and

$$\begin{aligned}
H_{sm}(x,y) &= J_{s-m}^2(x)J_s'^{\,2}(y)\\
T_{sm}(x,y) &= 2H_{sm}(x,y)+yJ_s'(y)\left\{2J_{s-m}^2(x)J_s''(y)-J_s(y)\right.\\
&\cdot\quad \left.\left[\frac{1}{x}J_{s-m}(x)J_{s-m}'(x)+J_{s-m}'^{\,2}(x)+J_{s-m}(x)J_{s-m}''(x)\right]\right\}\\
U_{sm}(x,y) &= -\frac{1}{2}yJ_s'(y)\left\{J_{s-1}(y)[J_{s-m-1}^2(x)-J_{s-m}^2(x)]\right.\\
&+\quad \left.J_{s+1}(y)[J_{s-m+1}^2(x)-J_{s-m}^2(x)]\right\},
\end{aligned}$$

where x and y are the arbitrary arguments of the functions and s is the cyclotron harmonic number. Finally, f_0 is the zeroth-order perturbation term in the relativistic 7-dimensional Vlasov equation,

$$\frac{\partial}{\partial t}f+\mathbf{v}\cdot\frac{\partial}{\partial\mathbf{x}}f-e\left[\mathbf{E}+\mathbf{v}\times(B_0\hat{z}+\mathbf{B})\right]\cdot\frac{\partial}{\partial\mathbf{p}}f=0 \quad (3.5)$$

where $\mathbf{x}$ is the spatial vector, $\mathbf{p}$ is the momentum vector, and t is time. The Vlasov equation is linearized according to small signal assumptions, such that $f(\mathbf{x},\mathbf{p},t) = f_0(\mathbf{x},\mathbf{p}) + f_1(\mathbf{x},\mathbf{p},t)$. Considering the electron orbit in Fig. 3-1, f_0 can be further reduced to,

$$f_0 = f_0(r_g, p_\perp, p_z). \tag{3.6}$$

For a thin, hollow electron beam with zero guiding center spread, we have a fairly simple zeroth order term,

$$f_0 = \frac{N_b}{2\pi r_{g0}}\delta(r_g - r_{g0})\frac{1}{2\pi p_{\perp 0}}\delta(p_\perp - p_{\perp 0})\delta(p_z - p_{z0}). \tag{3.7}$$

For zero velocity spread, the dispersion relation in Eqn. 3.3 is reduced to,

$$\begin{aligned} D(\omega,k_z) = \frac{\omega^2}{c^2} - k_z^2 - k_{mn}^2 \left[1 - (1+j)\left(1 + \frac{m^2}{\nu_{mn}^2 + m^2}\frac{\omega^2}{\omega_{cut}^2}\right)\frac{\delta}{r_w}\right] \\ - \frac{4}{r_w^2 K_{mn}}\frac{I_b}{I_A}\left[\frac{-\beta_{\perp 0}^2(\omega^2 - k_z^2c^2)H_{sm}(k_{mn}r_{g0}, k_{mn}r_{L0})}{(\omega - k_z v_{z0} - s\Omega_{cyc})^2}\right. \\ \left. + \frac{(\omega - k_z v_{z0})T_{sm}(k_{mn}r_{g0}, k_{mn}r_{L0}) - k_{mn}v_{\perp 0}U_{sm}(k_{mn}r_{g0}, k_{mn}r_{L0})}{\omega - k_z v_{z0} - s\Omega_{cyc}}\right] = 0, \end{aligned} \tag{3.8}$$

where I_b is the DC beam current in Amperes, and $I_A = 17.05\beta_{z0}\gamma_0$ kA is the Alfvén current.

Methods for including a Gaussian velocity spread to the dispersion relation have also been published [91]. To include velocity spread in the linear dispersion relation (Eqn. 3.3), a Gaussian momentum spread is introduced,

$$f_0 = \frac{N_b}{2\pi r_{g0}}\delta(r_g - r_{g0})g(p_\perp, p_z) \tag{3.9}$$

$$g(p_\perp, p_z) = A\delta(\gamma - \gamma_0)exp\left[\frac{-(p_z - p_{z0})}{2(\Delta p_z)^2}\right]. \tag{3.10}$$

3.2 Linear Theory

The linear growth rate for a gyro-TWT can be estimated from the dispersion relation by assuming that the fields grow axially as $\exp(2|k_{zi}|z)$, where k_{zi} is the dominant

i-th complex root of the dispersion relation equation $D(\omega, k_{zi}) = 0$, subject to the condition that the beam current is below the oscillation start current threshold, that is, $I_b < I_c$.

Using the generalized formalism of Nusinovich [92], we can develop a linear theory without deriving the full dispersion relation for a confocal structure. First we define a few normalized parameters,

$$\bar{\Delta} = \frac{1}{\beta_z}\left(1 - \frac{h}{k}\beta_z - \frac{s\Omega_{cyc}}{\omega}\right) \tag{3.11}$$

$$b = \frac{h}{k}\frac{\beta_\perp^2}{2\beta_z}\left(1 - \frac{h}{k}\beta_z\right)^{-1} \tag{3.12}$$

$$\bar{\mu} = \frac{\beta_\perp^2}{2\beta_z}\frac{1-(h/k)^2}{1-(h/k)\beta_z} \tag{3.13}$$

where $h = \sqrt{k^2 - k_\perp^2}$ is the axial wavenumber and s is the cyclotron harmonic.

Assuming the fields grow as $\exp(-i\Gamma\zeta)$, where $\zeta = kz$ is the normalized length, the TWT equation can be written,

$$\Gamma^3 - \bar{\Delta}\Gamma^2 - I_0'(s-b)\Gamma + (\bar{\mu} - \bar{\Delta}b)I_0' = 0, \tag{3.14}$$

where the normalized current $I_0' = [\xi^{s-1}/(s-1)!2^s]^2 I_0$ with $\xi = \kappa(p_{\perp 0}/\mu)$ and $\mu = eH_0/m_0c\omega$. The variable I_0 is then written in terms of the actual DC electron beam current I,

$$I_0 = \frac{e|I|}{m_0c^3}\frac{c^2}{\omega k N_s}\frac{1-(h/k)\beta_z}{\kappa\gamma_0\beta_{z0}^2}|L_s|^2, \tag{3.15}$$

where $\kappa = k_\perp/k$, and the coupling coefficient is,

$$L_s = \left[\frac{1}{\kappa}\left(\frac{\partial}{\partial X} + j\frac{s}{|s|}\frac{\partial}{\partial Y}\right)\right]^{|s|}\Psi(X,Y) = e^{js\phi}\left[\frac{1}{\kappa}\left(\frac{\partial}{\partial R} + \frac{j}{R}\frac{\partial}{\partial\phi}\right)\right]^{|s|}\Psi(R,\phi) \tag{3.16}$$

with the transformations $X = R\cos(\phi)$ and $Y = R\sin(\phi)$ for cylindrical coordinates. Here $\Psi(X,Y)$ is the membrane function that was defined at the end of Section 2.2.2.

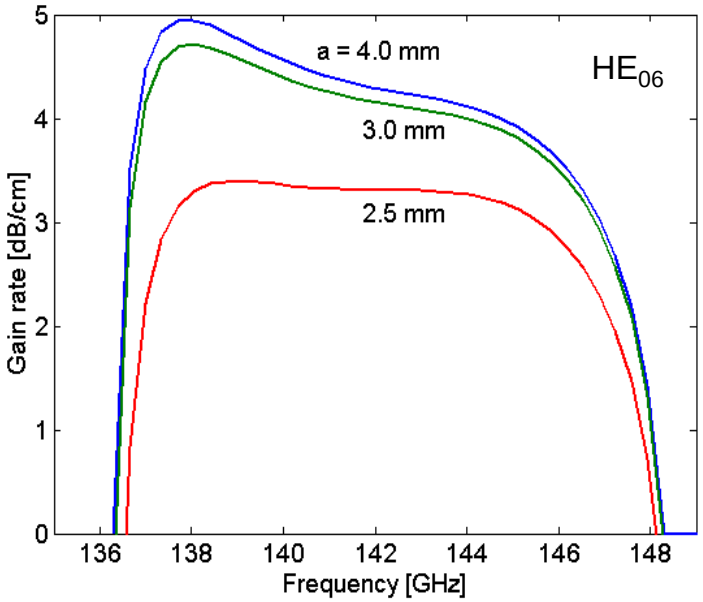

Mode	HE_{06}
V_0	30 kV
I_0	2A
α	0.75
B_0	4.94T
$L_\perp$	6.9mm
R_c	6.9mm
$k_\perp$	2.846 mm^{-1}

Figure 3-2: Linear growth rate calculation based on the linear dispersion relation for the parameters shown. Velocity spreads were not included. A growth rate of at least 2.5 dB/cm is needed for the amplifier.

The norm N_s can be written,

$$N_s = \int_{S_\perp} \{\mathbf{E_s} \times \mathbf{H_s^*} - \mathbf{H_s} \times \mathbf{E_s^*}\} \cdot \mathbf{z_0} dS_\perp = \frac{kh}{k_\perp^2} \sqrt{\frac{\pi L_\perp^3}{2k_\perp}}, \tag{3.17}$$

for confocal waveguide.

Using this series of relations, Eqn 3.14 can be solved to give an estimate of the linear growth rate for a given set of operating parameters. Figure 3-2 shows a simulation result of the linear growth rate of a confocal amplifier for a given set of operating parameters, excluding velocity spreads. The linear theory predicts growth rates of over 3 dB/cm for an aperture size of $a = 2.5$ mm and $L_\perp = R_c = 6.9$ mm, at 30 kV, 2 A, $\alpha = 0.75$ and $B_0 = 4.94$ T. To reach 50 dB gain with a 25 cm structure, the gain rate must be around 2.5 dB/cm (including severs), so this result looks promising.

3.3 Kinetic Theory

The details of the single particle theory were worked out by Yulpatov [93] and later generalized by Nusinovich [92, 94]. Methods for introducing Gaussian velocity spread to the kinetic equations have been published [95]. The following is a set of self-consistent equations for a gyro-TWT for a single-mode interaction by a thin beam in an arbitrary waveguide with an azimuthally symmetric hollow beam beam,

$$\frac{dw}{d\zeta} = -2\frac{(1-w)^{s/2}}{1-bw} Re\left\{F' \exp(-j\bar{\theta}_s)\right\} \tag{3.18}$$

$$\frac{d\bar{\theta}_s}{d\zeta} = \frac{1}{1-bw}\left[\bar{\mu}w - \bar{\Delta} - s(1-w)^{\frac{s}{2}-1} Im\left\{F' \exp(-j\bar{\theta}_s)\right\}\right] \tag{3.19}$$

$$\frac{dF'}{d\zeta} = -I_0' \frac{1}{\pi}\int_0^{2\pi} \frac{(1-w)^{s/2}}{1-bw} \exp(j\bar{\theta}_s) d\bar{\theta}_0. \tag{3.20}$$

The slowly-varying electron phase is $\theta = s\phi - \omega t + hz$, where ϕ is the electron position defined in Fig. 3-1. A full derivation of the conversion to slow-time scale variables is given as an appendix in [65]. The primed variables are defined,

$$F' = \frac{\xi^{s-1}}{(s-1)!2^s} F$$

$$I_0' = \left(\frac{\xi^{s-1}}{(s-1)!2^s}\right)^2 I_0$$

where I_0 is defined in Eqn 3.15, b was defined in Eqn 3.12, $\xi = \kappa(p_{\perp 0}/\mu)$, and the normalized energy of the electrons is

$$w = 2\frac{1-(h/k)\beta_{z0}}{\beta_{\perp 0}^2}\frac{\gamma_0 - \gamma}{\gamma_0}.$$

The electron phase for harmonic s is given by $\bar{\theta}_s$, and F is the normalized wave amplitude that includes the arbitrary waveguide factor L_n,

$$F = \frac{1-(h/k)\beta_{z0}}{\kappa\gamma_0\beta_{z0}\beta_{\perp 0}}\frac{eA}{m_0 c\omega}|L_n|$$

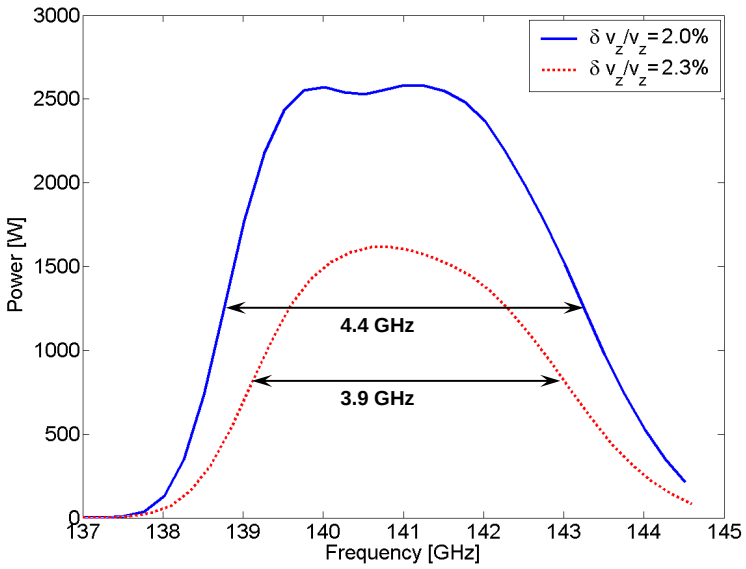

Mode	HE_{06}
V_0	30 kV
I_0	2 A
α	0.75
R_b	1.9 mm
B_0/B_g	0.998
$L_\perp = R_c$	6.9 mm
a	2.4 mm
Loss rate	2 dB/cm
P_{in}	10 mW

Figure 3-3: A nonlinear confocal simulation at 30 kV predicting a gain of over 50 dB and a bandwidth of around 4 GHz for various velocity spread conditions.

where A is the amplitude of the electromagnetic field in

$$\mathbf{E} = Re\left\{A(z)\mathbf{E}(\mathbf{r}_\perp)\exp[i(\omega t - hz)]\right\}.$$

Using the set of equations defined above, a code has been written [57] to evolve the nonlinear differential equations at each location in z including velocity spread effects. A result of the simulation is shown in Fig. 3-3 for a given set of operating parameters. The simulation assumes three 7 cm amplifier sections separated by two severs. The 7 cm amplifier length limit is taken from the BWO calculation (Sec. 3.4.1) for a 2 A beam current. The severs are simply very narrow mirror apertures that are predicted in HFSS to have over 30 dB electromagnetic loss at 140 GHz. The nonlinear simulation in Fig. 3-3 shows that, for the operating parameters given, gains of over 50 dB would be possible with bandwidths near 4 GHz, if the total parallel velocity spread could be maintained below 2.3 % (approx. 5 % perpendicular spread). Clearly, velocity spread is critical to the performance of the amplifier. Variations in mirror alignment and spacing $L_\perp$ could not be simulated in this version of the code.

During the initial experiment, it was found that the best operating parameters

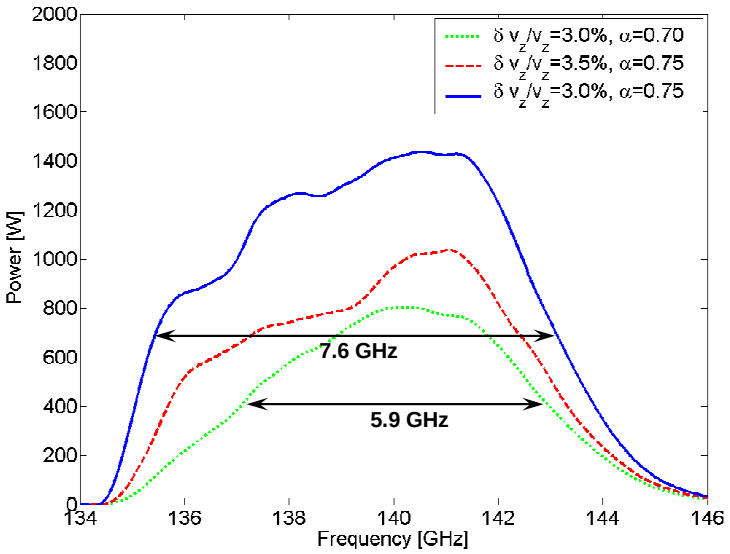

Mode	HE_{06}
V_0	40 kV
I_0	3 A
R_b	1.9 mm
B_0/B_g	0.998
$L_\perp = R_c$	7.05 mm
a	2.4 mm
Loss rate	2 dB/cm
P_{in}	10 mW

Figure 3-4: A nonlinear confocal simulation at 40 kV predicting a gain of over 50 dB and a bandwidth of around 6 to 7 GHz for various velocity spread and α conditions.

were obtained at closer to 40 kV. At 40-45 kV, the electron gun is predicted to have an α-value of 0.7 to 0.75. In addition, the interaction circuit is changed slightly to $R_c = L_\perp = 7.05$ mm to maintain the proper synchronism condition, and the current is increased to keep the perveance of the beam constant, that is, $I_1/V_1^{3/2} = I_2/V_2^{3/2}$. Fig. 3-4 shows the predicted nonlinear power output at 40 kV for several values of velocity spread. The gain is again near 50 dB, but the bandwidth is predicted to be significantly larger than at 30 kV, even in linear theory, assuming the input coupler has no limiting effect on the power coupled into the circuit. This increase in bandwidth is due to the fact that it is easier to maintain synchronism over wide bandwidth at higher voltages.

3.4 Instabilities

There are three general types of instabilities that need to be addressed in a gyro-amplifier: Absolute instabilities, backward wave oscillation (BWO) instabilities, and reflected power instabilities. The case of the reflective instability is analogous to allowing a positive feedback path in an analog amplifier circuit. It can be minimized

by eliminating reflections traveling in the backward direction, i.e., minimizing sharp angles or flat surfaces that could reflect or diffract power back toward the input.

The BWO instabilities arise from interactions with Doppler-shifted backward propagating modes at the fundamental or harmonics of the operation frequency [96] first being treated by Wachtel and Wachtel [97] in the linear regime. BWO frequencies can be estimated from the waveguide dispersion relation and beam resonance line intersections for negative k_z values, as in Fig. 2-2. The BWO has also been analyzed in the saturated regime [98], and for tapered magnetic fields and waveguide cross section [99]. BWO instabilities can be reduced by employing a mode selective structure such that the backward propagating modes are heavily attenuated. As we have shown in Sec. 2.2.3, the confocal structure can effectively filter out many of these unwanted backward wave modes.

The absolute instability is a function of the electron beam to electromagnetic wave coupling in the device. Above the critical threshold for absolute instability, the wave amplitude grows in time (complex frequency, ω), as opposed to the convective instability, which grows in space (complex wavenumber, k), assuming the waves propagate according to $\exp[j(\omega t - kz)]$. Adding loss to the circuit, via severs, absorbers, etc., reduces the susceptibility to absolute and reflective oscillations. The threshold for absolute instability is generally obtained from complex roots of the fourth-order dispersion relation [53].

3.4.1 BWO Instability

The BWO oscillation occurs due to a backward waveguide mode synchronous with a cyclotron beam mode, setting up an internal feedback mechanism. The BWO starting conditions are usually estimated via 2-D root search of the dispersion relation of the device for frequency and wavenumber [65]. It is known that the oscillation starting conditions become more sensitive near cutoff ($k_z \approx 0$), and are a function of the matching conditions at the output [96].

The BWO threshold was calculated using the formalism developed in the above sections. By the substitutions $I_0' \rightarrow -I_0'$ and $b \rightarrow -b$ in Eqn. 3.14, the BWO equation

can be written in the form,

$$\bar{\gamma}^2(\bar{\gamma} - \tilde{\Delta}) - 1 = 0 \tag{3.21}$$

where $\bar{\gamma} = \Gamma/(I_0'\bar{\mu})^{1/3}$, and $\tilde{\Delta} = \bar{\Delta}/(I_0'\bar{\mu})^{1/3}$. The term linear in $\bar{\gamma}$ has been omitted because it is negligibly small. The conditions for oscillation occur when the three roots of Eqn. 3.21 cause the corresponding three waves to sum to zero at the end of the BWO tube, equivalent to giving rise to an infinite gain. For the case of a lossless BWO with velocity spread neglected, the solutions for critical oscillation threshold reduce to [100],

$$\begin{aligned} (kL)(I_0'\bar{\mu})^{1/3} &= 1.98 \\ \bar{\Delta}(I_0'\bar{\mu})^{-1/3} &= 1.52 \end{aligned}$$

Figure 3-5 shows the critical oscillation start current versus the length of the circuit for the confocal case with a variety of mirror aperture sizes a. The start current is proportional to approximately $1/L^3$, where L is the length of the circuit.

3.4.2 Absolute Instability

An absolute instability calculation method can be found in [91], where the linear dispersion relation of Eqn. 3.8 with a cold beam (no velocity spread) can be solved for the roots $\omega_n, n = 1, 2, 3$. Velocity spread can be neglected because it will only raise the start current value, leading to a possible false sense of security.

Absolute instability roots form a saddle point that obeys the following conditions,

$$\begin{aligned} D(\omega_n, k_{zn}) &= 0 \\ \left.\frac{\delta D}{\delta k_z}\right|_{\omega_n, k_{zn}} &= 0 \end{aligned}$$

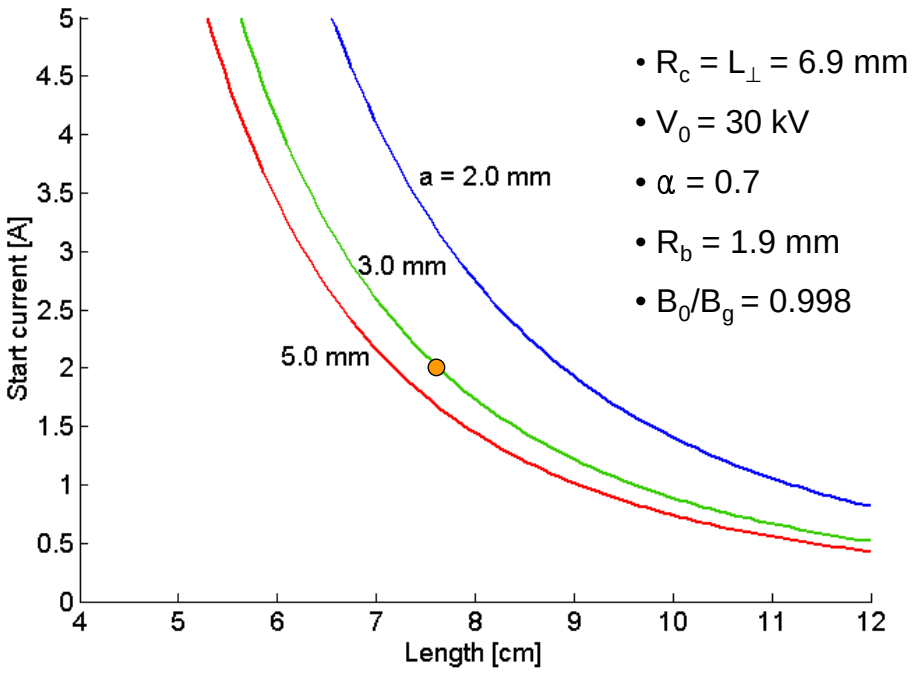

Figure 3-5: Calculated BWO oscillation start current thresholds versus circuit length under the conditions shown for various mirror apertures a. The dot indicates that a 2 A beam current limits the circuit length to about 7.5 cm or less at 30 kV.

The analytic expression for the saddle point can be written as,

$$\begin{aligned} \omega_s &= \frac{\omega_c}{1+8\beta_{z0}^2}\left\{\frac{B_0}{B_g}+\left[8\beta_{z0}^2\left(1-\frac{B_0^2}{B_g^2}\right)+64\beta_{z0}^4\right]^{1/2}\right\} \\ k_{zs} &= \frac{k_{mn}}{4\beta_{z0}}\left(\frac{\omega_s}{\omega_c}-\frac{B_0}{B_g}\right) \end{aligned}$$

for $\delta = 0$, and ignoring T_{sm} and U_{sm} in Eqn. 3.8. The k_{zs} roots in the saddle point split from a double root into two roots for $\omega = \omega_s + i\sigma$ as $\sigma \to \infty$, providing a convenient graphical method for determining the onset of instability. In Fig. 3-6, the real and imaginary roots of k_z are plotted for the TE_{03} cylindrical waveguide mode at 30 kV with $\alpha = 0.75$ at two different beam current values: 25 A below the absolute instability threshold, and 32 A above the threshold. Note that two of the real k_z roots merge in going from Fig. 3-6(a) to Fig. 3-6(d), while the imaginary parts split from (b) to (e), indicating that the actual saddle point for the onset of oscillation is somewhere in between 25 A and 32 A.

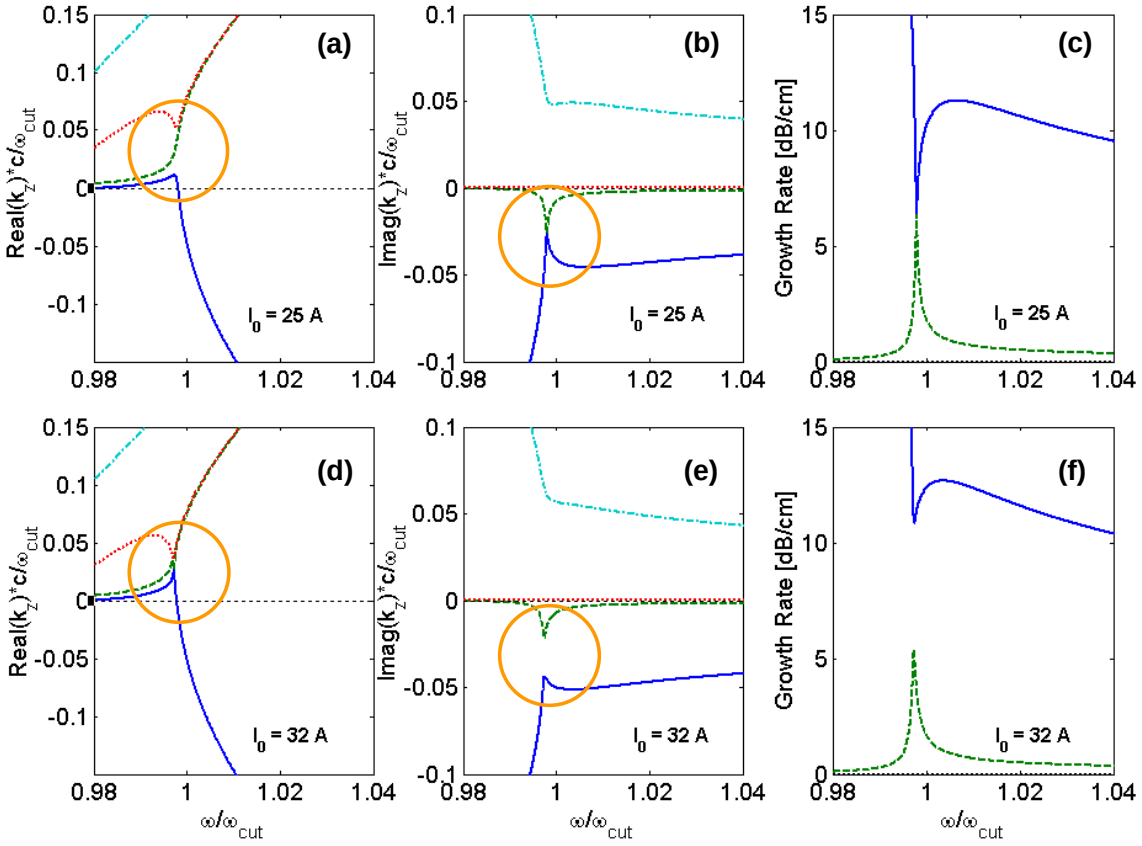

Figure 3-6: Plots of the roots of $D(w, k_z) = 0$ for a lossy circuit with $r_{cav} = 3.62mm$ for the TE_{03} mode with 30 kV, $\alpha = 0.75$ and $B_0/B_g = 0.997$. For $I_0 = 25$ A: (a) Real part of k_z, (b) Imaginary part of k_z, (c) estimated growth rate. (d-f) for 30 A. The circles indicate where the key roots split and merge.

While the absolute instability may be of legitimate concern in short, high power devices that have low losses, it is clear that the starting current is very high at over 25 A in the TE_{03} circuit, and therefore is not important compared to the backward wave oscillation thresholds described above. The confocal HE_{06} and cylindrical TE_{03} modes both have three electric field variations from the center of the waveguide to the mirror surfaces, and the electron beam has been positioned to interact with the intermediate maxima in both cases. Since the HE_{06} confocal circuit is more lossy than the closed TE_{03} cylindrical one, an even higher absolute instability start current for the confocal system can be expected.

3.4.3 Feedback Instabilities

A critical factor in the stability of an amplifier such as the gyro-TWA is limiting back-reflected power. A wave that is reflected backward into the circuit may easily trigger a feedback oscillation depending on the frequency and phase.

Typical features that could cause a reflection include sharp or sudden changes in the waveguide profile, downtapers to the electromagnetic fields, flat surfaces that might reflect or focus power in the backward direction, windows, and even mirrors or other materials placed outside of the vacuum tube itself. Such candidates for reflection must be avoided at all cost since even a reflection of -30 dB could limit the gain of the device to 30 dB due to the onset of oscillation. Feedback oscillations are extremely difficult to predict in simulation in the most relevant cases, like windows, because they require one to model the entire vacuum tube, which may be hundreds of even thousands of wavelengths long.

Some possible solutions to preventing feedback include Brewster windows, double-disc output windows, addition of MMW absorbing lining material inside the vacuum jacket to reduce stray radiation, and elimination of all surfaces perpendicular to the Poynting vector flows. In the actual experiment (Chap. 4), the addition of a double disc window greatly reduced oscillations and allowed regions of higher gain to be accessed.

3.5 Discussion

In this chapter, the interaction theory for the confocal structure has been described in detail. A linear dispersion relation including velocity spread has been introduced, and a linear theory showed that growth rates of 3 to 4 dB/cm could be realized in the confocal amplifier circuit. A nonlinear theory has been used to show that gain of up to 50 dB and bandwidths of up to 4 GHz or more are possible for a confocal circuit with ideal alignment and low velocity spreads. In addition, the tradeoff between backward oscillation start current and circuit interaction length was investigated along with a simple means for stabilizing the amplifier by varying the mirror aperture size, a. It was found that a 7 cm circuit would be stable for up to 2 A of beam current, and this led to a three-stage amplifier design verified in nonlinear simulation. It was shown that the absolute instability is not of concern for this kind of circuit.

Chapter 4

Gyro-Amplifier Experiment

In this chapter, I describe the 140 GHz confocal gyro-TWT amplifier experiment in detail and analyze the experimental results. This confocal amplifier circuit was fabricated as an amplifier with three 7 cm stages with $R_c = 6.90\ mm$ and a loss rate of approximately 2 dB/cm to stabilize against backward wave oscillations. The collector tube functions as an output waveguide for the TE_{03} mode, bypassing the lengthy mode converter design and fabrication process.

4.1 Scope of Experiment

The drive power for the amplifier experiment was supplied by a 140 GHz Extended Interaction Klystron (EIK) capable of generating pulses from about 4 ns full-width, half-maximum (FWHM) up to 2 μs in duration, at up to 150 W over the frequency range 139.2 GHz to 142 GHz. This source was not capable of generating pulses under 4 ns FWHM, so it was not possible to test the amplifier down to 1 ns or below. These pulses were passed through a simple diagnostic system before being injected into the amplifier. A photo of this system is shown in Fig. 4-1, and the corresponding block diagram is shown in detail in Fig. 4-2. The corresponding parts are cataloged by manufacturer part number and serial number in Table 4.1. The main power supply was a discrete transmission line-based modulator built at MIT capable of 5 μs pulses at up to about 45 kV (break down limit without oil) and easily several amps of current

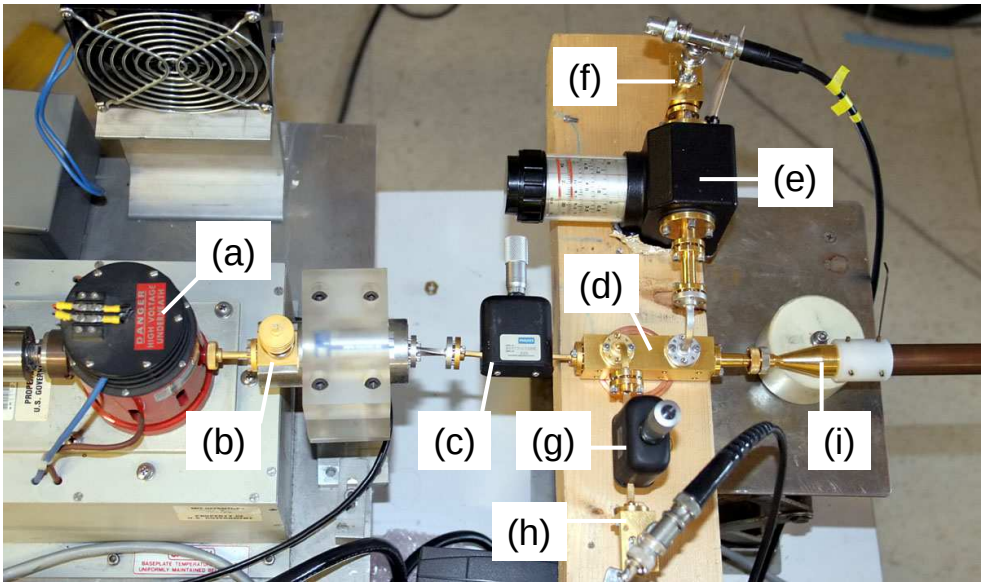

Figure 4-1: Front end system components: (a) Tunable EIK source, (b) Circulator, (c) Attenuator #1, (d) -20 dB coupler, (e) Attenuator #3, (f) Forward diode, (g) Attenuator #2, (h) Reflected diode, (i) Circular uptaper.

with a repetition rate of up to around 10 Hz. It also supplies the heater current for the electron gun.

4.2 System Components

In this section, the major components involved in the experiment are described in detail.

Table 4.1: System Components

Part	*Manufacturer*	*Model*	*SerialNumber*
Attenuator # 1	Hughes	45737H-1200	029
Attenuator # 2	MRI	ATVF-00	103
Attenuator # 3	Hughes	45728H-1000	084
-20 dB coupler	Custom Microwave	–	–
Forward Diode	–	HFD08P	2K09102
Reflected Diode	–	HFD07P	2K112135
Output Diode	Pacific Millimeter	WD	613
Output Attenuator	Dorado	VA-10	20104

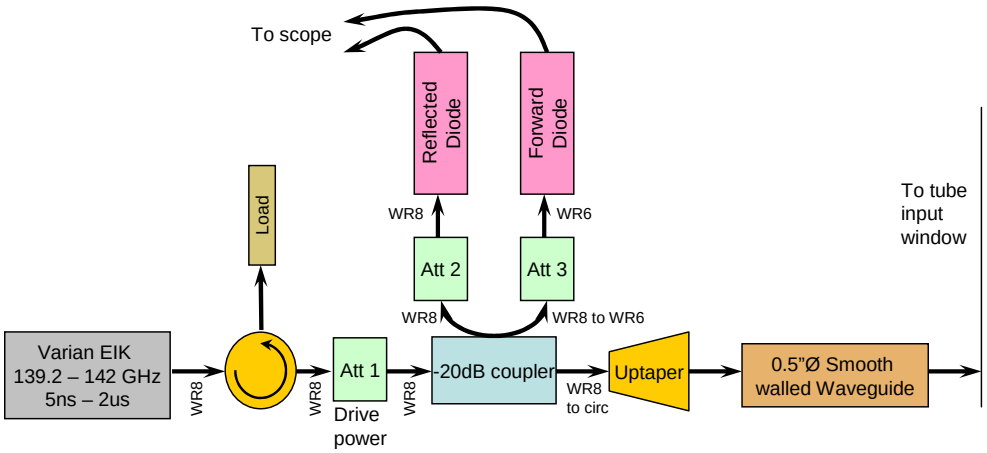

Figure 4-2: Block diagram of the front end of the gyro-amplifier experiment.

4.2.1 The Superconducting Magnet

The high precision superconducting magnet for this experiment was obtained from Magnex Scientific, LLC. The maximum field strength is 6.2 T with a ±0.5% uniform length of 28 cm. The magnet has a horizontal 12.7 cm diameter, room-temperature bore with a flange at one end for mounting the external, copper gun coil. A unique feature of this magnet is that it is actively shielded such that the magnetic field falls off as $B_z \sim 1/z^4$ in the vicinity of the cathode. Fig. 4-3 shows the predicted magnetic field profile along with the fall-off exponent of the field strength.

4.2.2 Electron Gun

A Varian VUW-8140 double-anode electron gun was used in this experiment. The electron gun was centered in the external copper gun coil, used for adjusting the gun performance and for beam focusing. This gun was designed for operation at 65 kV, but simulations predicted reasonable operation at 30 kV. The simulations were performed using EGUN version EGN2w, a 32-bit Windows/DOS command-line executable program [101]. Figure 4-4 shows magnetic compression and axial field profiles for several settings of gun coil current. The gun coil produces a maximum of 0.11 T at 250 A, though it is typically used at under ±60 A in the experiment. Figure 4-5 shows the theoretical electron guiding centers assuming an adiabatically

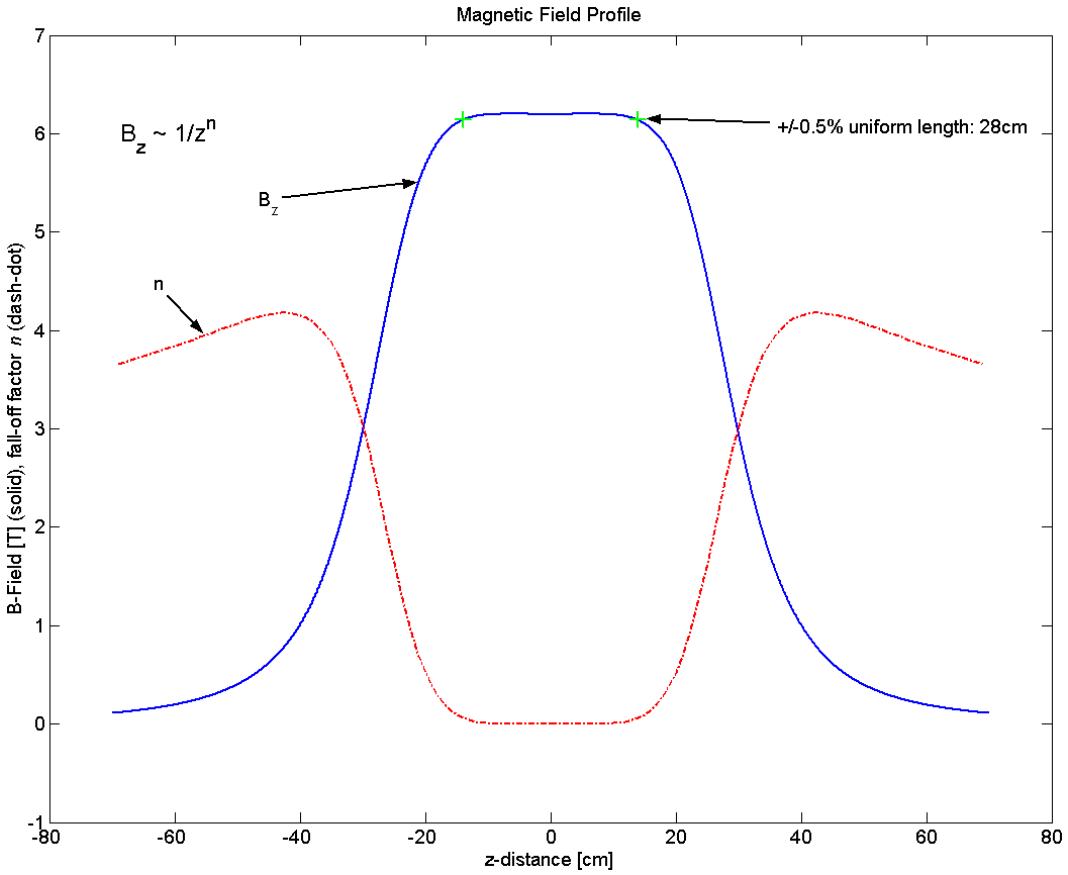

Figure 4-3: The predicted magnetic field profile shown at the rated maximum field strength of 6.2 T. The $\pm 0.5\%$ uniform field length is 28 cm and the field falls off as roughly $B_z \sim 1/z^4$ in the vicinity of the cathode, which is located at $z = -55\ cm$.

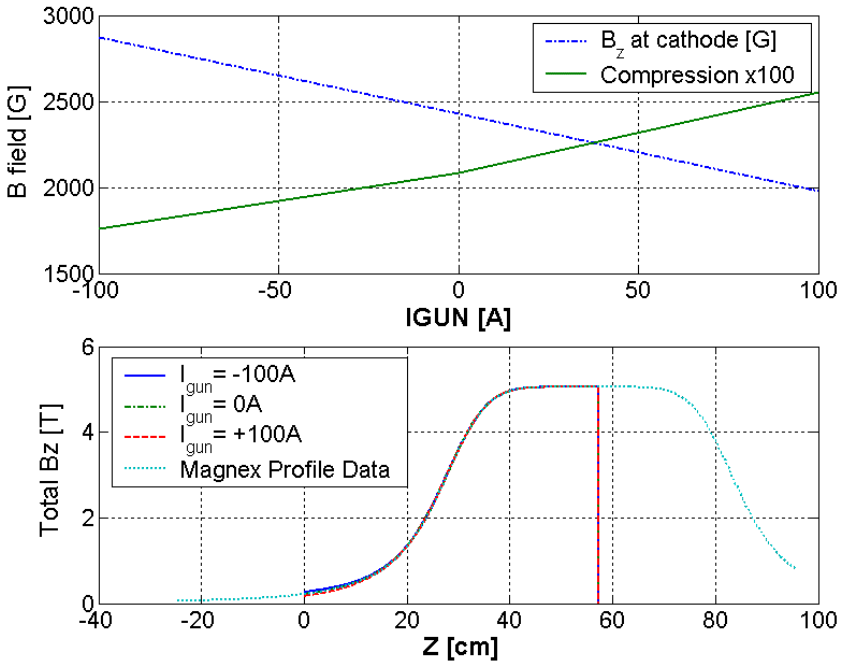

Figure 4-4: (top) Comparison of B_z cathode magnetic field and magnetic compression (magnified by 100x) vs. current I_{gun} in the external gun coil. (bottom) Axial magnetic field profile used by EGUN for several values of I_{gun}, including a data curve from Magnex showing perfect agreement with $I_{gun} = 0A$. In this plot, $z = 1.61\ cm$ is the cathode position.

compressed electron beam.

During the experimental optimization, however, it was discovered that the best operating points were obtained at higher voltages, above 35 kV. As an aid, contour maps of the electron gun performance generated by EGUN for a variety of gun coil currents are shown in Appendix C. These maps show that higher voltage in the range of 40-45 kV is required to achieve α-values of 0.7 to 0.75 at low velocity spreads.

The original gun operating point was chosen at 30 kV, with an intended operating point of $\alpha = 0.75$ and expected perpendicular optical velocity spread of $\delta v_\perp / v_\perp \approx 2\%$ (for a total velocity spread of approximately 6%). It was then found that the best operating parameters gravitated toward higher voltage. Eventually, the best operating point was found at around 38 kV at 2.7 A, $\alpha \approx 0.55$ (for a tuned mirror spacing of $L_\perp = 6.82$ mm), but it seems that this value was reached more because the perpendicular velocity spread found a local minimum rather than the α value

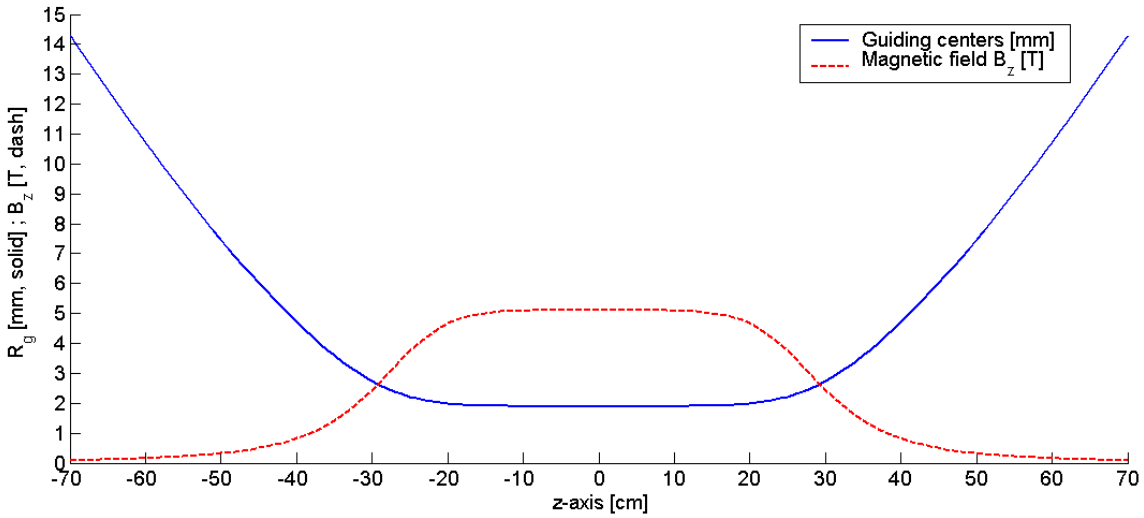

Figure 4-5: The theoretical electron guiding center trajectories assuming adiabatic compression following the magnetic field profile. The beam radius in the circuit is $r_b = 1.9mm$. In this plot, $z = 0$ cm refers to the center of the magnetic flat field.

actually being optimal. According to nonlinear simulations, higher α values in the range of 0.7 to 0.75 are required for high gain and high peak output power, and it has been observed in the experiment that velocity spread has a profound effect on the gain and bandwidth. It is estimated that the actual total perpendicular velocity spread in the experiment is in the range of 8% to 10%.

The voltage supply for the mod-anode on the electron gun is provided by a series of taps on a resistor voltage divider. The mod-anode voltage V_{MA} is related to the cathode voltage V_k and the tap number N_{TAP} (valid to within ± 0.3 % accuracy) by,

$$\frac{V_{MA}}{V_k} = -0.00496 N_{TAP} + 0.790 \tag{4.1}$$

4.2.3 Sources of Velocity Spread

It is important to remember that EGUN predicts only the optical velocity spread (designated by a subscripted "O" below). The total velocity spread can be estimated by including thermal spread ("T"), roughness ("R"), and alignment ("A"), assuming the sources are statistically independent. Estimates for thermal and roughness values

were given by Tsimring [102]:

$$\left(\frac{\delta v_\perp}{v_\perp}\right)_T = \left[\frac{KT_c}{m_o}\frac{F_m}{\gamma_o}\right]^{1/2}\frac{1}{v_{\perp o}} \tag{4.2}$$

$$\left(\frac{\delta v_\perp}{v_\perp}\right)_R = 0.4\left[\frac{2eE_cR}{m_o}\frac{F_m}{\gamma_o}\right]^{1/2}\frac{1}{v_{\perp o}} \tag{4.3}$$

where K is Boltzmann's constant, T_c is the cathode temperature in Kelvin, R is the radius of a small hemispherical bump characteristic of the cathode roughness, and F_m is the magnetic compression. The spreads are estimates of the standard deviations of the velocities such that the average spread width would be given by $\pm(\delta v_\perp/v_\perp)$.

These velocity spreads due to optical, thermal, roughness effects and misalignment combine orthogonally,

$$\left(\frac{\delta v_\perp}{v_\perp}\right)_{total} = \left[\left(\frac{\delta v_\perp}{v_\perp}\right)_O^2 + \left(\frac{\delta v_\perp}{v_\perp}\right)_T^2 + \left(\frac{\delta v_\perp}{v_\perp}\right)_R^2 + \left(\frac{\delta v_\perp}{v_\perp}\right)_A^2 + \ldots\right]^{1/2} \tag{4.4}$$

Generally, one can expect the total spread to be at least double that of the optical spread when the roughness and thermal spreads are included. The total perpendicular spread of 8% might be assumed under the best electron gun operating conditions for this experiment. It has been estimated that surface roughness is the dominant contribution to total velocity spread and can account for as much as 6% of the total spread [103].

4.2.4 Power Supply

The power supply consists of a 12-element L/C transmission line Pulse Forming Network (PFN) charged by a high voltage Spellman power supply and triggered by a thyristor. The voltage is stepped up through a 6:1 turns ratio short pulse high voltage transformer. In the series PFN configuration, the flat top pulse length is about 4 μs with a $\pm 1\%$ voltage flat top. The PFN can be configured in parallel for a shorter pulse (about 1.5 μs to 2 μs), which may be advantageous to reach higher pulse rates, but noise on the front edge of the pulse tended to cause oscillations at high gain.

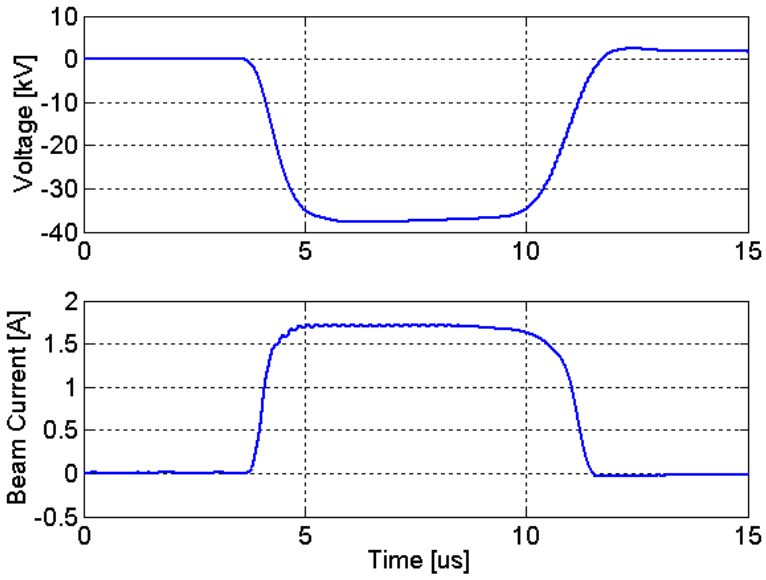

Figure 4-6: Typical oscilloscope traces of the cathode voltage and total beam current at the full voltage of 37 kV. The voltage pulse is flat to within 1% for a 4 μs pulse.

Figure 4-6 shows some typical pulse traces from the modulator supply in the 4 μs configuration with a 20 MHz bandwidth limit on the scope and an additional external filter circuit on the current trace with a cutoff frequency of 5 MHz.

In Fig. 4-7, a schematic of the power supply transformer tank is shown, featuring the resistive voltage divider that is used to supply the voltage for the mod-anode terminal of the electron gun. The mod-anode voltage is given as a function of the Tap number in Eqn. 4.1.

4.2.5 Tube Assembly

A cutaway view of the tube assembly is show in Fig. 4-8. The power enters through a side-facing 0.5" diameter, 0.1290" thick window made of Corning 7940 optical glass, which is designed to be transparent at 140 GHz. The millimeter wave (MMW) power then propagates into an overmoded 0.5" diameter copper smooth-walled waveguide in the TE_{11} mode. Near the input of the amplifier, a downtaper guides the MMW input into a short section of fundamental WR8 waveguide with a 90° H-plane bend. After the amplification in the HE_{06} mode, the power is converted through a nonlinear

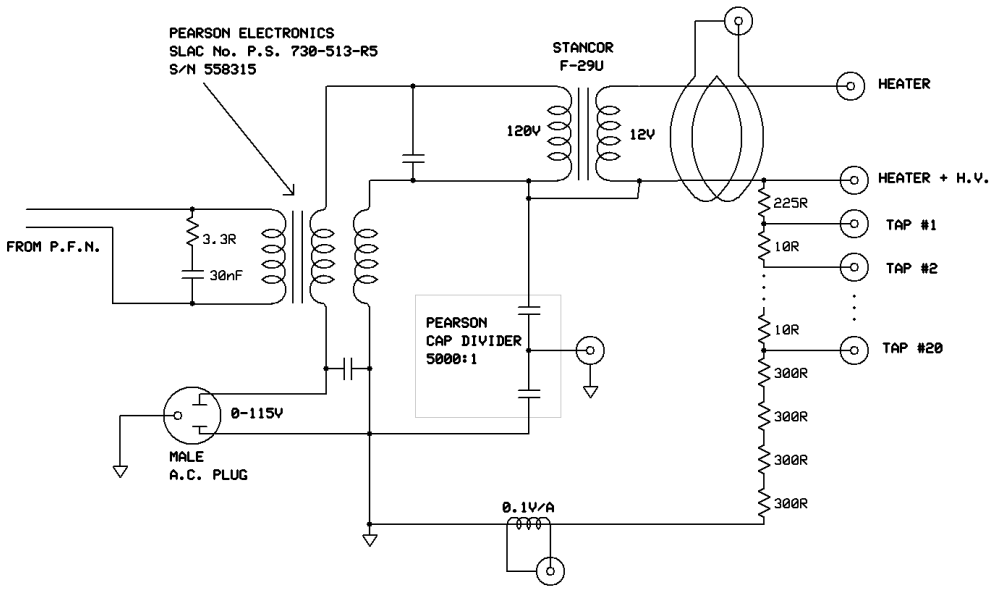

Figure 4-7: A schematic of the power supply transformer tank, including the resistive tap divider that supplies the mod-anode voltage.

uptaper into a TE_{03}-like mode.

The electron beam enters the tube from the left side of the figure, passes through an alpha-probe, followed by the amplifier circuit. The spent electron beam is finally collected on the collector pipe, which doubles as the output waveguide.

The output window is a 0.1290" thick Corning 7940 glass window. The window was measured on the F-band (90-147 GHz) Vector Network Analyzer (VNA) to be transparent at 140 GHz and 116 GHz, but a strong reflection of around 30% at 128 GHz is also present. Figure 4-9 shows the transmission of the window as measured. The theoretical fit [104] to ϵ_r is around 3.82, which matches the given value of 3.825.

A spare input window was used to create a tunable double-disc output window that reduced parasitic oscillations at 125-129 GHz, thus allowing higher gain at 140 GHz. Using a recursive algorithm for calculating arbitrary etalon structures [105], a script was written to calculate the reflection of an arbitrary interface or series of interfaces for a given incident MMW wave. Figure 4-10 shows reflectivity versus frequency for the case of a single output window and several configurations of a double output window.

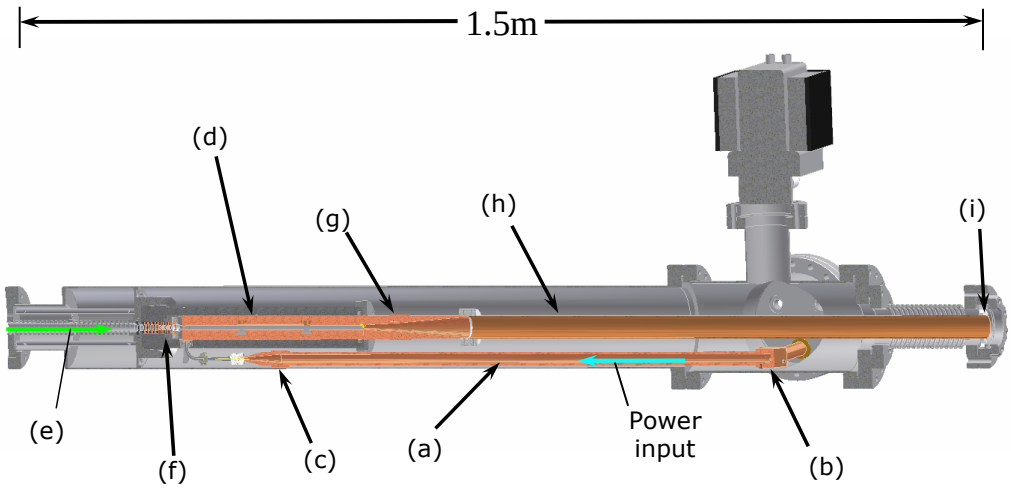

Figure 4-8: A cutaway view of the tube showing (a) Input overmoded TE_{11} waveguide, (b) miter bend, (c) downtaper, (d) amplifier circuit, (e) electron beam, (f) beam tunnel and alpha-probe location, (g) nonlinear uptaper, (h) collector/output waveguide, (i) output window.

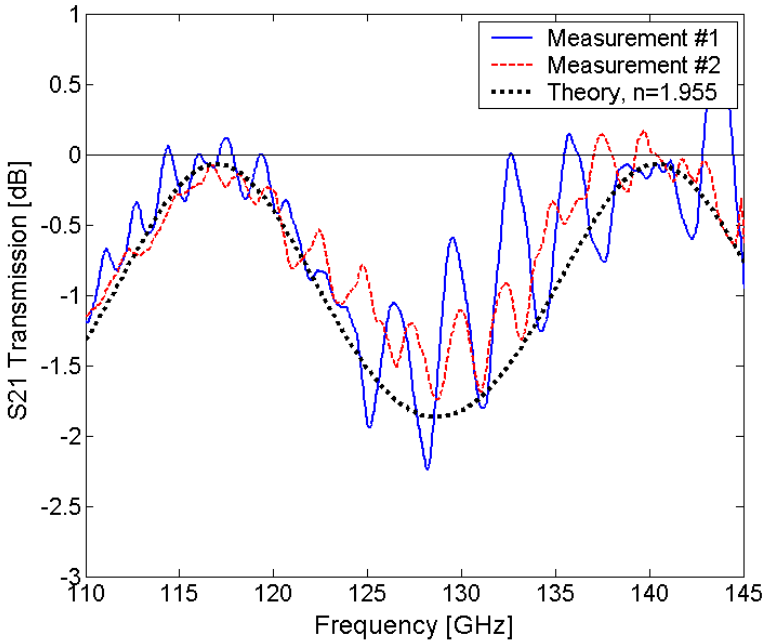

Figure 4-9: F-band VNA measurement of the window transmission. The window was placed between two horns for normal incidence.

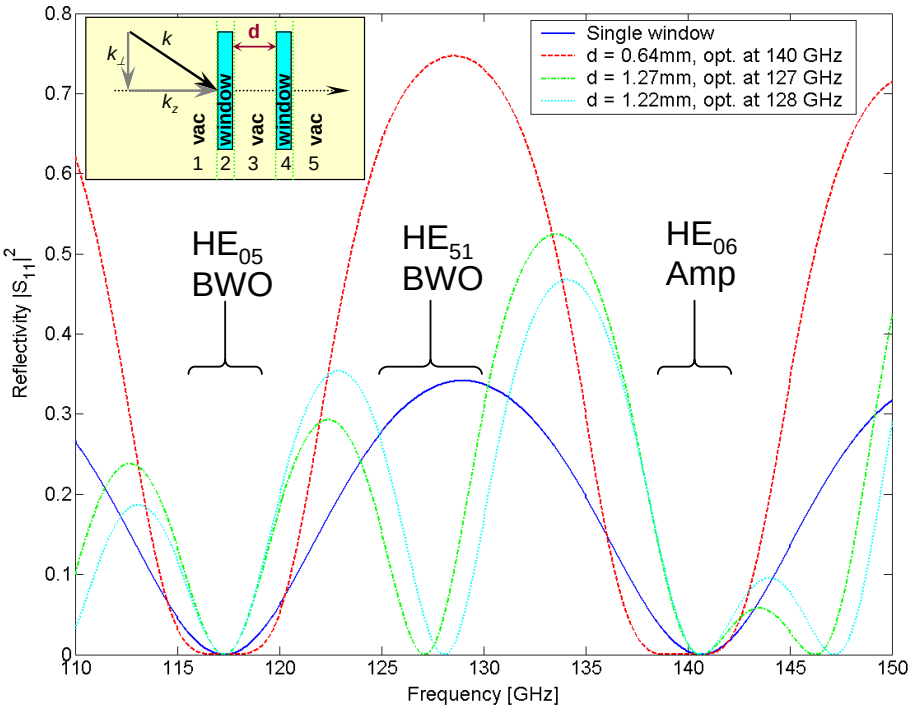

Figure 4-10: Calculation of window reflection versus frequency in the TE_{03} mode for the case of a single 0.1290" thick window, and for two windows separated by distance d. The double window can be used to widen bandwidth at 140 GHz, or can be made transparent at arbitrary frequencies around 125-130 GHz.

The double window can either be used to widen the bandwidth at 140 GHz, with a concomitant increase in reflectivity at 125-130 GHz, or it can be used to arbitrarily tune transparency in the 125-130 GHz range while maintaining good transmission at 116 GHz (HE_{05} mode BWO) and 140 GHz (HE_{06} mode forward wave). As it turned out in the experiment, strong oscillations in the 125-130 GHz band were observed at beam current above 2.5 A until the double window was included. It is important to have low reflection from any surface downstream of the amplifier to prevent oscillations by feedback. In the experiment, a spacing d of approximately 1.2 mm was needed to reduce feedback oscillations around 125 to 129 GHz in order to access higher gain.

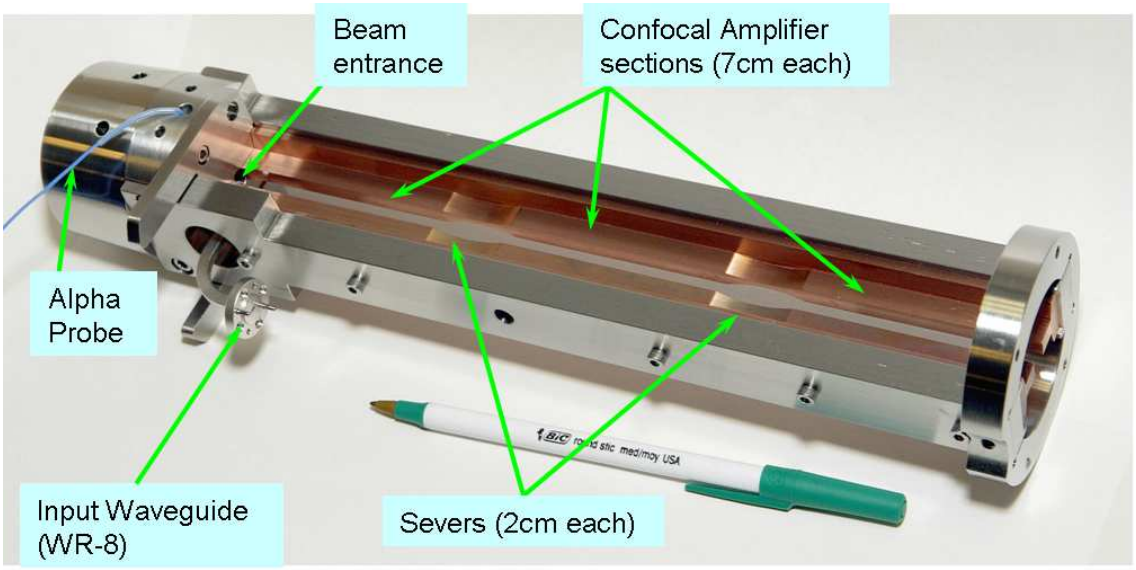

Figure 4-11: A photo of the amplifier circuit prior to installation. The amplifier consists of three 7 cm amplifier sections separated by two 2 cm severs.

4.2.6 Interaction Circuit

A photo of the finished interaction circuit prior to installation is shown in Fig. 4-11. The amplifier consists of three 7 cm long interaction circuits separated by two 2 cm quasi-optical severs. The severs are made by simply narrowing down the mirror aperture such that the MMW power leaks out completely by diffraction. An α-probe ring provides an estimate of the α-value [106], but the measurement has very high error for low α-values.

While the shimming was being performed for this version of the circuit, a bead-pull technique was used to verify that the six variations in the HE_{06} mode were indeed being excited. This test was performed by sliding a thin rod of pencil lead across the confocal waveguide cross section in the vicinity of the input coupler. During this test, it was noted that the bandwidth of the perturbation extended only 1.5 GHz, instead of the 5 GHz predicted by an HFSS simulation. Measurement of perpendicular spacing of the whole amplifier circuit were performed using a precision caliper designed for measuring internal curved surfaces. The measurement revealed significant irregularity in the tuning of the first amplifier section on the order of $\pm 30 \mu m$ that could not be

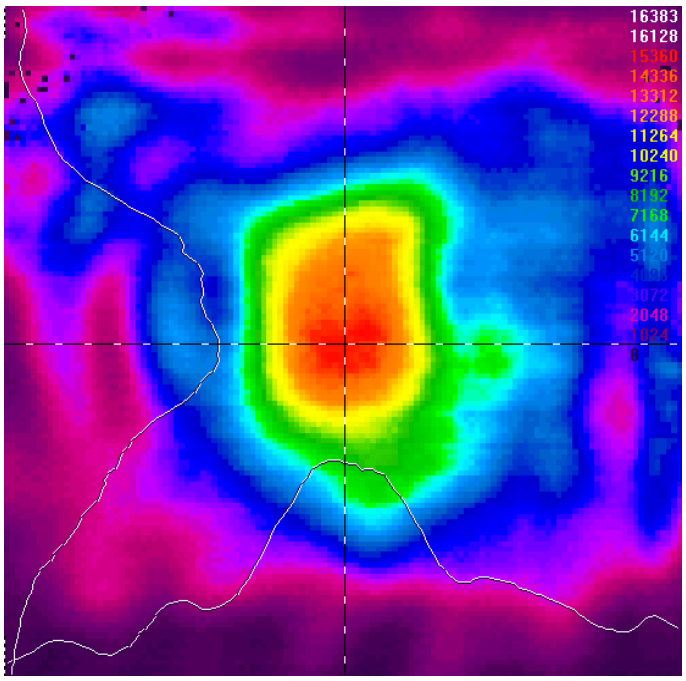

Figure 4-12: MMW field pattern at the end of the 1.85 m long, 0.5" I.D. copper waveguide showing a clean TE_{11} mode at the input to the tube. The pyroelectric camera sensor is 0.5" x 0.5".

corrected by mere shims. The largest spacing error occurred at the location of input waveguide, because the input waveguide was soldered in place after the circuit was machined and was not perfectly coplanar with the mirror curvature. This resulted in a small resonant volume near the coupler and a sharp reduction of coupling. This could be corrected by mounting the input waveguide before the mirror surface is machined. Ultimately, these irregularities led to a narrowing of coupling bandwidth and a reduction of gain due to non-uniform tuning. The last two sections of the amplifier measured within $\Delta L_{\perp} \approx 10\mu m$.

The MMW field pattern was measured at the end of the copper input transmission line using the PyroCam III from Spiricon, Inc. [107]. Figure 4-12 shows this mode pattern to be slightly elliptical, as expected.

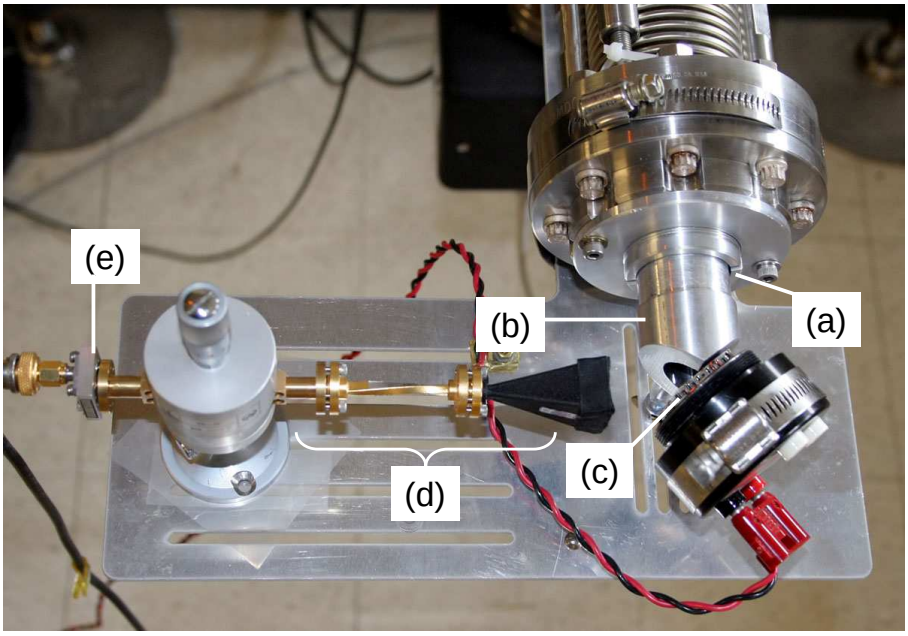

Figure 4-13: Output diagnostics: (a) Tunable double disc window fixture, (b) Downtaper, (c) Calorimeter, (d) Horn, polarization twist and attenuator, (e) Output diode. Not shown: Frequency system picks up stray radiation 2 m away.

4.3 Measurement Tools

Photo 4-13 shows the diagnostics mounted at the output of the tube. The power exits the vacuum through a tunable double-disc window followed by a slight downtaper to focus the fields on the 1" calorimeter head. The angle of the calorimeter head prevents the power from reflecting straight back into the tube and also allows the output diode to measure the pulse shape concurrent with the power measurement. In addition to the simultaneous power and pulse shape measurements, the stray power reflected from the calorimeter was simultaneously measured on the frequency system.

A Scientech model 360-001 (serial number 2213) 1" calorimeter was used in conjunction with a Scientech model 362 (serial number 2181) meter box for accurate measurement of the MMW power. The meter has set ranges going down to the 1 mW scale and independent adjustments for each scale. The calorimeter was calibrated at each power setting using the built-in resistive heater along with a volt-meter and current-meter to get an accurate reading of the power applied to the resistor. Each

setting was calibrated according to the user manual over a wide range of applied power to ensure linearity and this gave a calibration factor to each power scale. In addition, it was assumed that approximately 85 % of the incident power was absorbed in the MMW bands, which is a fairly conservative value. For power measurement, the pulse rate was typically set at around 5 Hz, rather than around 2 Hz in normal operation. A plastic bag placed over the output diagnostics eliminates power fluctuations due to air currents.

For the system configuration in Fig. 4-2, the forward diode was calibrated for input power by removing the copper transmission line and inserting the calorimeter. This calibration gave an accurate measure of the power into the copper waveguide. To keep the diode power to a reasonable level under all circumstances, Attenuator # 3 in Fig. 4-2 was used to limit the incident power such that the diode signal was always around the 10 mV level. Attenuator # 3 was calibrated on the VNA for both loss and frequency, and a MATLAB script was implemented to accurately translate the peak diode signal into an input power level for any given frequency and attenuator setting. The diode was finally loaded with a 50 Ω resistor for fast transient response below 1 ns, and to eliminate reflections caused by mismatches at the ends of the coax cables. The reflected diode detector was not calibrated and was only used as an indication of reflections and backward wave oscillations.

For the output side of the system, the output diode was used primarily to monitor pulse shape, but could also be calibrated for power at a given frequency. The peak diode signal varied as a strong function of angle and distance from the output window as well as polarization. As a consequence, the peak values also varied with frequency, so recalibration was required at each frequency for an accurate absolute power measurement. This diode was also loaded with a 50 Ω resistor for fast response.

A heterodyning receiver system was used for the frequency measurement. Since the system was very sensitive, it could easily be located 2 m from the magnet and pick up stray radiation scattered from the calorimeter head. Routine frequency measurement accuracy is within 1 MHz.

4.4 Experimental Results

The experiment achieved over 1.5 GHz of bandwidth, over 820 W consistently, and up to 34 dB linear gain from the interaction circuit. The characteristics of the amplifier are presented and analyzed below.

The experiment went through several phases of tuning where the perpendicular spacing $L_\perp$ was adjusted before settling on the final results presented here. Initially, the spacing was adjusted by shimming the circuit until the S_{11} value on the VNA gave a strong dip near 140 GHz, indicating good coupling. HFSS simulations, however, predicted a broadband dip in S_{11} that could not be found through shimming. On further investigation, it was found that the irregularities in the first section of the amplifier produced a resonant cavity that, when modeled in HFSS, produced distinct sharp dips in S_{11} not unlike what was observed on the VNA. Even deviations as small as $20 - 30\mu m$ were enough to impact the coupling efficiency significantly. Finally, a perturbation technique was employed instead to ensure the MMW were reaching several centimeters into the first amplifier section in the correct frequency range.

4.4.1 Saturated Characteristics

Since the input source was capable of generating power on the order of 100 W, corresponding to approximately 10 W coupling into the amplifier circuit, it was not difficult to measure saturated characteristics. It was even possible to overdrive the amplifier such that the output power decreased for further increases in input power.

Fig. 4-14 shows a 1.5 GHz bandwidth measurement, produced at 38.5 kV, 2.5 A, and a 5.05 T magnetic field. The simulation results matched the data best for those operating parameters assuming an input power of 0.65 W, $\alpha = 0.54$, parallel velocity spread of 3.55% (approximately 11 % perpendicular velocity spread). To mimic the bandwidth limiting effect of the coupler, the input power was Gaussian distributed with a mean of 140 GHz and FWHM of about 1.5 GHz, as observed during the perturbation measurement on the VNA. The simulation used amplifier mirror spacings $L_\perp$ of 6.83 mm, 6.81 mm, and 6.82 mm for the first, second and third amplifier

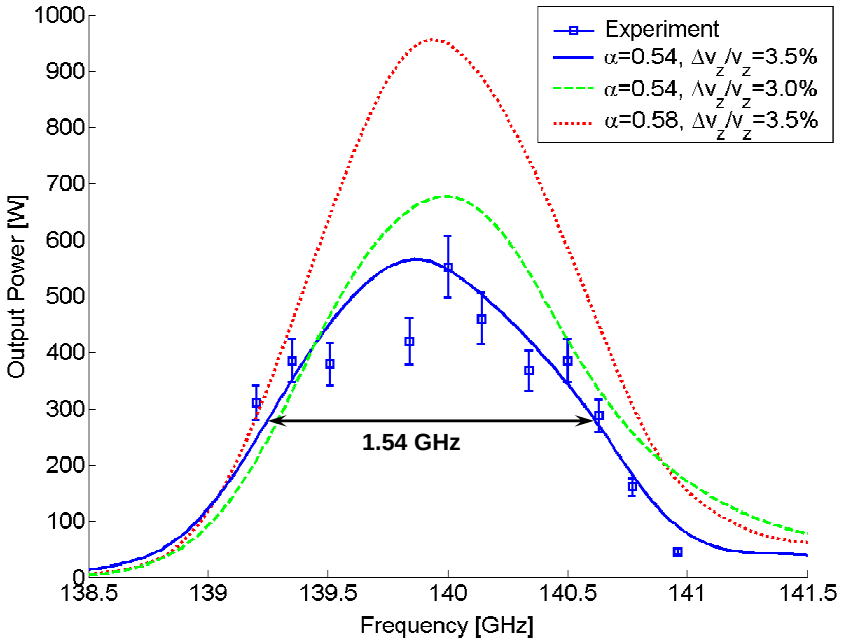

Figure 4-14: Measured peak output power (markers) and simulations (curves) at 38.5 kV, 2.5 A. The simulation fit is best for $\alpha = 0.54$, $\delta v_z/v_z = 3.55\%$. The experimental bandwidth has been measured at over 1.5 GHz.

sections, respectively, an estimated average of the spacings measured before the amplifier was installed in the tube. The simulation code was not able to handle the complex arbitrary irregularities in the first amplifier circuit. In the experiment, the measured output power peaked at 570 W, which matches with this simulation. In addition, there is a slight ripple effect noticeable on the measured data that is due to resonances in the input transmission line (discussed in Sec. 4.4.3).

The estimated power arriving at the amplifier input coupler flange based on network analyzer measurements is approximately 10 W, indicating that the electromagnetic coupling from this flange into the confocal amplifier circuit may be less efficient than expected. The ideal coupler assumes that there is no misalignment or variation in $L_\perp$ with the z-coordinate. Simulations in HFSS put the insertion loss figure at around 4 dB for an ideal structure, whereas to fit the data, a loss of around 10 dB is assumed. In the experiment, the irregularities in the first amplifier section are the order of ± 30 μm in the immediate area of the coupler, as mentioned previously, and have a strong effect on the mode structure and therefore the coupling efficiency.

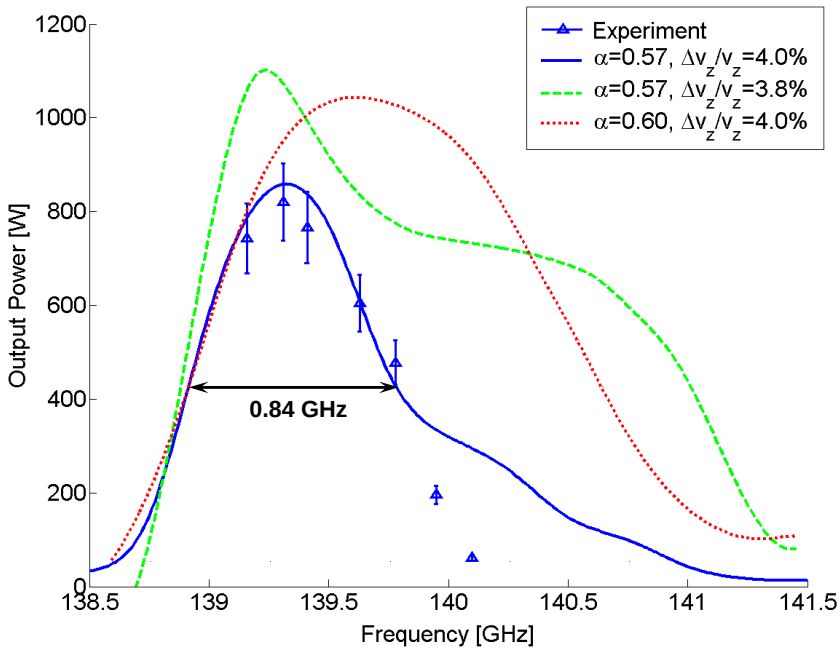

Figure 4-15: Measured peak output power (markers) and simulations (curves) at 37.7 kV, 2.7 A. The simulation fit is best for $\alpha = 0.57$, $\delta v_z/v_z = 4.0\%$. The experimental power has been measured at over 820 W.

It is not surprising, given these irregularities, that the coupling efficiency would be adversely affected.

With a slight adjustment of operating parameters to 37.7 kV, 2.70 A, 5.05 T magnetic field, and adjustment of the gun coil, the high power curve in Fig. 4-15 was produced. For $\alpha = 0.57$, an input power of 1.5 W, and a parallel velocity spread of 4.0%, the simulation agrees well with the experiment. The slightly higher alpha value used for this simulation is consistent with measured values as the gun coil current was changed between the operating parameters. The measured bandwidth was 0.8 GHz for this operating point and agrees reasonably well with the simulation, with a departure above 140 GHz possibly due to unfavorable velocity spread characteristics at the different cathode voltage.

The saturation characteristics can be seen in Fig. 4-16, where output power and gain are plotted versus input power at 139.63 GHz. The input power is an estimate from the known losses in the waveguide and simulation of the coupler performance. Saturation begins to set in at around 0.1 W of power coupled into the circuit, and

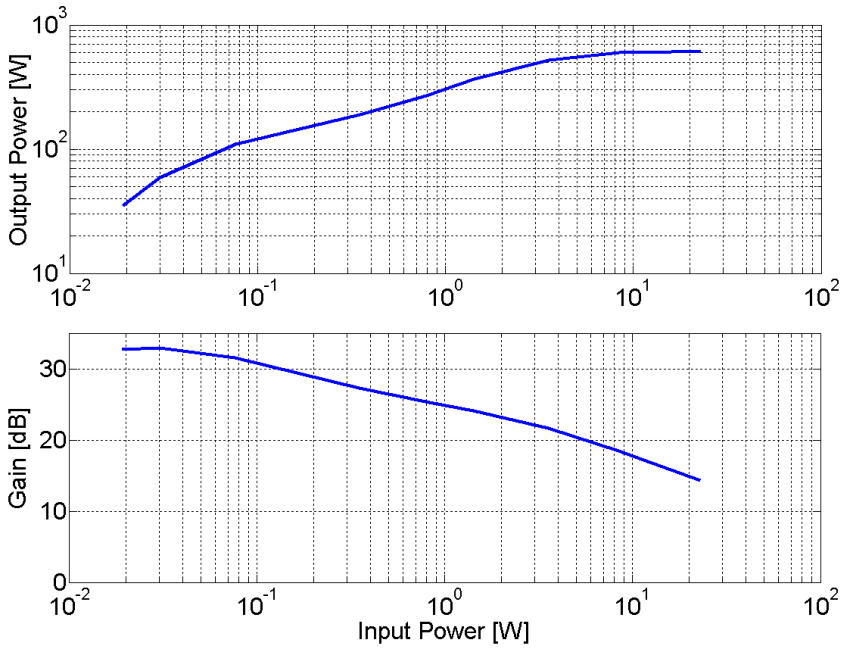

Figure 4-16: Saturation characteristics. (top) Flattening of output power. (bottom) Gain saturation. The -3 dB point occurs for about 0.1 W of power coupled into the circuit.

the peak power is reached for an input power of about 10 W.

4.4.2 Linear Gain

Linear gain is generally the most difficult to measure since it depends on measurements of both output power and input power. The best method for measuring the gain was to measure relatively high output power (100's of Watts) in the saturated regime at high input power at a given frequency in order to calibrate a video detector diode to the calorimeter. Then the input power was reduced until the output diode signal was small. Along with the calibration for the forward diode power, this gave accurate gain values at a given frequency. When the frequency is changed, however, this process has to be repeated, since the output diode calibration may depend on frequency and certainly depends on its position with respect to the output window. Figure 4-17 shows the measured linear gain versus frequency for $V_0 = 34.7\ kV$, $I_0 = 2.7\ A$, $\alpha = 0.6$, $B_0 = 5.05\ T$.

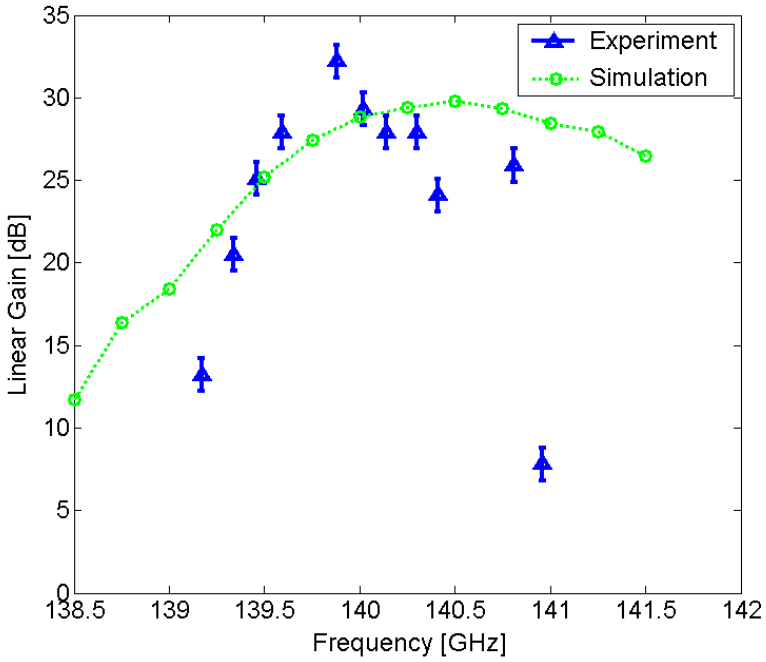

Figure 4-17: Linear Gain of the gyro-amplifier compared to simulation at 34.7 kV.

The presence of ripple on the linear gain can be explained: The input transmission line contains a downtaper and uptaper on each end of a roughly 3 m stretch of 0.5" I.D. copper waveguide. Trapped power resonates at a multitude of frequencies, and the effect can be readily seen of sharply rising and falling reflected diode signal as one sweeps through the frequency range. Thus the input power varies significantly with frequency, leading to an apparent ripple in gain. This variance with frequency is readily apparent while observing the reflected diode signal. In addition, there may be some resonant reflections from the output window due to higher order modes in the output waveguide.

4.4.3 Short Pulses

While the EIK was not capable of generating pulses under 4 ns, it was still found that the short pulses could be used for time-domain reflectometry. In order to make sense of the TDR signals, it was necessary to estimate the propagation delays for each section of the amplifier system. Figure 4-18 shows detailed timing estimations

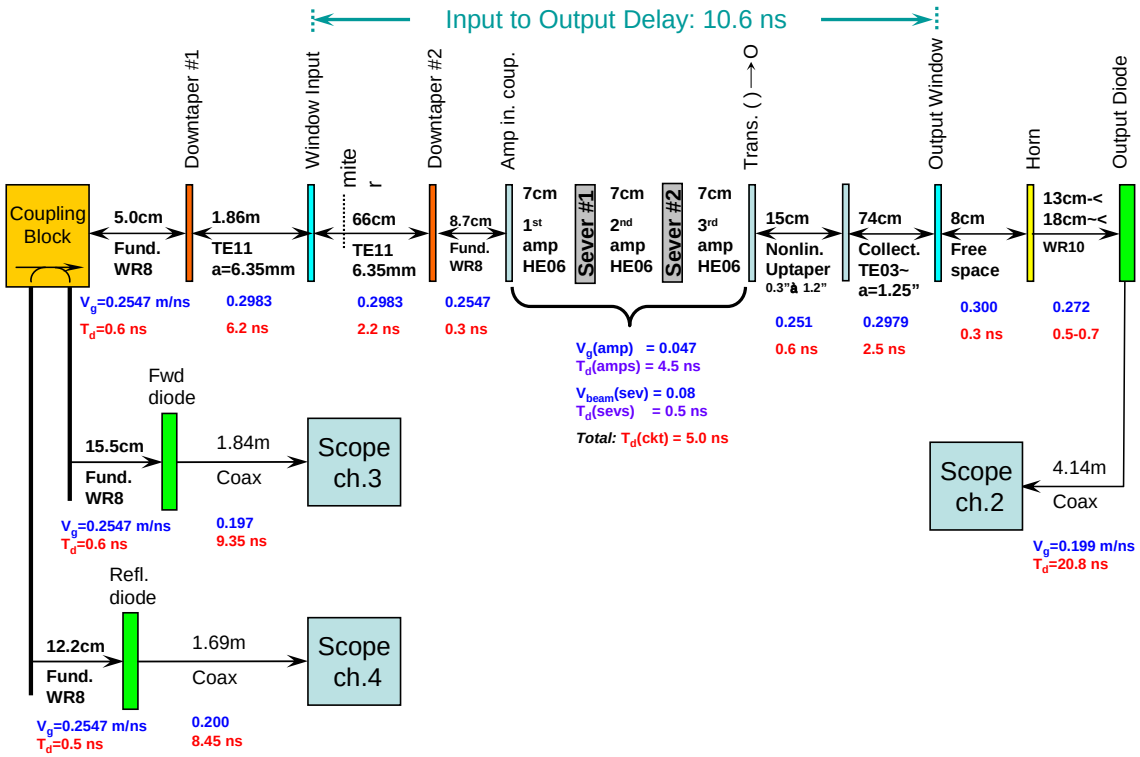

Figure 4-18: Diagram of estimated system group delays as an aid in mapping TDR measurements. Uncertainty is generally about 1 ns. The waveforms are measured by three video diodes: Forward, Reflected and Output.

based on group velocity for each subassembly of the whole experiment. Uncertainty is approximately 1 ns. The electrical length of the coaxial cables was measured to within a fraction of a nanosecond by setting the oscilloscope to trigger on the negative edge with a 50 Ω input impedance. Then the cable was charged by momentarily touching a T-joint attached to the oscilloscope with a 1.5 V battery. Upon release of the battery, the cable discharges in two steps, and the width of the 0.75 V step is the round trip delay.

Figure 4-19 shows measured signals from the forward, reflected and output diodes at 139.63 GHz for a 200 W output pulse. The reflected diode signal delay and input-to-output delays exactly match up to confirm that the echoes are coming from the overmoded input transmission line. The echoes are only seen at some frequencies. Short pulses in the range of 4 to 5 ns have been generated at power levels exceeding 400 W. Statistically, the amplifier did not show any pulse broadening due to

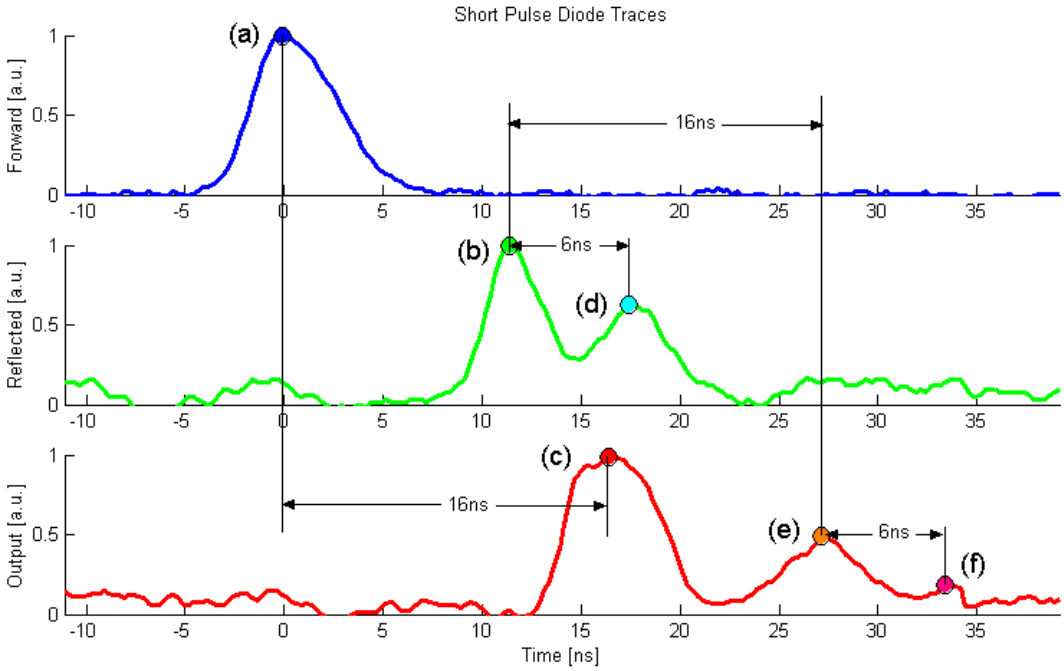

Figure 4-19: Measured TDR traces at 139.63 GHz. The input power is detected by the forward diode at (a). The first reflected signal (b) is from the input window, and a second reflection (d) is due to the internal downtaper. The output diode measures the main pulse (c) followed by two echoes (e) and (f) that are due to trapped power in the input transmission line.

bandwidth limitations, but subtle reflections at some frequencies appeared to slightly broaden the pulse by about 0.5 ns or so. An example of such a reflection-broadened event is visible on the rising edge of the output diode curve in Fig. 4-19(c) where a "shoulder" can be seen, and may be due to a slight chirp in the rise of the EIK pulse.

4.4.4 Backward Wave Oscillations

Fig. 4-20 shows the measured start current and oscillation frequency for the HE_{05} backward wave mode at around 117 GHz. The start current threshold was measured by decreasing the electron beam current at each magnetic field until the oscillation disappeared. The minimum start current is only around 300 mA, but it occurs at a detuned magnetic field of 4.7 T and does not oscillate at the higher magnetic field of around 5.05 T in the amplifier regime.

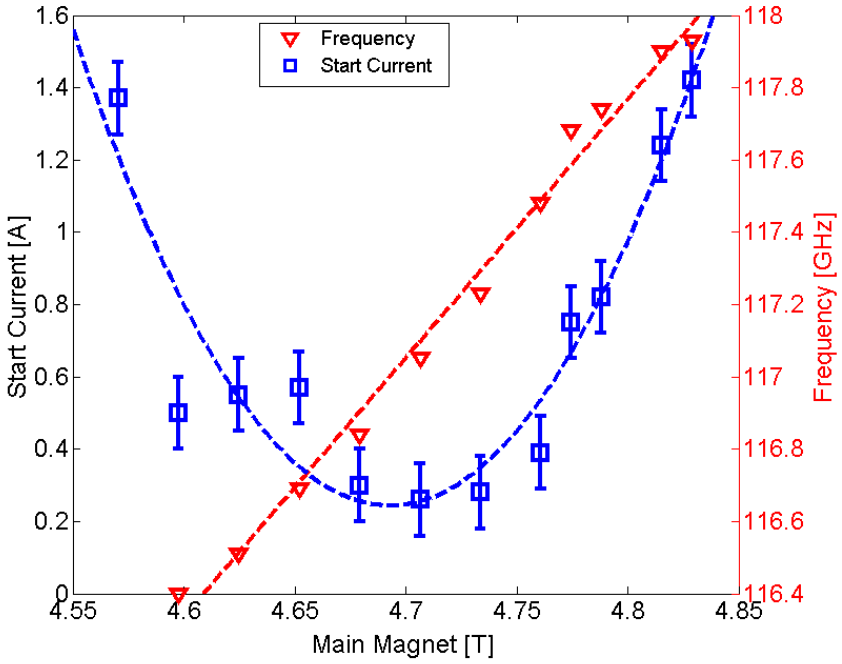

Figure 4-20: Start current threshold for the HE_{05} backward wave oscillations as a function of magnetic field.

4.5 Analysis of Data

The data illuminated several important factors that could be corrected in the next version of the tube. First, the measured BWO oscillation frequencies and EGUN simulations agreed that the α-value was somewhere between 0.5 to 0.6, which is significantly lower than the design value of 0.7 to 0.75. According to nonlinear simulations, a higher α value would be important for achieving higher gain and power.

Second, the measured bandwidth of 1.5 GHz maximum was in line with the bandwidth of the input coupler as estimated by the perturbation technique. HFSS predicts over 5 GHz bandwidth easily for a wider mirror aperture and confocal ($R_c = L_\perp$) system, and nonlinear simulations of the gyro-TWA predicted bandwidth on the order of 4 to 6 GHz. Therefore, it is concluded that the input coupler is limiting the bandwidth of the gyro-TWA.

Third, the combination of the downtaper and uptaper pair on the input transmission line caused numerous standing wave resonances that reduced input power sharply at a multitude of frequencies. In fact, an average 4 dB insertion loss was

measured on the input transmission line, mostly due to the downtaper. In addition, the coupling loss of the input power from the WR8 waveguide to the actual circuit is around 4-5 dB according to HFSS simulations of an ideal coupler, but in fitting the data, it seems the coupling loss is closer to 10 dB (the irregularities could not be modeled rigorously in HFSS). A three-mirror quasi-optical input transmission line based on Gaussian optics was designed in HFSS that allows the coupling loss to drop to below 2 dB.

Fourth, in fitting the data to theory, the velocity spreads appear to be higher than anticipated. Since this electron gun was designed to operate at 65 kV, the beam quality is not optimized for operation at 30 to 40 kV. A modern electron gun design should have perpendicular optical velocity spreads of 1% or less and total velocity spreads of under about 6%. This electron gun is predicted to have a minimum perpendicular optical velocity spread of about 3% and, according to how the simulations fit the experimental data, it seems to have a total of more like 9% spread, although it does depend on the operating parameters. In a very long circuit such as this one, having a low velocity spread is even more critical.

Finally, it was found that reflections from the output window at frequencies in the range of 125-130 GHz led to oscillations that prevented the amplifier from reaching higher regions of gain. The double-disc window helped very much in this regard, but slightly restricts the bandwidth of the window, according to electromagnetic theory.

4.6 The Spectrometer System

The actual spectrometer system will ultimately require a precision MMW pulse generation system and a highly stable, low ripple power supply. Both of these items are discussed below.

4.6.1 The RF Source

The low-power RF source must be able to supply at least 100 mW with a bandwidth of greater than 1 GHz at a center frequency of 140 GHz. The source should

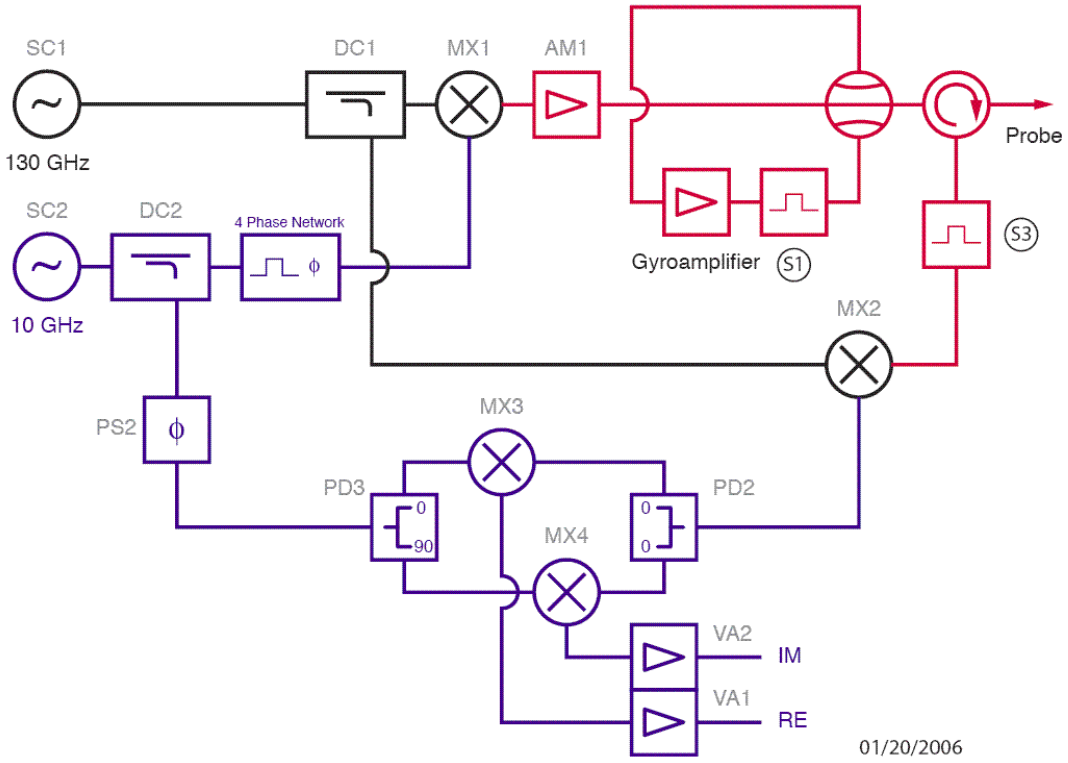

Figure 4-21: Phase stable, frequency multiplying diode transceiver system employing a 4-phase pulse-forming network. *(Courtesy of T. Maly, MIT Francis Bitter Magnet Laboratory.)*

also be capable of generating short pulses and must be very phase stable. Possible systems include a highly phase stable, frequency multiplying diode and a 4-phase pulse-forming network. These components, along with the system shown in Fig. 4-21 essentially comprise a high-performance radar system. In this system, pulses are generated by mixing a phase-controlled signal at 10 GHz with a 130 GHz source to generate 140 GHz stable short pulses down to 1 ns. These short pulses are amplified by the gyro-TWA described in this thesis, and the resulting high-power short pulses are sent to the spectrometer probe. The echo is received along the bottom channel by a down-mixing and phase detection network.

To protect the sensitive receiver from the high power gyro-amplifier, the timing sequence in Fig. 4-22 is proposed using several high-speed MMW switches. In this diagram, the blanking gate $S1$ prevents power coming out of the gyro-TWA from traveling to the spectrometer, but opens for enough time to send a high-power MMW

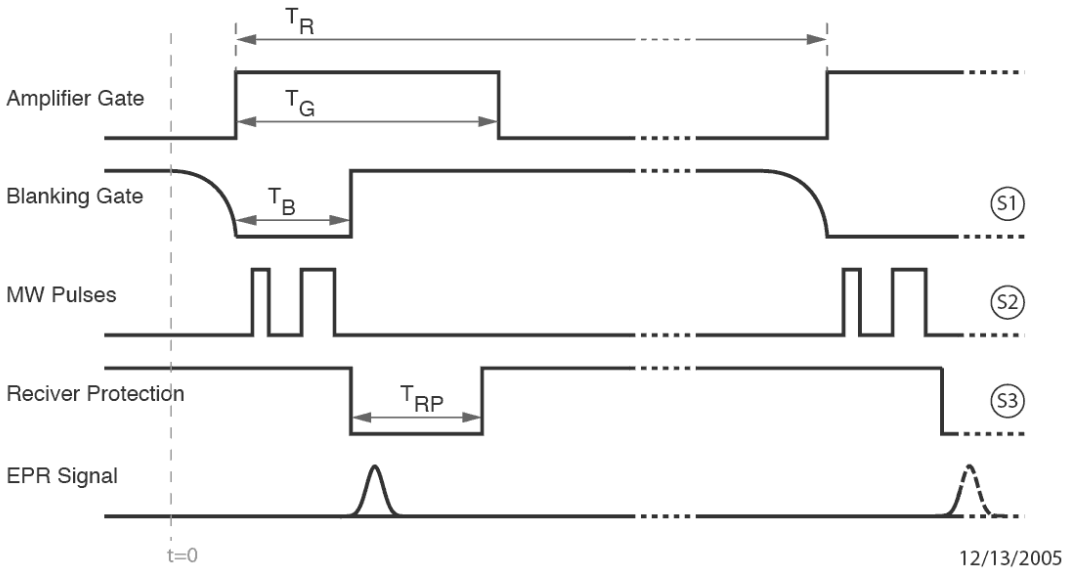

Figure 4-22: A proposed timing diagram for the transceiver system. *(Courtesy of T. Maly, MIT Francis Bitter Magnet Laboratory.)*

pulse sequence into the probe. The receiver protection switch $S3$ blocks power from the sensitive receiver while the high-power pulses are being generated. This protection switch opens to receive the echo from the spectrometer. Several electrically-controlled prototype silicon switches have been tested to date, but even the fastest rise times are too slow at 4-8 ns. The final switches must be faster than 1 ns and, in particular, $S1$ must be able to handle high pulsed power in an overmoded waveguide system.

4.6.2 New Power Supply

To maintain zero-drive stability at high gain, it is very important to have a power supply with low voltage ripple and high stability of the voltage level. Since the gain of the amplifier is usually limited by the presence of oscillations, it is important to be able to set the voltage close to the oscillation threshold without crossing that threshold. In addition to the low ripple requirement, the droop of the pulse must be very low in order to maintain the phase stability requirements for electron spin resonance experiments. It is estimated that the voltage ripple and droop must be below $\pm 0.1\%$ to meet the strictest requirements.

Due to ripple on the present power supply, it was difficult to reach high gain because oscillations often appeared on the voltage ripples. These voltage ripples seem to be due to L/C resonances because they did not change shot-to-shot. The present power supply was a built at MIT a very long time ago and was not designed for ultra-high stability and regulation, but it was sufficient to prove this gyro-TWA experiment.

4.7 Conclusions

The gyro-amplifier experiment using this amplifier interaction circuit succeeded in producing over 820 W peak power, a linear gain of 34 dB, and a saturated bandwidth of over 1.5 GHz. Furthermore, short pulses down to 4 ns at several hundred watts and over 20 dB gain have been produced with no noticeable pulse broadening. The short pulse tests revealed that trapped power in the input waveguide system causes echoes. This same transmission line is responsible for causing resonant fluctuations in the power available to the amplifier circuit. Table 4.2 compares the required specifications to the achieved values.

During the experiment, the best operating points gravitated toward higher voltages, ending up at 38 kV. These trends seems to agree well with EGUN simulations showing a reduction in perpendicular velocity spread as well as an increase in α at higher voltages. This result is not entirely unexpected, since the electron gun was originally designed to operate at 65 kV. Through EGUN simulations and experimentally measured backward wave oscillation frequencies, it was determined that α is between 0.5-0.6 at the voltage of 38 kV. Simulations show that α must be increased toward 0.7 or more in order to reach higher gain and output power.

The input coupler was measured to have a bandwidth of only 1.5 GHz due to irregularities in the coupling aperture, limiting the overall bandwidth of the amplifier. The simulation of the input coupler predicts a bandwidth of over 5 GHz.

Armed with these observations, a new version of the experiment is designed for an operating point of 40 to 45 kV and $\alpha = 0.75$. Consequently, the confocal parameters

Table 4.2: Specifications and Achievements

Parameter	*Required*	*Achieved*
Maximum output power	>100 W peak	>820 W peak
Minimum pulse width	1 ns	below 4 ns*
Minimum Bandwidth	1 GHz	>1.5 GHz
Saturated gain	40 dB	34 dB

(The minimum pulse width capability of the source)*

must change to $R_c = L_\perp = 7.05$ mm to maintain synchronism properly. The input coupler has been redesigned for lower loss and is fabricated in a way that is less susceptible to errors.

Chapter 5

Mode Convertor Design

In this chapter, the design of the quasi-optical mode convertor will be discussed in detail. The purpose of the mode convertor is to carry the power out of the gyro-amplifier in an efficient way by transforming the operating mode into a Gaussian beam, which is preferred for transporting the beam long distances with low loss.

5.1 Mode convertor structure

Fig. 5-1 shows the general shape of the mode convertor along with dimension names used in the Ansoft HFSS [89] simulation. The electric field phase is shown at one specific point in time. The mode converter starts with an uptaper section to reduce the very high bounce angle to closer to 50 degrees. Then there is a series of dimples in the parallel plane to focus the fields into a beam. Finally, two mirrors move the beam off-axis, away from the electron beam, and guide it to a corrugated output waveguide.

Due to the transverse curvature R_c of the confocal waveguide, the fields are already Gaussian in the plane perpendicular ($\perp$) to the z-axis, reducing the design to a Gaussian optics problem. In the parallel plane ($||$), we use a dimpled launcher design [108, 109] to focus the fields into a Gaussian-like pattern and then correct the resulting beam with two mirrors. Because these two planes are independent and solved using different methods, they are treated separately here.

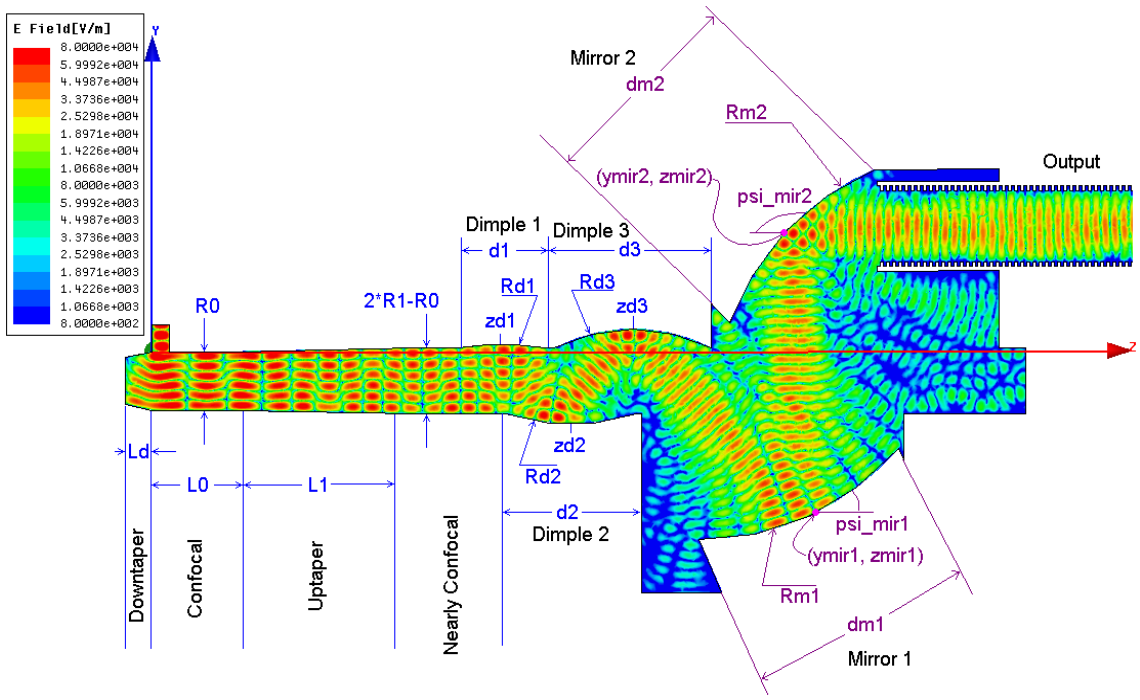

Figure 5-1: Dimensions and features in the parallel plane of a flat 2-D version of the mode convertor, shown with a logarithmic scale of the electric field.

5.2 Gaussian Optics

In chapter 2, the formalism for Gaussian beams was covered in detail. Here we extend that formalism to Gaussian optics by parameterizing the Gaussian beam by the complex q-parameter, defined as,

$$\frac{1}{q} \equiv \frac{1}{R} - \frac{j}{b} \tag{5.1}$$

This parameter allows us to keep track of the characteristics of the Gaussian beam as it passes through a series of mirrors.

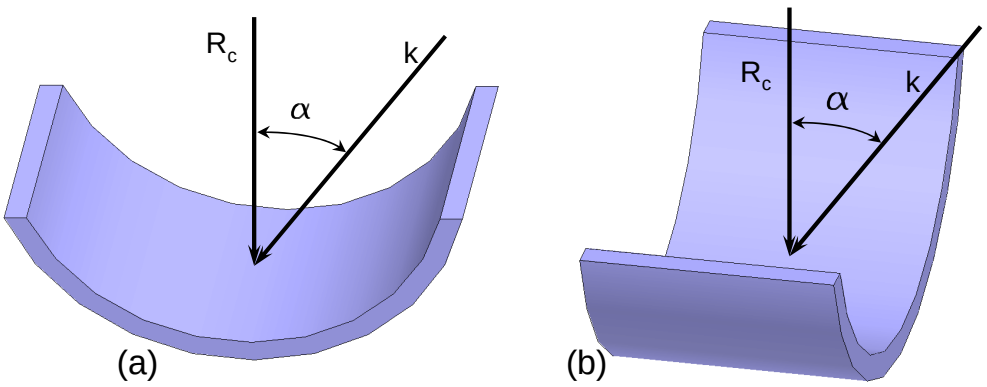

Figure 5-2: Incidence angle planes on a curved mirror: (a) The k-vector is in the same plane as the radius of curvature, (b) k is perpendicular to the R_c plane.

5.2.1 Propagation Matrices

It can be shown that the transformation law of the q parameter is equivalent to a bilinear transform on q of the following form [82],

$$q' = \frac{Aq + B}{Cq + D} \tag{5.2}$$

where q' is the new value after undergoing a transformation of the original value q. The values A, B, C and D can be put into a convenient matrix form and cascaded together using matrix multiplication.

For propagation through free space, the parameter q undergoes the following transformation:

$$\begin{bmatrix} A & B \\ C & D \end{bmatrix} = \begin{bmatrix} 1 & d \\ 0 & 1 \end{bmatrix} \tag{5.3}$$

where d is the distance of propagation. This results in the simple transformation $q' = q + d$.

For a curved mirror with radius R_c, the phase front of the beam incident at angle α in Fig. 5-2 is altered according to the following transformation,

$$\begin{bmatrix} A & B \\ C & D \end{bmatrix} = \begin{bmatrix} 1 & 0 \\ -\frac{2}{R} & 1 \end{bmatrix} \tag{5.4}$$

where $R = R_c \cos\alpha$ for the case when the incident k is parallel to (in the plane of) the radius of curvature R_c, and $R = R_c/\cos\alpha$ for the case when k is perpendicular to the radius of curvature. The focal length of the mirror is simply $f = R/2$.

At this point, we revisit the confocal derivation of Sec. 2.2.2 where we derived the membrane function and take a look at propagation with non-zero k_z. Fig. 5-3 is a diagram of the situation. Here we see that the path length L_b between the midplane and mirror is no longer equal to half the mirror spacing $L_\perp/2$, but is $L_b = L_\perp/2\cos\alpha$. The beam is incident on the curved mirror with an angle of α perpendicular to the curvature of radius, hence $R = R_c/\cos\alpha$. We want to show that the beam replicates itself after the bounce if the radius of curvature is chosen properly. The initial Gaussian beam waist is q and the final is q'. Since these are at the beam waist, the radius of curvature of the phase fronts are flat, $R = R' = \infty$, and hence the initial parameter is simply $1/q = -j/b$. To propagate a Gaussian beam through an inclined mirror and free space, we can cascade the series of matrices together to get q'. The $ABCD$-matrix system of Fig. 5-3 can then be written as follows,

$$\begin{aligned}
\begin{bmatrix} A & B \\ C & D \end{bmatrix} &= \begin{bmatrix} 1 & L_b \\ 0 & 1 \end{bmatrix} \begin{bmatrix} 1 & 0 \\ -\frac{1}{f} & 1 \end{bmatrix} \begin{bmatrix} 1 & L_b \\ 0 & 1 \end{bmatrix} \\
&= \begin{bmatrix} 1 - \frac{L_b}{f} & L_b\left(2 - \frac{L_b}{f}\right) \\ -\frac{1}{f} & 1 - \frac{L_b}{f} \end{bmatrix} = \begin{bmatrix} 0 & f \\ -\frac{1}{f} & 0 \end{bmatrix}
\end{aligned}$$

where we have used the fact that, for confocal waveguide,

$$\begin{aligned}
L_b &= \frac{L_\perp}{2\cos\alpha} = \frac{R_0}{2\cos\alpha} \\
f &= \frac{R_0}{2\cos\alpha} = L_b
\end{aligned}$$

and thus the q-parameter becomes,

$$q' = \frac{0 + f}{-q/f + 0} = -\frac{f^2}{q} \tag{5.5}$$

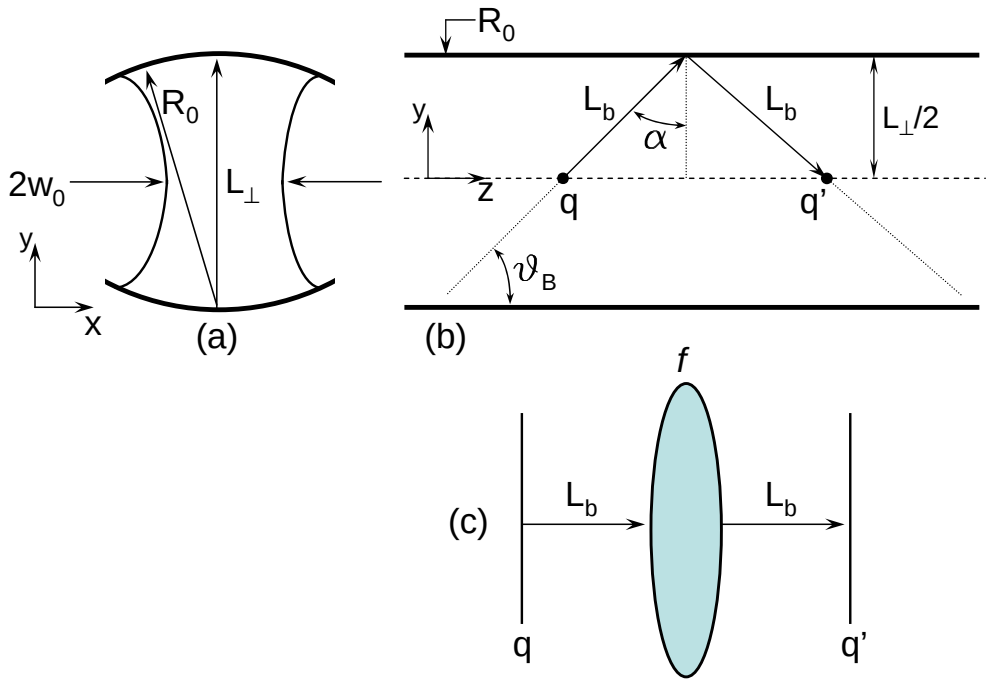

Figure 5-3: Gaussian beam propagation with finite k_z: (a) Gaussian beam waist w_0, (b) propagates in $\hat{z}$-direction. (c) Equivalent lens system from the midplane to one bounce and back to the midplane.

Setting $q' = q$ to replicate, we arrive at the condition $q^2 = -f^2$ implying $f = b = R_0/2$ will result in a Gaussian beam which replicates itself every time it crosses the midplane. This is the same result as analyzing only in the transverse plane with $k_z = 0$ because the $\cos\alpha$-terms along with $k = k_\perp/\cos\alpha$ and $L_b = L_\perp/\cos\alpha$ cancel out.

For the mode converter, this type of matrix system would be very complicated, but theoretically we could restrict the final q' given the initial q by ensuring that $R_{out,\perp} = R_{out,||} = \infty$, and $w_{out,\perp} = w_{out,||}$ at the output of the mode convertor to obtain a round Gaussian beam that matches with a corrugated output waveguide.

5.3 The Perpendicular Plane

The perpendicular plane is a solvable Gaussian optics problem. The only difficulty is the uptaper that is used to reduce the very high bounce angle in the confocal

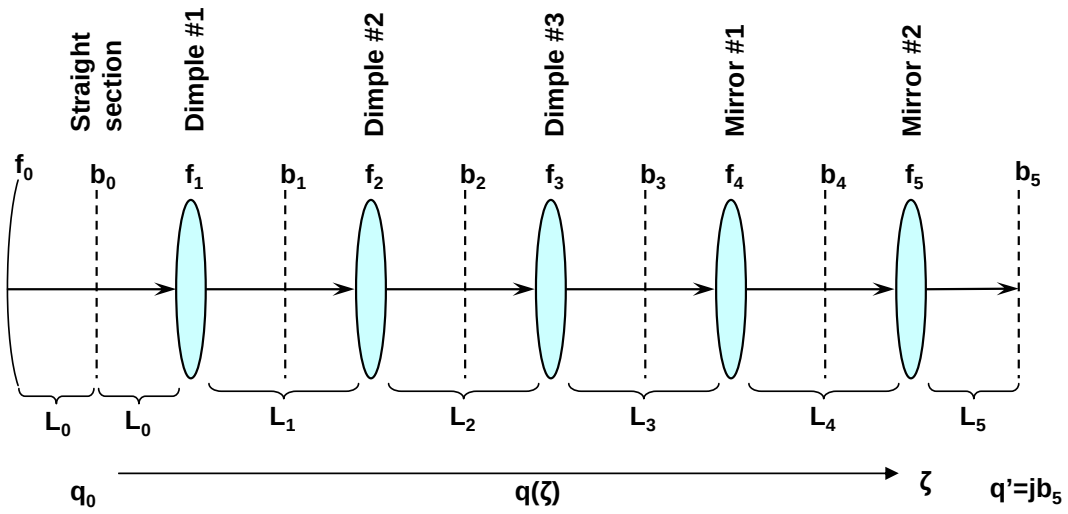

Figure 5-4: Equivalent mirror system of the perpendicular plane with focal lengths f_m, confocal parameters b_m, and lengths L_m. The coordinate along the path of the beam is ζ. The vertical dotted line indicates the location of the beam waist.

section because it would introduce some non-Gaussian mode conversion. As an approximation, assuming the weak angle of the uptaper does not introduce too much mode conversion, we can assume the fields are approximately Gaussian in the straight section of Fig. 5-4 and start from there. First, we need to know the bounce angle in between the mirrors. For that, we simply calculate the Brillioun angle,

$$\theta_B = \arcsin \frac{k_\perp}{k} \tag{5.6}$$

with $\alpha + \theta_B = \pi/2$ being the angle of incidence on the mirror (Fig. 5-3). From the chapter on curved mirror systems,

$$k_\perp = \frac{\pi}{L_\perp}\left(n + \frac{1}{\pi}\arcsin\sqrt{\frac{L_\perp}{2R_c}}\right) \tag{5.7}$$

We can reduce the perpendicular plane to a series of lenses and distances using Gaussian optics. Fig. 5-4 shows the equivalent system of mirrors from the second straight section which is nearly confocal, through the three dimples and two mirrors to the output, at which point the final beam should have infinite radius of curvature. We calculate the q-parameter in the nearly confocal region of L_0 by assuming the

q-parameter replicates itself in the midplane on every bounce,

$$q' = \frac{Aq + B}{Cq + D} = q \tag{5.8}$$

Solving this equation for q results in a quadratic equation,

$$q = \frac{A - D}{2C} \pm \frac{1}{C}\sqrt{\left(\frac{A + D}{2}\right)^2 - 1} \tag{5.9}$$

where $AD - BC = 1$ has been used because the determinant of the $ABCD$-matrix is unity for mirrors and for propagation in free space. The $ABCD$-matrix for the region of L_0 is,

$$\begin{bmatrix} A & B \\ C & D \end{bmatrix} = \begin{bmatrix} 1 & L_0 \\ 0 & 1 \end{bmatrix} \begin{bmatrix} 1 & 0 \\ -\frac{1}{f_0} & 1 \end{bmatrix} \begin{bmatrix} 1 & L_0 \\ 0 & 1 \end{bmatrix} = \begin{bmatrix} 1 - \frac{L_0}{f_0} & L_0\left(2 - \frac{L_0}{f_0}\right) \\ -\frac{1}{f_0} & 1 - \frac{L_0}{f_0} \end{bmatrix}$$

where $L_0 = L_\perp/(2\cos\alpha)$ and $f_0 = R_c/(2\cos\alpha)$, and R_c is the radius of curvature of the mirror surface. Note that $A = D$, so the equation for q reduces to,

$$q_0 = -\frac{\sqrt{A^2 - 1}}{C} = -j\frac{\sqrt{1 - A^2}}{C} = jL_0\sqrt{\frac{2f_0}{L_0} - 1} = jb_0 \tag{5.10}$$

Now that we have b_0 at the midplane, we can cascade all the matrices together for the mirror system to calculate $q' = jb_5$, the final beam waist,

$$\begin{bmatrix} A & B \\ C & D \end{bmatrix} = \begin{bmatrix} 1 & L_0 \\ 0 & 1 \end{bmatrix} \prod_{m=1,2,\ldots 5} \left\{ \begin{bmatrix} 1 & 0 \\ -\frac{1}{f_m} & 1 \end{bmatrix} \begin{bmatrix} 1 & L_m \\ 0 & 1 \end{bmatrix} \right\}$$

where the $\prod$ operator indicates cascaded matrix multiplication of the remaining matrices. For this system, the distances between the dimples are the same, hence $2L_0 = L_1 = L_2$. Using the values for radii of curvature in Table 5.1, the radius of curvature of the phase fronts and the beam waist have been calculated along the beam in the ζ direction in Fig. 5-5 using the known equations [110] for propagating

from an aperture of radius of curvature R_0,

$$w(z) = w_0 \left[\left(1 + \frac{z}{R_0} \right)^2 + \left(\frac{2z}{kw_0^2} \right)^2 \right]^{1/2} \tag{5.11}$$

$$R(z) = z \left[\frac{\left(1 + \frac{z}{R_0} \right)^2 + \left(\frac{2z}{kw_0^2} \right)^2}{\frac{z}{R_0} \left(1 + \frac{z}{R_0} \right) + \left(\frac{2z}{kw_0^2} \right)^2} \right] \tag{5.12}$$

where $z = 0$ is at the aperture. R_0 is a negative value obtained from the lens equation with a reversed sign,

$$\frac{1}{R_0} = -\left(\frac{1}{F} - \frac{1}{R_{inc}} \right) \tag{5.13}$$

where R_{inc} is the phase front radius of curvature before passing through the lens. The beam is first calculated in the nearly confocal section assuming the q-parameter replicates itself at the midplane as above. This value is propagated up to the first dimple, mirrored and propagated using Eqns 5.11 and 5.12 using the fact that the beam waist at the mirror surface must be continuous: $w(\zeta_0 - \epsilon) = w(\zeta_0 + \epsilon)$, where ζ_0 is the mirror location and ϵ is a very small number. Since the mirror is by definition altering the phase front radius of curvature, $R(\zeta)$ need not be continuous at the mirror surface.

For the parallel plane of Fig. 5-5, a rough approximation was made in order to use Gaussian optics. It was assumed that the fields were launched into the first dimple with a rectangular distribution. This rectangle was fit to a Gaussian in order to apply Gaussian optics. In practice, this approximation did not agree with HFSS simulations due to the presence of mode conversion from the uptaper and from the focusing effect of the dimples, so 2-D electromagnetic simulations were performed instead for the parallel plane.

5.4 The Parallel Plane

The fields in the parallel plane require focusing to be formed into the Gaussian beam. A series of circular dimples in the curved waveguide gradually focuses the beam into

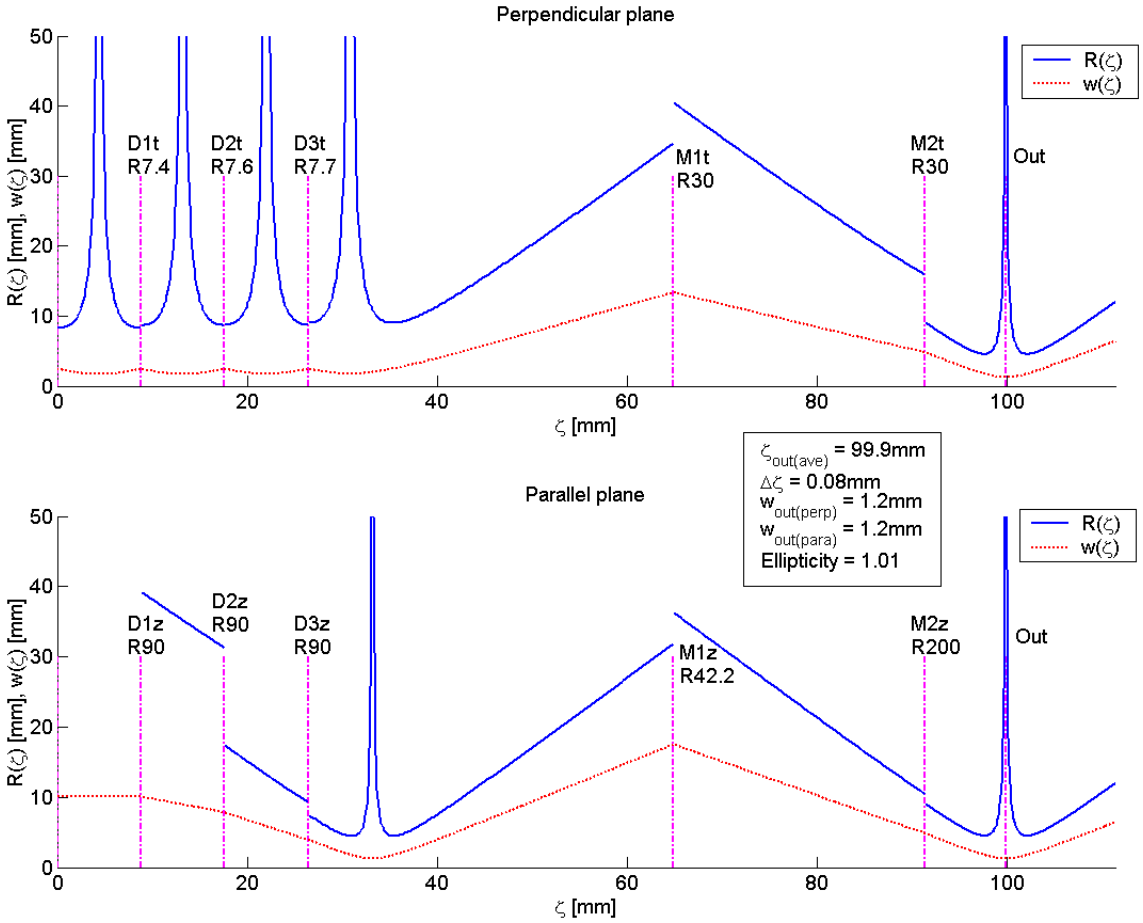

Figure 5-5: Traces of $R(\zeta)$ and $w(\zeta)$ along the beam trajectory for the perpendicular plane (above) and parallel plane (below). The vertical dash-dotted lines indicate the location of the dimples or mirrors along with their radii of curvature in each plane. For the parallel plane, a Gaussian fit to a rectangle of the launcher length was used. Labels starting with D refer to dimples, and M to mirrors.

Table 5.1: Design Parameters.

Region	input	uptaper	0	D1	D2	D3	M1	M2	Output
z	10	20	30	40	48	55	74	75	114
$R_{\perp}$	6.9	-	7.29	7.7	8.4	9.4	30	30	∞
$w_{0,\perp}$	1.6	-	1.7	1.8	1.8	1.9	3	12	2.5
$R_{\|\|}$	-	-	-	30	25	20	30	40	∞
$w_{0,\|\|}$	-	-	-	-	1.5	-	9	15	2.0

a pair of mirrors before the mode conversion is complete. This mode conversion problem is very difficult to solve using Gaussian optics due to the uptaper section and the fact that the fields are not Gaussian when they exit the uptaper.

In the parallel plane, the beam is essentially launched into the dimple by a cut in the nearly confocal waveguide. An attempt to was made to approximate the launched beam as a plane wave that is converted to a Gaussian beam after the first dimple, but the result did not agree with simulations in HFSS, due to the complex mode conversion interactions in the uptaper. It proved to be much faster and easier to use HFSS in 2-D for the initial design. Fig. 5-1, shown at the beginning of this section, illustrates how the electric fields are transformed from from the HE_{06} at the far left, and then gradually focused into a fundamental Gaussian beam with a single variation across the phase front. Actually, the beam is already tightly focused after dimple #2, so dimple #3 is not necessary for the parallel plane.

5.4.1 Dimpled Launcher Design

Most of the dimple design was performed in HFSS in planar 2-D waveguide for the parallel plane, because of the much simplified mesh and quicker solution times. In planar waveguide, however, the transverse wavenumber $k_\perp$ goes as the number of variations, n, instead of as $n + 1/4$ in confocal. This can be understood mathematically by setting $R_c \to \infty$ in Eqn. 5.7. Thus the perpendicular dimension $L_\perp$ of the waveguide section was reduced by a factor of $n/(n + 1/4)$ with $n = 6$ for the HE_{06} mode. Each dimple was designed to focus the beam a little bit, and by adding the dimples in order, a tightly focused beam was created. Using the 2-D system, an accurate design can be generated very quickly.

Finally, the whole design of the mode converter is made into a 3-D HFSS simulation, remembering to adjust $L_\perp$ back to the proper value for finite R_c. The key dimensions are parameterized to facilitate further optimization. 3-D models easily take several hours to simulate even with 32 GB of RAM on an 8-core processor. To refine the simulation, it is useful to optimize one component at a time, starting from the first dimple, gradually adding downstream components back in until the whole

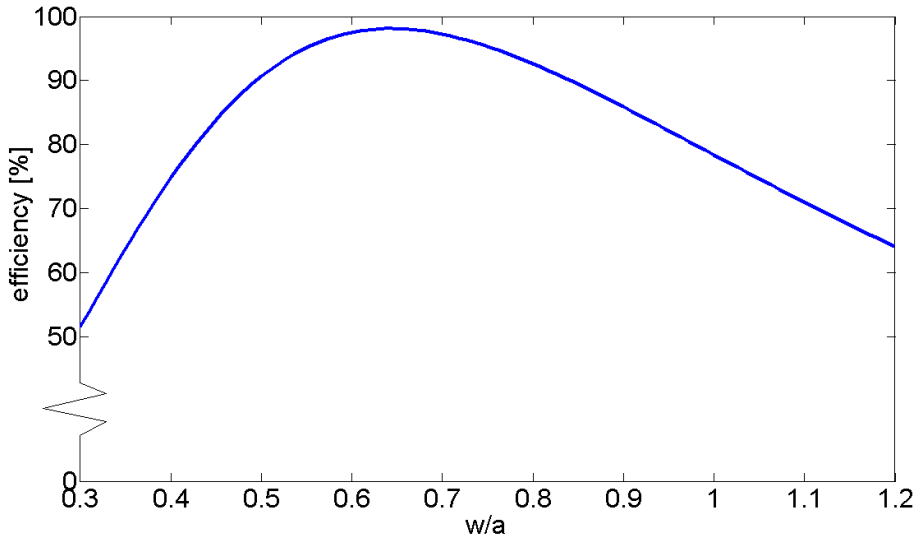

Figure 5-6: The matching efficiency between a free-space Gaussian beam and a fundamental HE_{11} hybrid mode in a corrugated waveguide is plotted against the ratio of the beam waist w and the waveguide radius a. The optimal efficiency is 98.1% for $w = 0.645a$.

converter has been refined. It is very difficult to calculate parameters such as the beam radius of curvature and beam waist from HFSS field solutions at a plane, and even more difficult to plot $R(\zeta)$ and $w(\zeta)$. It was helpful, however, to look at the phase of the electric field at key planes to locate the beam waist and then fit the simulation to extract an approximate beam waist value. The variation in the phase at the output plane should be zero, and the waist should be circular. In addition, the output beam waist of the free-space Gaussian beam should match to the radius of the corrugated waveguide supporting the fundamental HE_{11} hybrid mode. The matching efficiency can be calculated by the following expression,

$$\eta = \frac{|\int_0^a J_0\left(\frac{\xi_{11}}{a}r\right) \cdot \exp\left(-\frac{r^2}{w^2}\right) 2\pi r dr|^2}{\int_0^a J_0^2\left(\frac{\xi_{11}}{a}r\right) 2\pi r dr \cdot \int_0^\infty \exp\left(-\frac{2r^2}{w^2}\right) 2\pi r dr}, \tag{5.14}$$

where $\xi_{11} \approx 2.405$ is the first root of $J_0(\xi_{1n}) = 0$ because $J_0(\xi) = J_1'(\xi) + J_1(\xi)/\xi$. Fig. 5-6 shows a plot of $\eta(w/a)$. The maximum theoretical efficiency is approximately 98.1% and occurs when $w = 0.645a$. For a 12.7 mm (0.5") diameter corrugated output waveguide, this corresponds to a needed Gaussian beam waist of 4.1 mm.

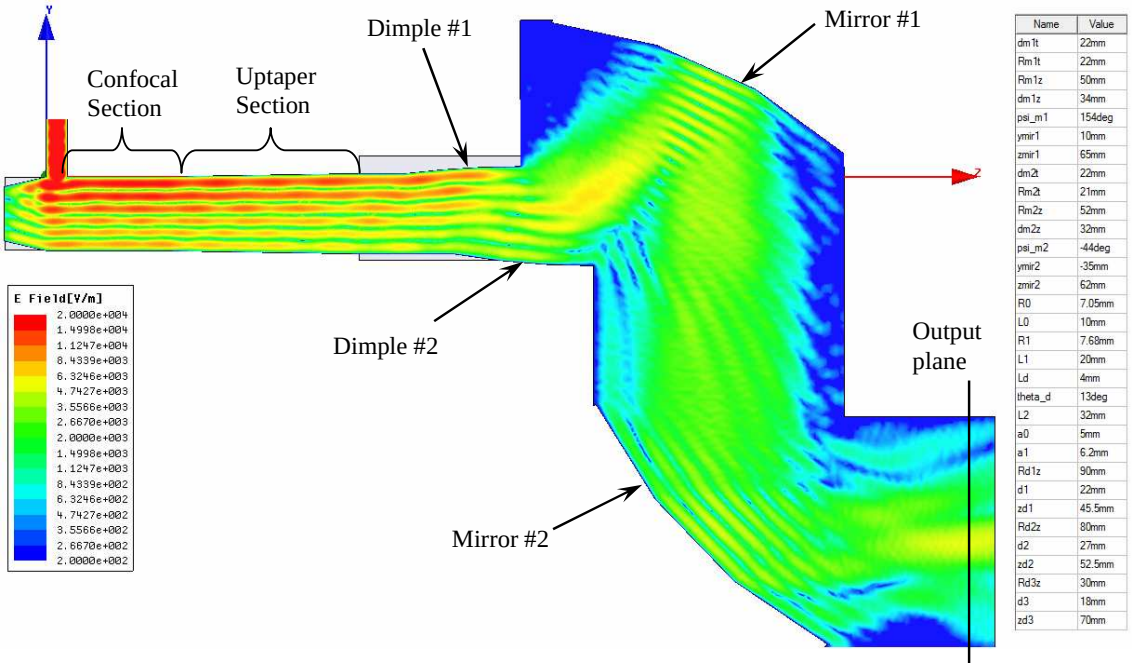

Figure 5-7: HFSS 3-D simulation of the final mode converter design with two dimples and two mirrors. The complex magnitude of the electric field pattern is shown to eliminate time dependence. This design achieved a simulated insertion loss of under 2 dB.

5.5 Results of Simulation

After refining many parameters of the mode converter simulations, a reasonable design was finished using only two dimples and two mirrors. Fig. 5-7 shows the complex magnitude of the electric field patterns in the midplane of the mode converter. Small amounts of stray radiation leak out of the structure and account for the insertion loss of under 2 dB. A portion of this insertion loss is due to diffraction from the fictitious input coupler needed to excite the HE_{06} confocal mode.

The simulated free-space Gaussian output beam for the mode converter is shown in Fig. 5-8. The beam does display some low-level formation of beamlets, but the strongest one is about 8 dB down in power. The phase is well controlled at the center of the waveguide and is flat to within $\pm 15^o$. The resulting beam waist is about 4.2 mm in both planes, which matches with the theoretical optimum of a 4.1 mm beam waist for a 12.7 mm diameter corrugated waveguide. The beam waist is the radius where

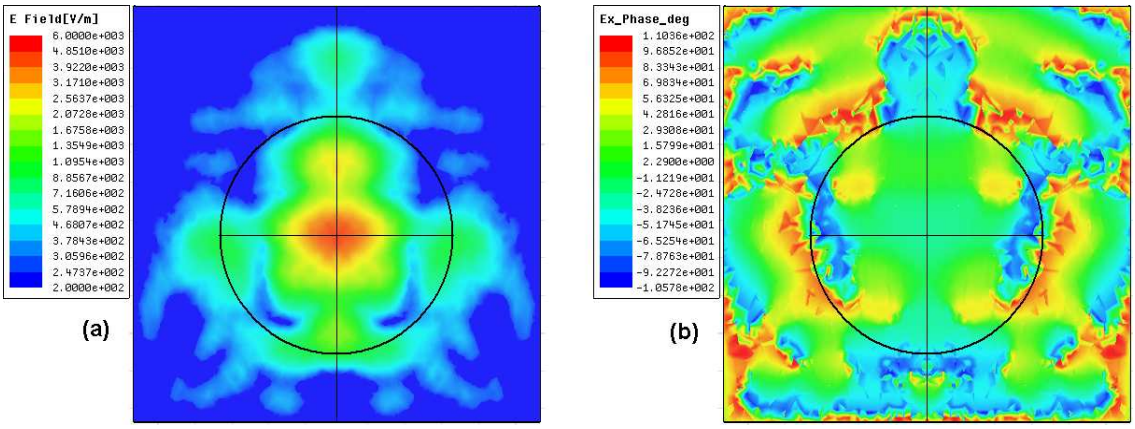

Figure 5-8: HFSS simulation of (a) the output electric field beam shape, and (b) corresponding phase. The black circle represents the best location for the 12.7 mm diameter corrugated waveguide. The beam waist is about 4.2 mm in both planes. The phase variation is about $\pm 15^o$ over the central region of the beam.

the electric field falls to -8.69 dB of the peak value.

5.6 Discussion

In this chapter, I introduced the $ABCD$-matrix formalism and the q-parameter formalism for analyzing Gaussian beam systems. I described in detail how the mode converter was designed using the $ABCD$-matrices in the perpendicular plane, and using 2-D electromagnetic simulations for the more difficult parallel plane. The HFSS simulations showed under 2 dB insertion loss in the full 3-D simulation, and the resulting beam waist of 4.2 mm was very close to the theoretical optimum waist of 4.1 mm for a 12.7 mm diameter corrugated waveguide.

Chapter 6

Conclusions

This novel gyro-traveling wave amplifier experiment has successfully demonstrated a linear gain of 34 dB, output powers of over 820 W, and a saturated bandwidth of over 1.5 GHz. In addition, although the experiments were nominally carried out at a 2 μs pulse length, it has been shown to amplify pulses as short as 4 ns, the limit of the present source, with no noticeable pulse broadening. These nanosecond-scale pulses were used to diagnose the system by a novel time-domain reflectometry technique. This unique method provided valuable insights to the nature of echoes, resonances, and reflections in the system, which could be pinpointed inside of the vacuum tube without the need to ever open the vacuum vessel.

I presented a detailed analysis of the theory of the confocal waveguide in Chap. 2. The interaction theory of the electromagnetic waves and the electron beam were described in Chap 3, and included linear theory, an analysis of instabilities, and nonlinear simulations that directed the design of the amplifier circuit.

The gyro-TWA experiment was described in Chap. 4, including thorough information on each major piece of the system, contour maps of the predicted electron gun performance, and a full characterization of group delay for each electromagnetic section of the amplifier. The amplifier performance was measured in terms of output power, bandwidth, gain and short pulse capability, and the results matched well to simulations.

In Chap. 5, I presented a detailed study of the theory, methods and design of an

internal mode converter that would enable the gyro-TWA vacuum tube to radiate a pure mode suitable for ultra-low loss transmission via corrugated waveguide.

6.1 Recommendations

These recommendations are provided to offer my perspective on the key features I believe could most significantly enhance the performance of this gyro-TWA device. Some of these suggestions, such as the new electron gun, would take considerable time and money to deploy. On the other hand, the internal mode converter has already been designed, modeled in 3-D, and even reduced to shop drawings, and the power supply has received a bidder.

6.1.1 Internal Mode Converter

An internal mode converter has been designed in Chap. 5 and simulations indicate an insertion loss of under 2 dB, a phase front flatness within $\pm 15^o$ of the output free-space Gaussian beam, and a beam waist of 4.2 mm matching to the theoretical optimum for a 12.7 mm diameter corrugated waveguide.

6.1.2 New MIG design

Since this Varian VUW-8140 triode electron gun was designed for optimum performance at 65 kV, it would be very beneficial to design a build a new electron gun capable of less than 1% optical velocity spread, and making full use of modern techniques to reduce surface roughness, the dominant source of non-optical velocity spread. Simulations predict that if the total perpendicular velocity spread is below 5%, the gain could be as high as 55 dB.

6.1.3 Improved Input Coupler

A major issue with the current experimental setup is the overmoded input transmission line. Since the transmission line has downtapers at both ends, it easily traps

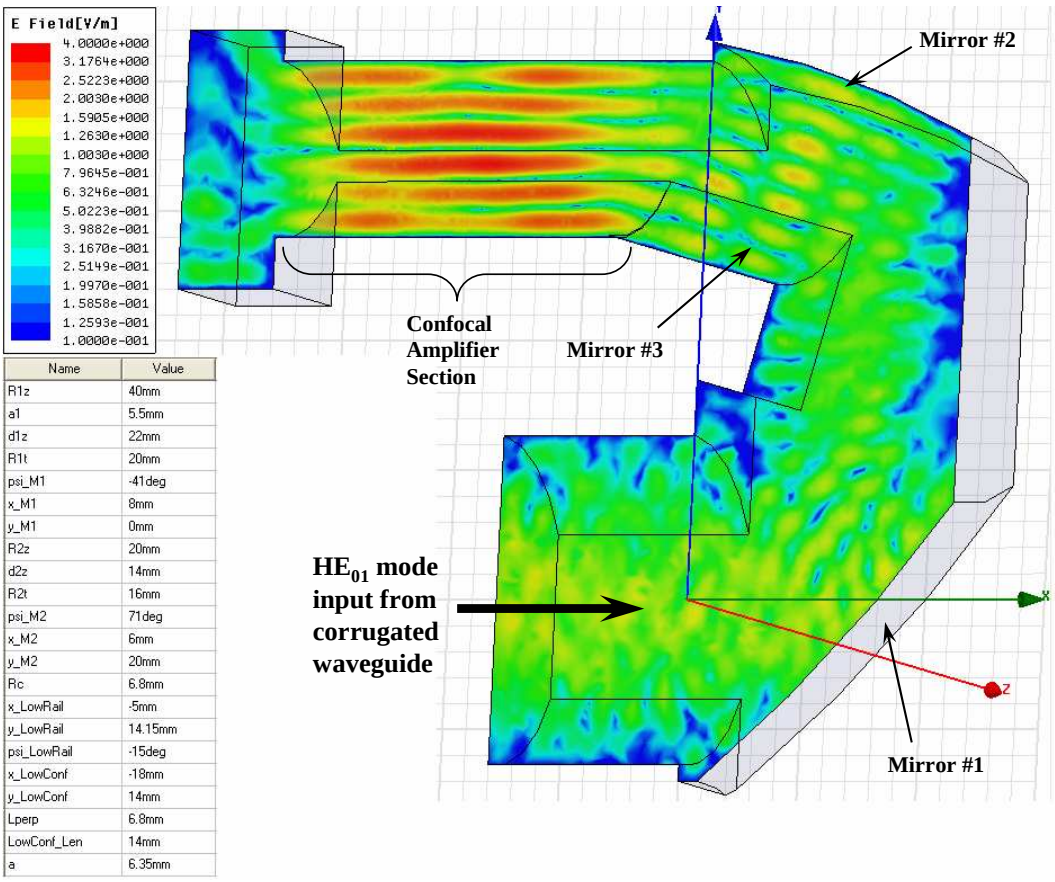

Figure 6-1: An HFSS simulation of a three-mirror quasi-optical input coupler to convert the HE_{11} mode to the confocal HE_{06} mode. Simulated insertion loss is under 2 dB.

power and causes resonances in the line. These resonances are clearly visible as the frequency is swept. In addition, the reflections from the downtapers cause echoes that were visible during nanosecond-scale pulse testing (Sec. 4.4.3). It also appears that, due to fabrication irregularities in the input coupler and first amplifier section, the coupling loss is significantly higher than predicted (Sec. 4.5). A quasi-optical input launcher could be implemented to drastically reduce insertion loss and eliminate trapped power resonances and echoes.

In Fig. 6-1, a quick three-mirror launcher system was simulated to couple the fundamental HE_{11} mode of a corrugated waveguide into a confocal waveguide supporting the HE_{06} mode. The estimated insertion loss for this system was less than 2 dB, as compared to 4 dB predicted for the current input coupler using WR-8 waveguide.

Due to the relative insensitivity of Gaussian optics to frequency, the bandwidth of this coupler could easily exceed 5 GHz. Once the power is coupled into the corrugated waveguide using this quasi-optical technique, it diffracts out of the confocal waveguide to be lost and does not reflect back into the corrugated waveguide, solving the problem of resonances and trapped power.

6.1.4 Power Supply

To maintain zero-drive stability at high gain, it is very important to have a power supply with low voltage ripple and high stability of the voltage level. Since the gain of the amplifier is usually limited by the presence of oscillations, it is important to be able to set the voltage close to the oscillation threshold without crossing that threshold. In addition to the low ripple requirement, the droop of the pulse must be very low in order to maintain the phase stability requirements for electron spin resonance experiments. It is estimated that the voltage ripple and droop must be below $\pm 0.1\%$ to meet the strictest requirements.

Appendix A

Gaussian Beams in a Spherical Resonator

The solution to Eqn 2.20 can be found by the Fresnel Integral by convolution of the source amplitude distribution $u_0(x_0, y_0)$ with the Fresnel Kernel for 2-D source,

$$h(x, y, z) = \frac{j}{\lambda z} \exp\left(-jk\frac{x^2 + y^2}{2z}\right) \tag{A.1}$$

which is itself a solution to the Paraxial Wave Equation. Since the PWE is invariant to translation in the z-coordinate, another solution can be written $h(x, y, z - z_0)$. By analytic continuation, we arrive at an interesting solution with $z_0 = jb$. It is the fundamental Gaussian beam, $u_{00}(x, y, z)$,

$$u_{00}(x, y, z) = \frac{j}{\lambda(z + jb)} \exp\left[-jk\frac{x^2 + y^2}{2(z + jb)}\right]. \tag{A.2}$$

By multiplying the complex terms through by $(z - jb)/(z - jb)$, this solution can be rewritten to expose characteristics of the Gaussian beam,

$$u_{00}(x, y, z) = \sqrt{\frac{2}{\pi}}\frac{1}{w(z)} \exp[j\phi(z)] \exp\left[-\frac{x^2 + y^2}{w^2(z)}\right] \exp\left[-\frac{jk}{2R(z)}(x^2 + y^2)\right]. \tag{A.3}$$

In this solution, the constant and $1/w(z)$ terms in front constitute a normalization such that, for all z,

$$\int_{-\infty}^{\infty} dx \int_{-\infty}^{\infty} dy |u_{00}(x,y,z)|^2 = 1. \tag{A.4}$$

The first exponential term in Eqn A.3 is a phase shift term, the second exponential is the beam profile, and the last exponential term represents the radius of the phase fronts, where

$$w^2(z) = \frac{2b}{k}\left(1 + \frac{z^2}{b^2}\right) \tag{A.5}$$

$$\frac{1}{R(z)} = \frac{z}{z^2 + b^2} \tag{A.6}$$

$$\tan\phi(z) = \frac{z}{b} \tag{A.7}$$

These equations define a Gaussian beam traveling in the $+z$ direction with phase front radius of curvature $R(z)$, phase $\phi(z)$ and beam waist $w(z)$ at the point where the electric field has fallen to $1/e$ of its maximum amplitude. It should be noted that others, particularly in Russia (and previous MIT theses [84] [57]), have defined w_0 to be the point where the *intensity* falls to $1/e$ (and hence the electric field falls to $e^{-1/2}$). The two are related by $w^2_{0(E)} = 2w^2_{0(I)}$, where the E and I denote the electric field notation and intensity notation, respectively. Here, the more conventional electric field notation used by Boyd [79] [80], Haus [82] and others is used. The minimum beam waist is given by

$$w_0 = \sqrt{\frac{2b}{k}} \tag{A.8}$$

where $b = kw_0^2/2 = \pi w_0^2/\lambda$ is the confocal parameter and can be found by use of Eqn A.6 at the mirror surface. We can rewrite Eqns A.5-A.7 in more convenient

terms of the minimum beam waist w_0 (with $\lambda/\pi = 2/k$) as

$$w^2(z) = w_0^2\left[1+\left(\frac{2z}{kw_0^2}\right)^2\right] \tag{A.9}$$

$$\frac{1}{R(z)} = \frac{z}{z^2+(kw_0^2/2)^2} \tag{A.10}$$

$$\tan\phi(z) = \frac{2z}{kw_0^2} \tag{A.11}$$

The validity of the paraxial approximation as a Gaussian beam is conditional on

$$\frac{1}{bk} = \frac{\lambda^2}{2\pi^2 w_0^2} \ll 1. \tag{A.12}$$

Higher order modes in a confocal mirror system require the use of angular wavefunctions in prolate spherical coordinates, but for Gaussian beams, they can be approximated near the center of the mirror using Hermite polynomials $H_\eta(\xi)$. Using Haus's form [82],

$$u_{mn}(x,y,z) = \frac{C_{mn}}{\sqrt{1+\frac{z^2}{b^2}}}\psi_m\left(\frac{\sqrt{2}x}{w(z)}\right)\psi_n\left(\frac{\sqrt{2}y}{w(z)}\right)\exp\left[-\frac{jk}{2R(z)}(x^2+y^2)\right]e^{j(m+n+1)\phi(z)} \tag{A.13}$$

where $\psi(\xi) = H_m(\xi)\exp(-\xi^2/2)$ and $H_\eta(\xi)$ is a Hermite polynomial, the lowest orders of which are,

$$H_0(\xi) = 1, \quad H_1(\xi) = 2\xi, \quad H_2(\xi) = 4\xi^2 - 2. \tag{A.14}$$

and normalizing constant,

$$C_{mn} = \left(\frac{2}{w_0^2\pi\cdot 2^{m+n}m!n!}\right)^{1/2}. \tag{A.15}$$

To obtain standing wave peaks in even and odd numbers of q, the number of variations between the mirrors, we counter-propagate two Gaussian beams and superimpose them in or out of phase respectively, noting that $w(-y) = w(y)$, $R(-y) = -R(y)$

and $\phi(-y) = -\phi(y)$,

$$u_{00}(x,y,z)e^{-jkz} + u_{00}(x,y,-z)e^{+jkz} = \\ 2\sqrt{\frac{2}{\pi}}\frac{1}{w(z)}\exp\left[-\frac{x^2+y^2}{w^2(z)}\right]\cos\left[\phi(z) - kz - \frac{k(x^2+y^2)}{2R(z)}\right] \quad \text{(A.16)}$$

$$u_{00}(x,y,z)e^{-jkz} - u_{00}(x,y,-z)e^{+jkz} = \\ 2j\sqrt{\frac{2}{\pi}}\frac{1}{w(z)}\exp\left[-\frac{x^2+y^2}{w^2(z)}\right]\sin\left[\phi(z) - kz - \frac{k(x^2+y^2)}{2R(z)}\right]. \quad \text{(A.17)}$$

In order to create a resonant structure out of these two beams, we simply place curved mirrors at the nulls defined by,

$$\frac{k(x^2+y^2)}{2R(z)} = const. \quad \text{(A.18)}$$

Again, this analysis is for a spherical resonator supporting a 2-D Gaussian beam. We can now find these modes by setting the phase terms to $q\pi$, and solving for k,

$$k = \frac{\pi}{L_\perp}\left[q + \frac{1+m+n}{2}\left(1 - \frac{4}{\pi}\arctan\frac{R_s - L_\perp}{R_s + L_\perp}\right)\right] \quad \text{(A.19)}$$

which for a confocal system with spherical radius R_s equal to separation $L_\perp$ becomes,

$$k = \frac{\pi}{L_\perp}\left(q + \frac{1+m+n}{2}\right). \quad \text{(A.20)}$$

Appendix B

Derivation of bunching mechanism

This document is a follow-up to questions proceeding from the Research Qualifying Exam administered on 11/10/04. In this document, I attempt to (i) show that the azimuthal bunching mechanism does indeed dominate over axial bunching, (ii) show that no gain is possible in this regime unless relativity is included in the model and (iii) give a pictorial description of the energy transfer process.

B.1 Azimuthal vs. Axial Bunching

Both azimuthal bunching (Cyclotron Resonance Maser Instability) and axial bunching (Weibel Instability) are simultaneously present in such systems of gyrating electrons, except in the cases of zero external magnetic field or infinite wavelength. For a given operating regime, one instability dominates over the other: When the phase velocity is greater than the speed of light, azimuthal bunching dominates and vice versa.

Starting with a linearized, relativistic Vlasov equation for the electrons (ion dynamics and collisions are neglected) and assuming the distribution function commonly used for monochromatic electrons in cyclotron maser studies,

$$f_0 = \frac{1}{2\pi p_\perp}\delta(p_\perp - p_{\perp 0})\delta(p_z) \tag{B.1}$$

where $\delta(t)$ is the Dirac delta function, the following dispersion relation can be de-

rived [111] for the case of a relativistic electron beam,

$$\omega^2 - k_z^2 c^2 = \frac{\omega_p^2}{\gamma_0}\left[\frac{\omega}{\omega - \Omega_e/\gamma_0} - \frac{\beta_{\perp 0}^2(\omega^2 - k_z^2 c^2)}{2(\omega - \Omega_e/\gamma_0)^2}\right] \tag{B.2}$$

where $\omega_p = \sqrt{(4\pi n e^2/m)}$ is the plasma frequency and n is the particle density per unit volume, $\Omega_e = eB_0/m_e$ is the non-relativistic cyclotron frequency, $\beta_{\perp 0} = p_{\perp 0}/\gamma_0 mc$ and the relativistic mass factor is,

$$\gamma_0 = \left(1 - \frac{v_{\perp 0}^2 + v_{\parallel 0}^2}{c^2}\right)^{-1/2}$$

Similarly, in the non-relativistic limit, the dispersion relation in Eqn. B.2 reduces to,

$$\omega^2 - k_z^2 c^2 = \omega_p^2\left[\frac{\omega}{\omega - \Omega_e} + \frac{k_z^2 v_{\perp 0}^2}{2(\omega - \Omega_e)^2}\right] \tag{B.3}$$

with $v_{\perp 0} = \beta_{\perp 0} c$.

Consider an electron spiraling around a magnetic field line and moving in the z-direction with velocity v_z in electromagnetic wave fields that vary as $\exp(-i\omega t + ik_z z)$. The Doppler-shifted cyclotron frequency can be defined,

$$\Omega_D = k_z v_z + \Omega_e/\gamma_0 \tag{B.4}$$

where Ω_D is the effective cyclotron frequency seen by the propagating wave.

For a small change in time Δt, the change in Ω_D is,

$$\Delta\Omega_D = k_z \Delta v_z + \Omega_e\left(\frac{1}{\gamma_0 + \Delta\gamma} - \frac{1}{\gamma_0}\right) \tag{B.5a}$$

$$\simeq k_z \Delta v_z - \Omega_e \Delta\gamma/\gamma_0^2 \tag{B.5b}$$

The first term on the right-hand side of the equation is due to axial bunching (Δv_z) and the second term is due to azimuthal bunching ($\Delta\gamma$).

Using the relativistic Lorentz equation of motion for the electrons, it can shown

that, for the axial instability we have,

$$\Delta v_z \mathbf{e_z} \simeq \frac{-e}{\gamma_0 mc} \mathbf{v}_\perp \times \mathbf{B_1} \Delta t \tag{B.6}$$

and for the azimuthal instability we have,

$$\Delta \gamma \simeq \frac{-e}{mc^2} \mathbf{v}_\perp \cdot \mathbf{E_1} \Delta t \tag{B.7}$$

and the change in Doppler shifted cyclotron frequency contains both mechanisms,

$$\Delta \Omega_D = \frac{-ek_z^2}{\gamma_0 m} \left(1 - \frac{\omega \Omega_e}{\gamma_0 k_z^2 c^2} \right) \mathbf{v}_\perp \cdot \mathbf{E_1} \Delta t \tag{B.8}$$

where $\mathbf{E_1}$ is the electric field of the propagating wave and $\mathbf{B_1}$ has been eliminated by Maxwell's equations.

If we consider two electrons orbiting on the same guiding center with the same initial momentum, but 180-degrees apart in Larmor space, we can see from Eqn. B.8 that since they have oppositely directed velocity components initially, $\Delta \Omega_D$ is of opposite sign for both electrons. If one electron gains in phase due to the electric field, the other slips in phase angle, and hence they tend to bunch toward each other. Also, since ω and Ω_e are of the same sign, the terms in parenthesis tend to offset one another. Furthermore, the azimuthal bunching mechanism dominates when

$$\frac{\omega \Omega_e}{\gamma_0 k_z^2 c^2} > 1 \tag{B.9}$$

and the axial mechanism dominates when

$$\frac{\omega \Omega_e}{\gamma_0 k_z^2 c^2} < 1 \tag{B.10}$$

In these two equations, γ_0 is only one of the factors determining which mechanism dominates. This shows that it is not only the electron energy that is the criterion for choosing the azimuthal bunching model or axial bunching model. The criterion is based on Eqns. B.9 and B.10. Furthermore, in the electron phase space, synchronism

condition is required to keep the bunched electrons in the energy extracting phase of the electric field. This condition can be expressed as $\omega \approx \Omega_e/\gamma_0$, hence, the above conditions reduce to,

$$\omega^2/k_z^2 > c^2 \tag{B.11}$$

in the *fast wave* region where azimuthal bunching dominates and

$$\omega^2/k_z^2 < c^2 \tag{B.12}$$

when the *slow wave* axial mechanism dominates.

In gyro-devices, such as gyrotrons and gyroklystrons, the cyclotron frequency is very close to waveguide cutoff, and hence we let $k_z \approx 0$. Going back to Eqns. B.2 and B.3, we can plug $k_z \approx 0$ and solve for ω. When can do this for the relativistic case (Eqn. B.2) by neglecting the first term on the RHS, since we've stipulated that $\omega - \Omega_e/\gamma_0 \simeq 0$ and thus the double pole in the second term dominates. We find a solution for ω as,

$$\omega \simeq \frac{\Omega_e}{\gamma_0} \pm i\frac{\beta_{\perp 0}\omega_p}{\sqrt{2\gamma_0}} \tag{B.13}$$

where the "+" term results in an instability that grows with time. Now if we let $k_z \approx 0$ in the non-relativistic dispersion relation in Eqn. B.3, we get, via the quadratic formula, a stable solution that has only real ω for all real Ω_e and ω_p. Thus a purely non-relativistic interaction ultimately cannot result in gain when $k_z \approx 0$, as it is for weakly relativistic gyro-devices.

Furthermore, we can see that axial bunching will be weak if a TE_{0p} mode is excited in the cavity. In this case we would have,

$$H_z = J_0(k_\perp r)e^{ik_z z} \tag{B.14a}$$

$$H_r = i\frac{k_z}{k_\perp}J_1(k_\perp r)e^{ik_z z} \tag{B.14b}$$

and since the only term that depends on $\mathbf{B} = \mu_0\mathbf{H}$ in the equation of motion contains the term $\mathbf{v}\times(B_0\mathbf{e_z} + \mathbf{B_1})$, then the axial bunching is due only to the $\mathbf{H_r}$ contribution,

which is zero in the limit $k_z \to 0$.

B.1.1 Bunching Summary

So far, we have shown that for a gyro-device where the phase velocity is greater than the speed of light, the azimuthal bunching mechanism dominates. We have also shown that the cyclotron resonance maser instability is absent in the non-relativistic model.

B.2 Energy Extraction Examples

Now we will look at explaining the transfer of energy from the electron beam to the RF fields via example. First we'll again prove that there is no possibility of net gain in the non-relativistic model for the case of azimuthal bunching and then give an example that shows net gain is possible in the relativistic model.

Let's start with the equation of motion (in MKS),

$$m\frac{d}{dt}\gamma\mathbf{v} = q\mathbf{E_1} + q\mathbf{v}\times(B_0\mathbf{e_z} + \mathbf{B_1}) \tag{B.15}$$

where B_0 is the constant axial magnetic field. Here, we will assume that $\mathbf{B_1}$ can be neglected since it only leads to the axial bunching, which we've shown is negligible. Let's first consider the case of the non-relativistic limit $\gamma \to 1$, and let $E_y = E_0 sin(\omega t)$ be linearly polarized in the y-direction. Then we have,

$$m\frac{d}{dt}v_x = qv_yB_0 \tag{B.16a}$$

$$m\frac{d}{dt}v_y = qE_y - qv_xB_0 \tag{B.16b}$$

$$m\frac{d}{dt}v_z = 0 \tag{B.16c}$$

With $E_y = 0$, the electrons simply spiral around the magnetic field lines. Now let $v_\perp \equiv v_x + iv_y$ be the complex velocity and the equations reduce to,

$$\left(\frac{d}{dt} + i\Omega\right)v_\perp = i\frac{qE_y}{m} \tag{B.17}$$

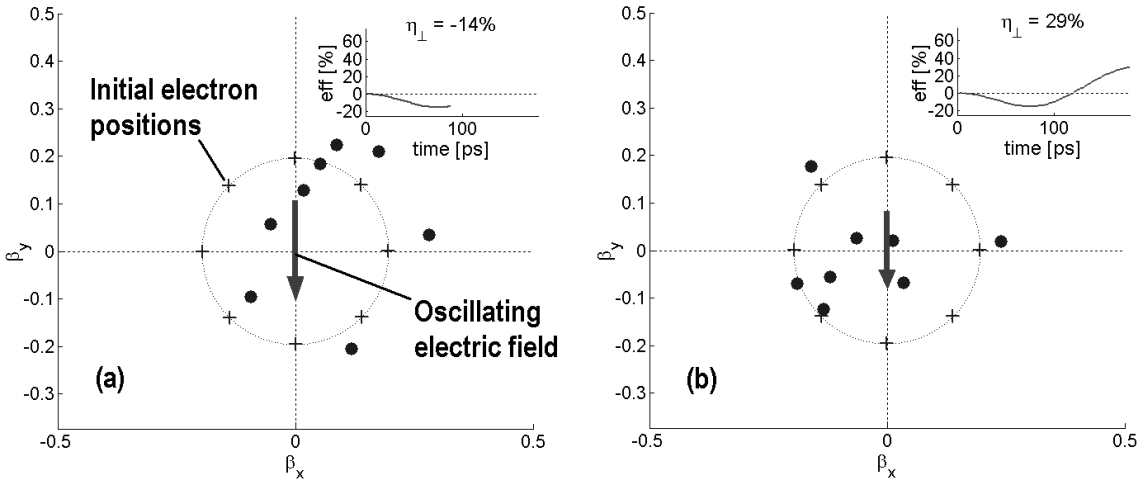

Figure B-1: Results of the electron motion code showing that gain (positive efficiency) is possible with relativistic effects included. (a) Showing loss after about 12 cyclotron orbits; (b) Showing gain after 25 orbits.

Table B.1: ODE solution values

Variable	Value	Note
γ_0	1.029	Relativistic factor
$\alpha_0 = \beta_{\perp 0}/\beta_{z0}$	1.5	Pitch factor
E_0	$5 \times 10^7\ V/m$	RF electric field strength
ω	$2\pi \times 143.5\ GHz$	RF frequency
Ω_e/γ_0	$2\pi \times 140\ GHz$	Cyclotron frequency
B_0	5.14 T	Static magnetic field

where $\Omega = qB_0/m$ is the signed non-relativistic cyclotron frequency. We can easily solve this differential equation and obtain,

$$v_\perp(t) = v_{\perp 0}e^{-i\Omega t} + \frac{qE_0/m}{\Omega^2 - \omega^2}(i\omega\cos\omega t + \Omega\sin\omega t - i\omega e^{-i\Omega t}) \tag{B.18}$$

The resulting particle energy $mv_\perp^2(t)$, however will be larger than or equal to its initial energy when averaged over the initial phase angles of the electrons. This implies that the electrons cannot give up more energy than they receive from the beam, and hence no net gain is possible. In fact, if $\Omega = \omega$, the electrons continually take energy from the beam and spiral with growing Larmor radii, as in a cyclotron particle accelerator.

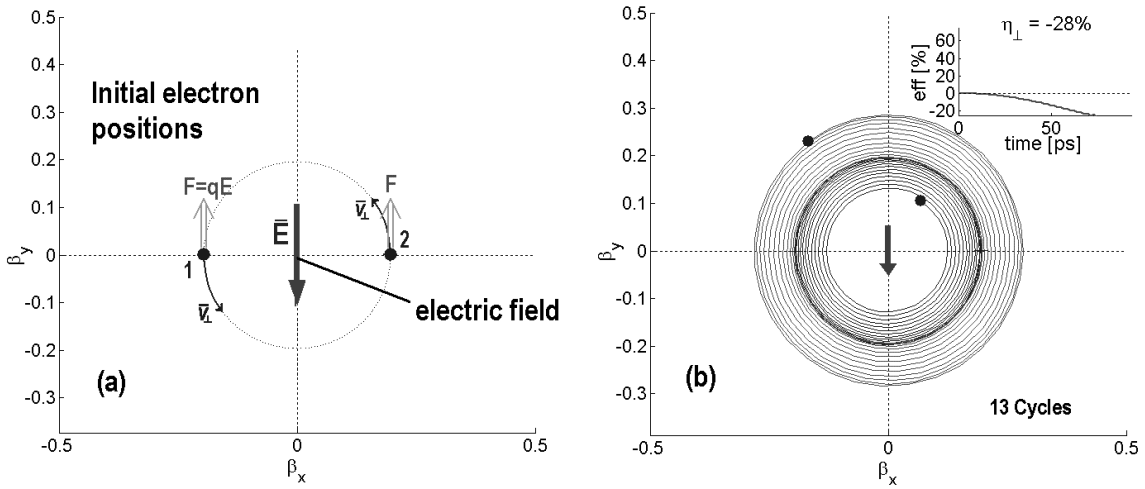

Figure B-2: (a) Initial electron phases. (b) Evolution after 13 cycles. Electron trajectories shown as continuous lines.

Including relativity in Eqn. B.15, we obtain a nonlinear relativistic correction term in the ODE that goes as $1/\gamma$,

$$\frac{d}{dt}v_\perp = \frac{1}{\gamma(t)}\frac{q}{m}\left[iE_y - iB_0 v_\perp - \frac{E_0 \sin\omega t}{c^2} Im(v_\perp)v_\perp\right] \tag{B.19}$$

where $\gamma(t) = [1 - \beta_\perp^2(t) - \beta_z^2]^{-1/2}$ is the relativistic evolution. This ODE can be solved numerically to show that, under certain conditions, gain can occur. A code was written to solve this equation and a result is shown in Fig. B-1. The parameters chosen are shown in Tab. B.1. The same code was then used to test the non-relativistic equation, and after trying many different parameters, only zero and negative gain were observed, as expected. The perpendicular efficiency is calculated in terms of the total particle energy and is defined to be,

$$\eta_\perp = 1 - \frac{\sum \beta_{\perp n}^2(t)\gamma_n(t)}{\sum \beta_{\perp 0m}^2\gamma_{0m}} \tag{B.20}$$

where n and m are the particle indices. It is a measure of how much beam energy has been converted to electromagnetic energy.

B.3 Picture of Energy Transfer

The simplest picture of the electron beam to E-field energy transfer is to view the electron bunch as a current source $\mathbf{J} = qN\mathbf{v}$ driving the curl of the RF magnetic fields in the cavity. The interaction is necessarily more complex than this because a uniform distribution of gyrating electrons produces only a static magnetic field; for a given electron, an electron of opposite phase can be found that cancels out the fluctuation. In order to achieve energy transfer, the electrons must first be bunched into an azimuthally asymmetric electron distribution so that this current density fluctuates with a frequency near that of the electric fields.

As the relativistic mass of the electrons changes, so does the electron cyclotron frequency, so frequency mismatch and phase evolution are key concepts here. In this non-self consistent model (following Eqn. B.19), we can consider these systems as having independent phases that must line up to produce gain.

Consider two electrons with equal initial perpendicular normalized velocity $\beta_{\perp 0}$ that start with opposite phase in the Larmor orbit (Fig. B-2a). An electric field is initially pointing in the $-\hat{y}$ direction and varies as $\cos\omega t$. Electron #1 feels the $\mathbf{F} = q\mathbf{E}$ force trying to slow it down. Meanwhile, electron #2 gains energy by the same force.

About 13 cycles of the electric field later, Fig. B-2b is produced showing that electron #1 has lost momentum (orbit is smaller than initially) and electron #2 has gained momentum (orbit is larger than initially). The equation for the cyclotron frequency is given by,

$$\omega_{cyc} = \Omega_e/\gamma = \frac{eB_0}{\gamma m_e} = \frac{v_\perp}{r_L} \tag{B.21}$$

where r_L is the Larmor radius. Electron #1 is effectively pushing against the E-field and loses energy, hence $\omega_{cyc} = v_\perp/r_L$ increases. Electron #1 has gained in phase, but lost momentum and electron #2 has fallen behind in phase, but gained momentum. At this point, the beginning of phase bunching can be seen, but the bunch is about 90° out of phase with respect to the E-field, so the instantaneous energy transfer of the system is zero. So far, we have only taken energy out of the E-fields, so the

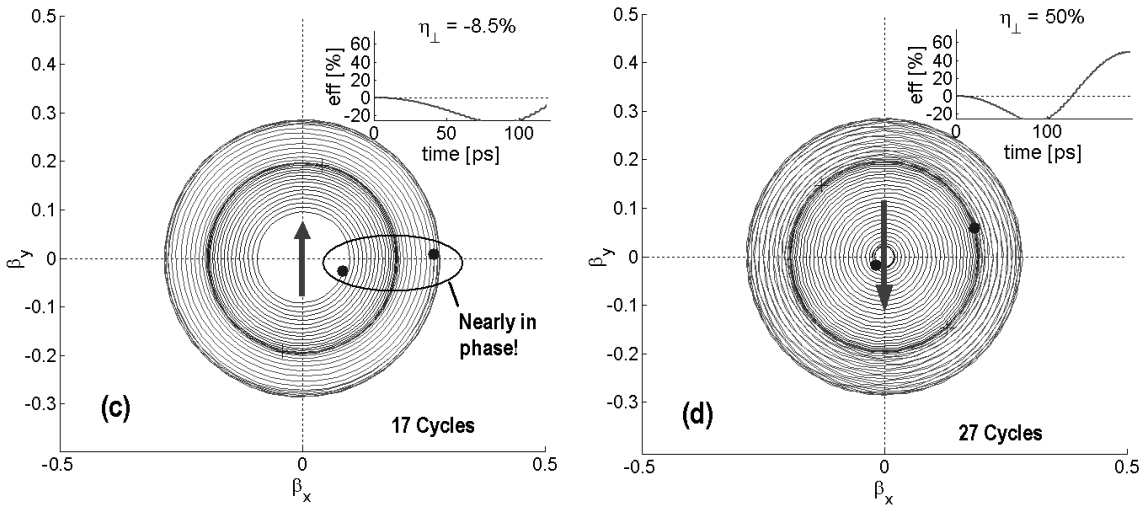

Figure B-3: (c) After 17 cycles, the electrons are in phase with each other and in the correct phase with the E-field to transfer their energy to the E-field. (d) After 27 cycles, 50% of the beam energy is transferred to the E-field.

efficiency is negative. It should be noted that this loss of energy from the E-field is required to form the azimuthal bunch if the electrons are initially unbunched, but the energy required is small in the linear regime. If one electron gains a small amount of energy Δv, and the other loses the same amount, then,

$$(v + \Delta v)^2 + (v - \Delta v)^2 = 2v^2 + 2(\Delta v)^2,$$

where the $(\Delta v)^2$ portion is taken from the electric field energy.

Just a few cycles later (Fig. B-3c), due to the electric field frequency being slightly higher than the cyclotron frequency, the phase of the E-field is now lined up with the evolving electron bunch such that the net force $\mathbf{F} = q\mathbf{E}$ now opposes both electrons, and hence energy is being transferred to the E-field. Finally, after 27 cycles, Fig. B-3d shows that 50% of the initial beam energy has been transferred to the E-field.

We can get a clearer picture of this phase evolution if we plot it against time. Fig. B-4a shows that the average of the electron phases cancel out the possibility of gain for $t < 20\,ps$ since they start out of phase in Larmor space. Due to the relativistic nature of this process, the electrons slowly slip in phase with respect to one another

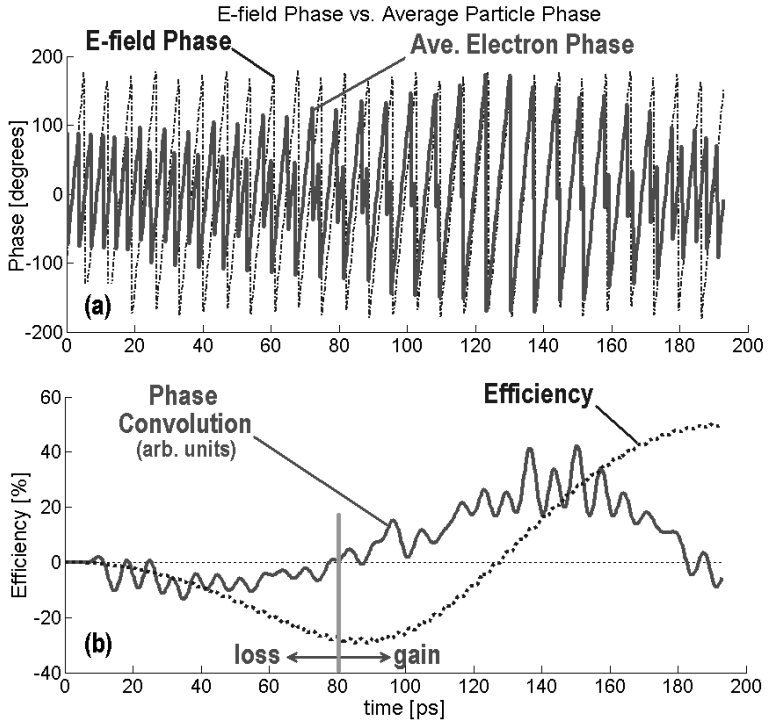

Figure B-4: (a) The average electron phase $(\theta_{e1} + \theta_{e2})/2$ and E-field phase evolution, (b) the efficiency and Phase Convolution,$\Upsilon(t)$.

and with respect to the electric field, and all three phases line up nicely around 130 ps. This point corresponds to the maximum growth of efficiency according to,

$$\frac{d}{dt}\varepsilon = q\mathbf{E}\cdot\mathbf{v} \tag{B.22}$$

where the particle energy ε is then decreasing.

In Fig. B-4b, I have plotted the efficiency and a "Phase Convolution" term that represents the correlation of the phases over a period T,

$$\Upsilon(t) = \left[\frac{\theta_{e1} + \theta_{e2}}{2}\arg\{E\}\right] \star Rect\left(\frac{t}{T}\right) \tag{B.23}$$

where θ_{e1} and θ_{e2} are the phases of the two particles, the $arg\{E\}$ is the phase angle of the E-field, "$\star$" denotes convolution, and $Rect(\xi)$ is the rectangle function, which is unitary for $|\xi| < 1/2$ and zero otherwise. I have also applied a smoothing low pass filter to this function in the plot. When this Phase Convolution term Υ is negative,

there is net loss in the interaction (energy is being transferred to the particles), and where it is positive, there is a net gain.

In Fig. B-4, both decay and growth of the efficiency are present, so this brings up the question whether it is possible to essentially shift the whole efficiency curve upward such that there is no point of negative efficiency. Indeed, this is possible. It can be done by evolving the electron phases up to the point of minimum efficiency (around -28% at $t = 90\ ps$ in this example) and by using the momentum and phase information of the electrons at that point as the initial conditions. This is the idea behind the gyroklystron - that the cavities preceding the final cavity bunch the beam over a wide range of frequencies such that no further bunching is needed in the final cavity. This way, energy transfer occurs in such a way that energy is only given to the E-fields.

B.4 Conclusions

In this document, I have shown that (i) the azimuthal bunching mechanism does indeed dominate over axial bunching, (ii) no gain is possible in this regime unless relativity is included in the model and (iii) alignment of electron and E-field phases is required for gain to occur. The E-field phase must catch the decelerating phase of the electron orbit for this gain to occur. A simple example was also studied that was modeled completely on the basis of the equations of motion. This example resulted in a positive electronic efficiency when relativity was included and no gain without relativity included.

Appendix C

Electron Gun Performance Maps

It was found during the experiment that the best performance was obtained at voltages closer to 40 kV, which seemed to be correlated to higher α-values and lower velocity spreads. A collection of simple MATLAB scripts were devised to automatically run the EGUN gun optics code hundreds of times to obtain maps of gun operation for fixed gun coil current. The simulations were performed using EGUN version EGN2w, a 32-bit Windows/DOS command-line executable program [101]. Due to the restriction of 50 point coils maximum for modeling the total magnetic field, the main magnetic field was modeled using 33 point coils and the gun coil was modeled using 17 point coils. It was found that using too few point coils for the gun coil, or using point coils that were too large in radius resulted in large inaccuracies in the total magnetic field profile. The velocity spreads at the amplifier entrance position were calculated over a range of axial tube position, cathode voltage, and mod-anode tap voltage at each fixed gun coil value. From these values, the optimal (lowest) velocity spread was selected for each mod-anode voltage, providing useful contour maps of gun performance and the parameters necessary to reach the optimal values. The maps are shown below in Figs. C-2 to C-6, corresponding to gun coil currents of -20 A, +0 A, +20 A, +40 A, and +60 A respectively.

These contour maps are plotted against cathode voltage and axial tube position. The axial tube position is set by the distance $ZGUN$, which is conveniently measured as shown in Fig. C-1.

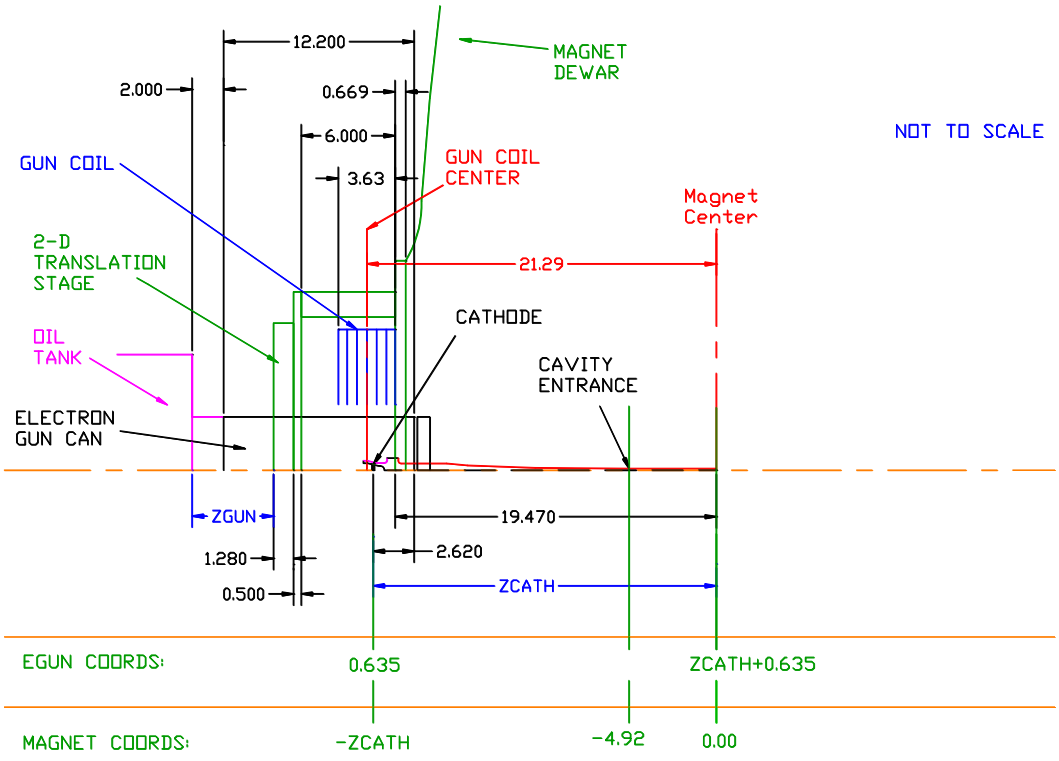

Figure C-1: The axial position of the tube is defined by the variable $ZGUN$, conveniently measured from the inner surfaces of the oil tank to the 2-D translation stage. Dimensions are in inches.

The objective of the electron gun contour maps is to easily locate the best operating regime for the electron gun. The key parameters are the α-value and the velocity spread. In addition, the optimal beam guiding radius, R_{guide} is about 1.9 mm for the HE_{06} mode in this waveguide, and should be kept below 2 mm to avoid hitting the beam scraper and alpha-probe. In general, these maps show that higher α-values are associated with higher cathode voltages and with smaller beam radii (higher magnetic field compression). For Figs. C-2 and C-3, the α-values are generally too low, and the beam guiding radius is larger than optimal. In Figs. C-4 and C-5 between 40-45 kV on the cathode, the α-values between 0.7 and 0.8 are readily attainable at low perpendicular and parallel velocity spreads. In addition, the beam radii, while slightly larger than optimal, are in the right range. In Fig. C-6, the α-values are starting to climb high enough that backward wave oscillations are likely at nominal current. Therefore, it is expected that the best performance will be obtained for a cathode voltage of 40 to 45 kV, a gun coil current of about 20 to 40 A and a tube axial position $ZGUN$ between about 138 and 142 mm.

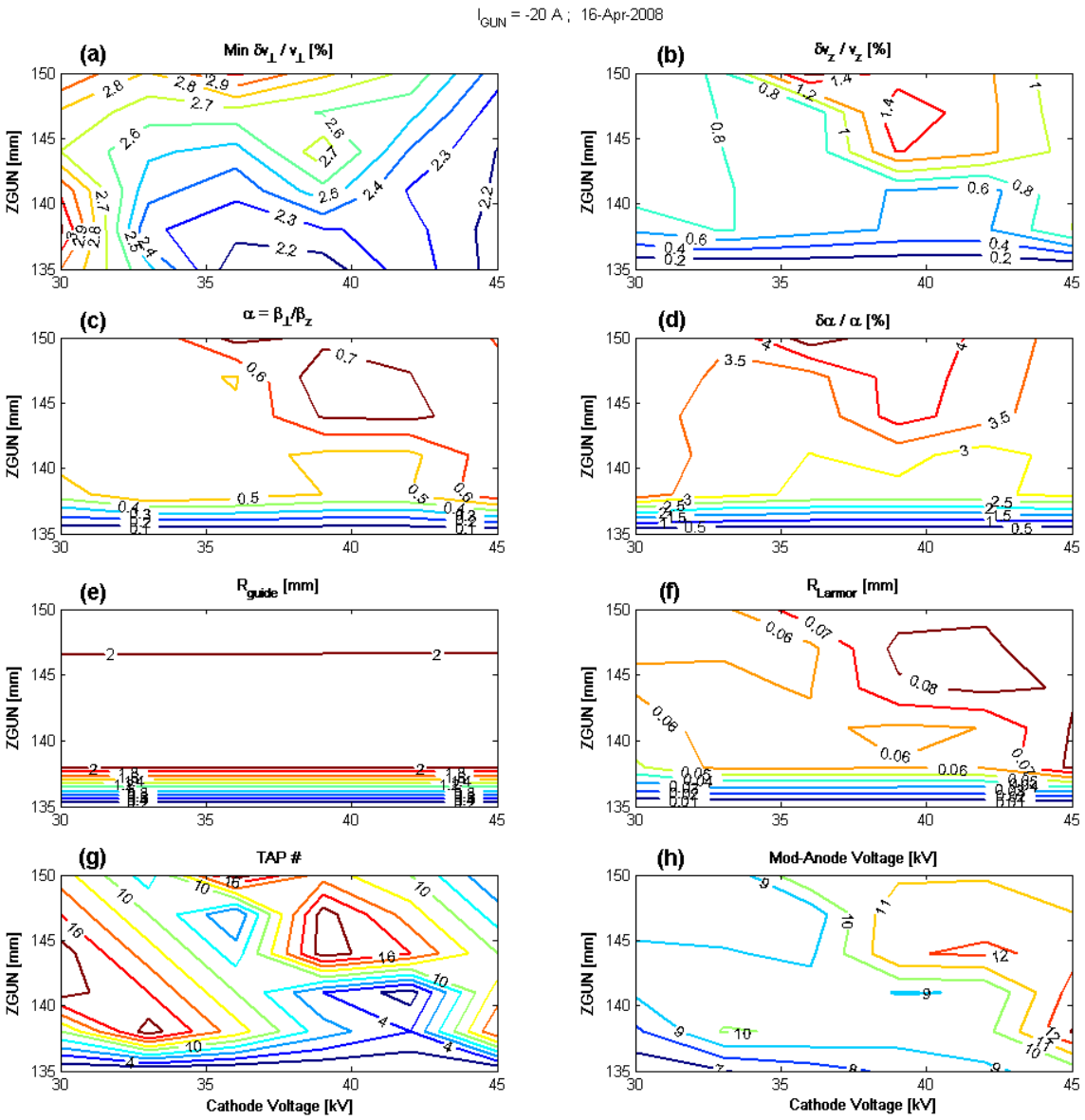

Figure C-2: Gun coil current = -20 A. Contour plots of (a) optimal perpendicular velocity spread, and (b) corresponding parallel velocity spread, (c) alpha value, (d) alpha spread (in percent), (e) guiding center radius, (f) average Larmor radius, (g) Mod-anode voltage Tap number, and (h) corresponding Mod-anode voltage.

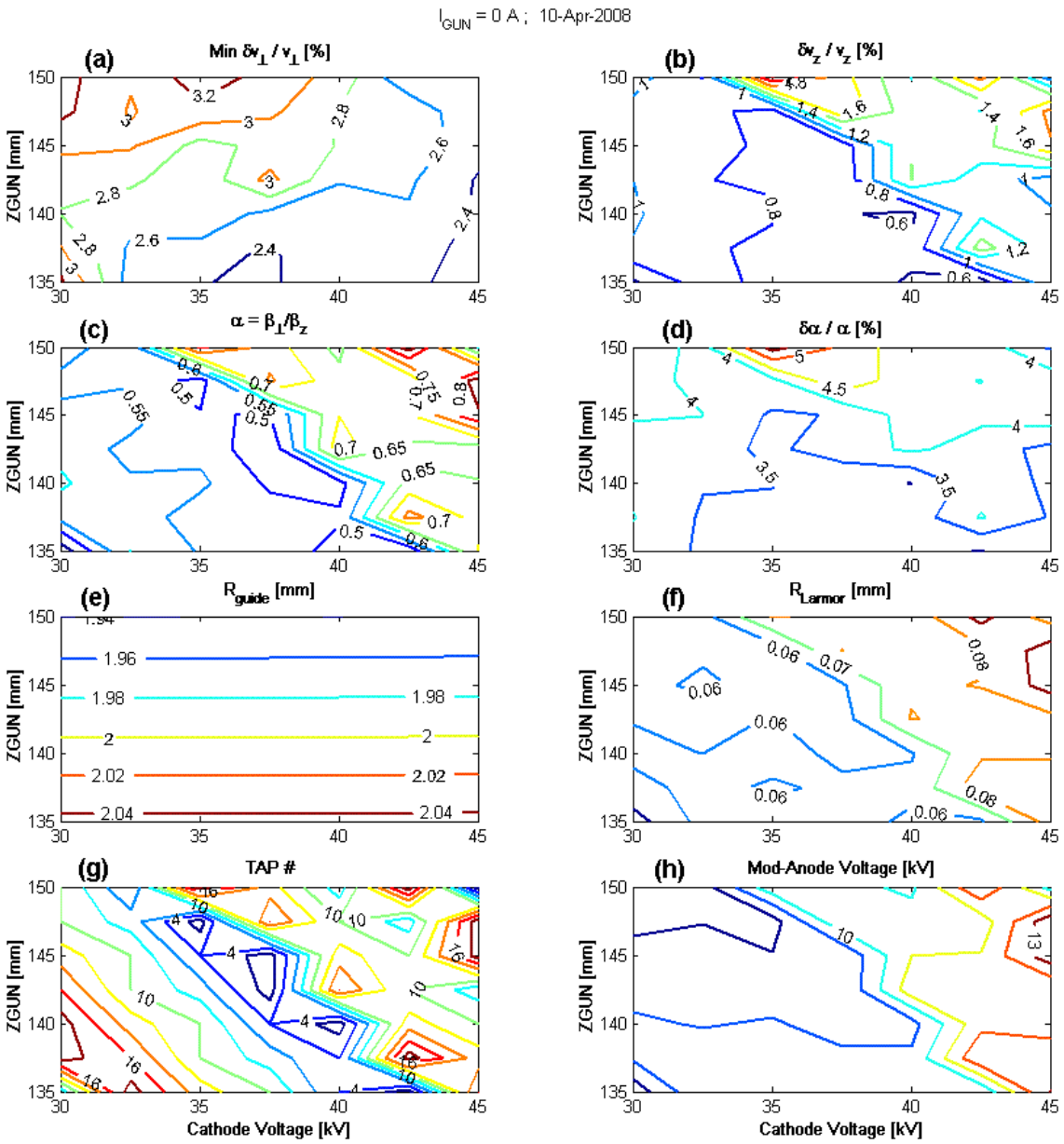

Figure C-3: Gun coil current = 0 A. Contour plots of (a) optimal perpendicular velocity spread, and (b) corresponding parallel velocity spread, (c) alpha value, (d) alpha spread (in percent), (e) guiding center radius, (f) average Larmor radius, (g) Mod-anode voltage Tap number, and (h) corresponding Mod-anode voltage.

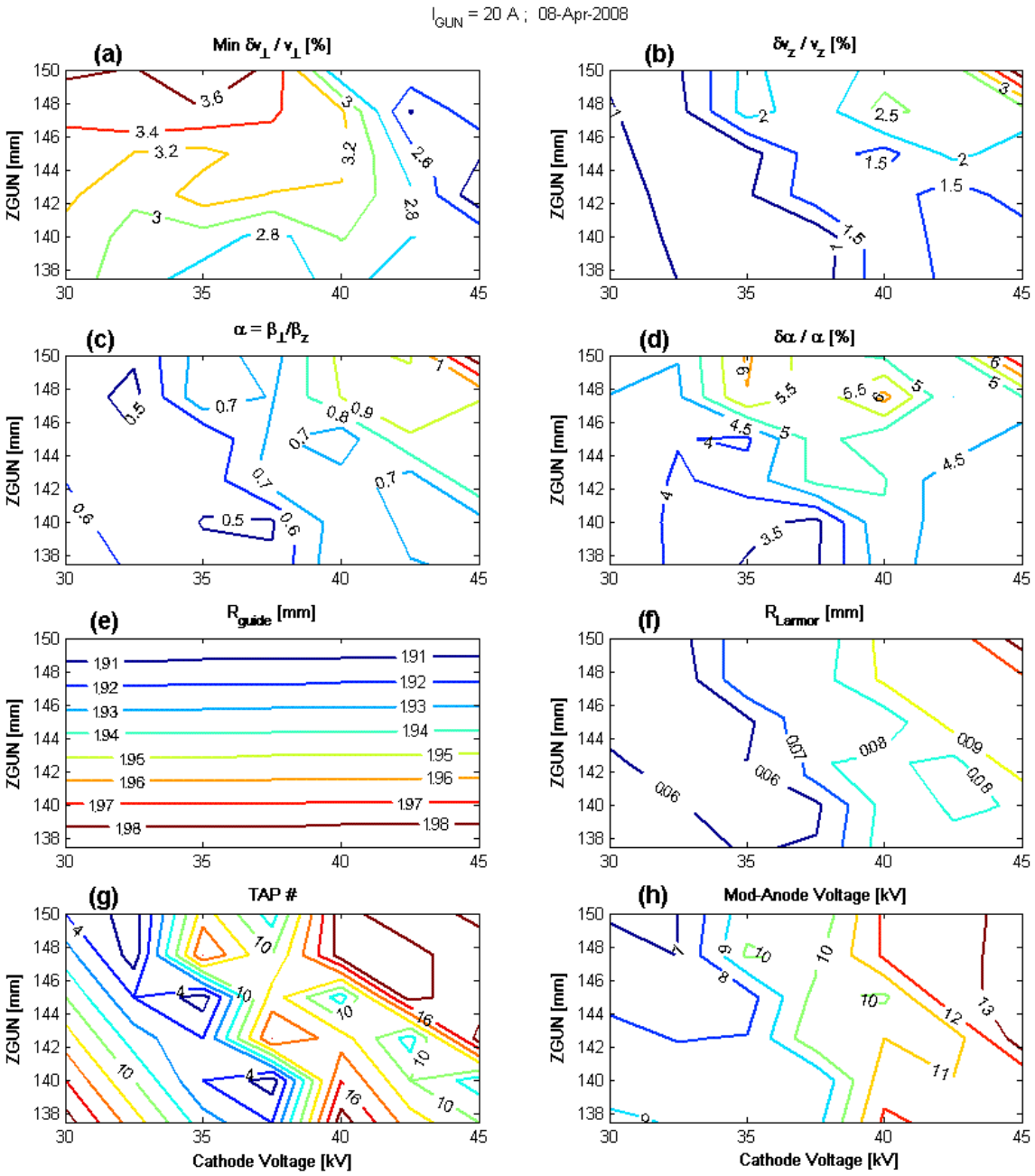

Figure C-4: Gun coil current = +20 A. Contour plots of (a) optimal perpendicular velocity spread, and (b) corresponding parallel velocity spread, (c) alpha value, (d) alpha spread (in percent), (e) guiding center radius, (f) average Larmor radius, (g) Mod-anode voltage Tap number, and (h) corresponding Mod-anode voltage.

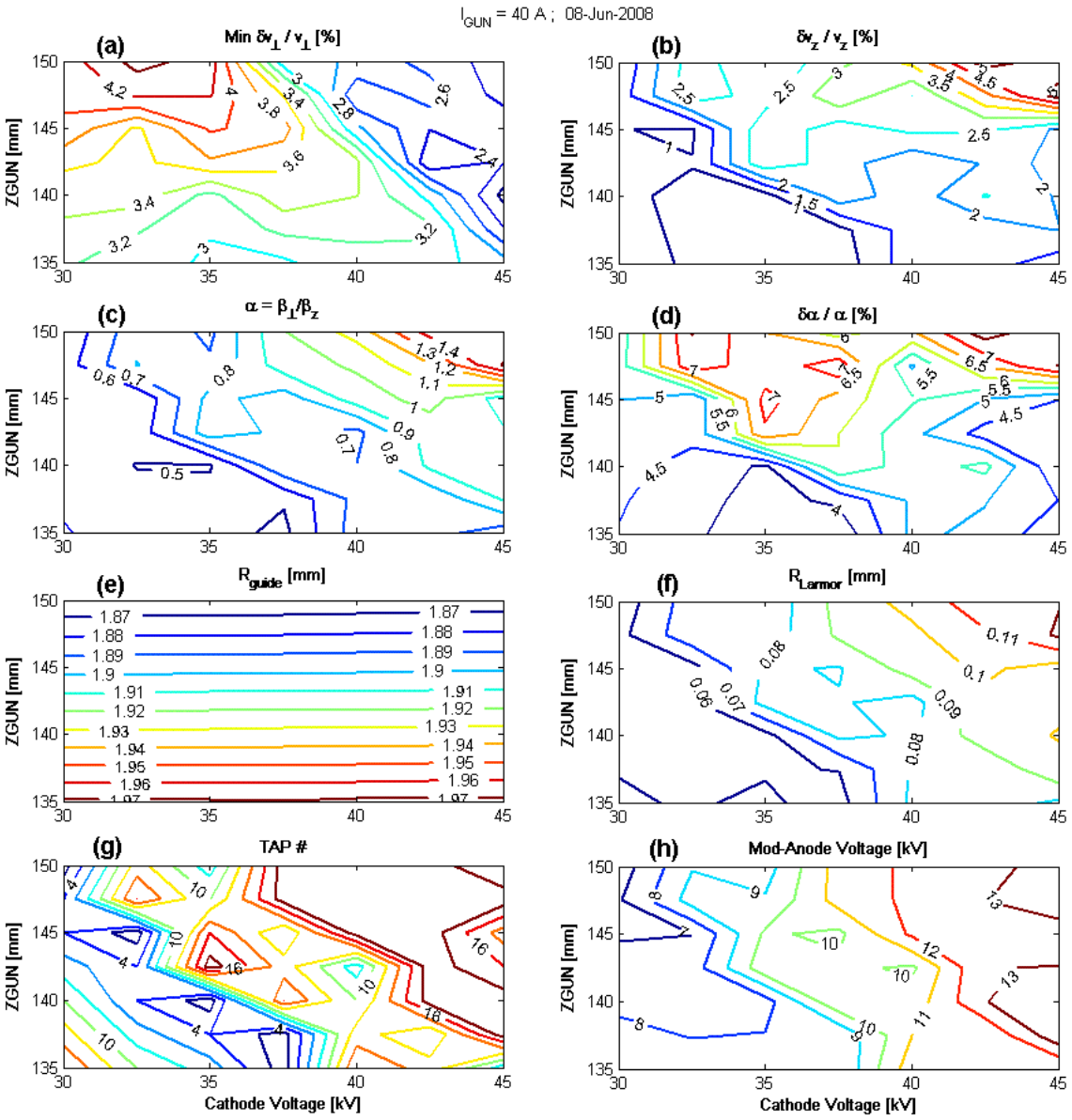

Figure C-5: Gun coil current = +40 A. Contour plots of (a) optimal perpendicular velocity spread, and (b) corresponding parallel velocity spread, (c) alpha value, (d) alpha spread (in percent), (e) guiding center radius, (f) average Larmor radius, (g) Mod-anode voltage Tap number, and (h) corresponding Mod-anode voltage.

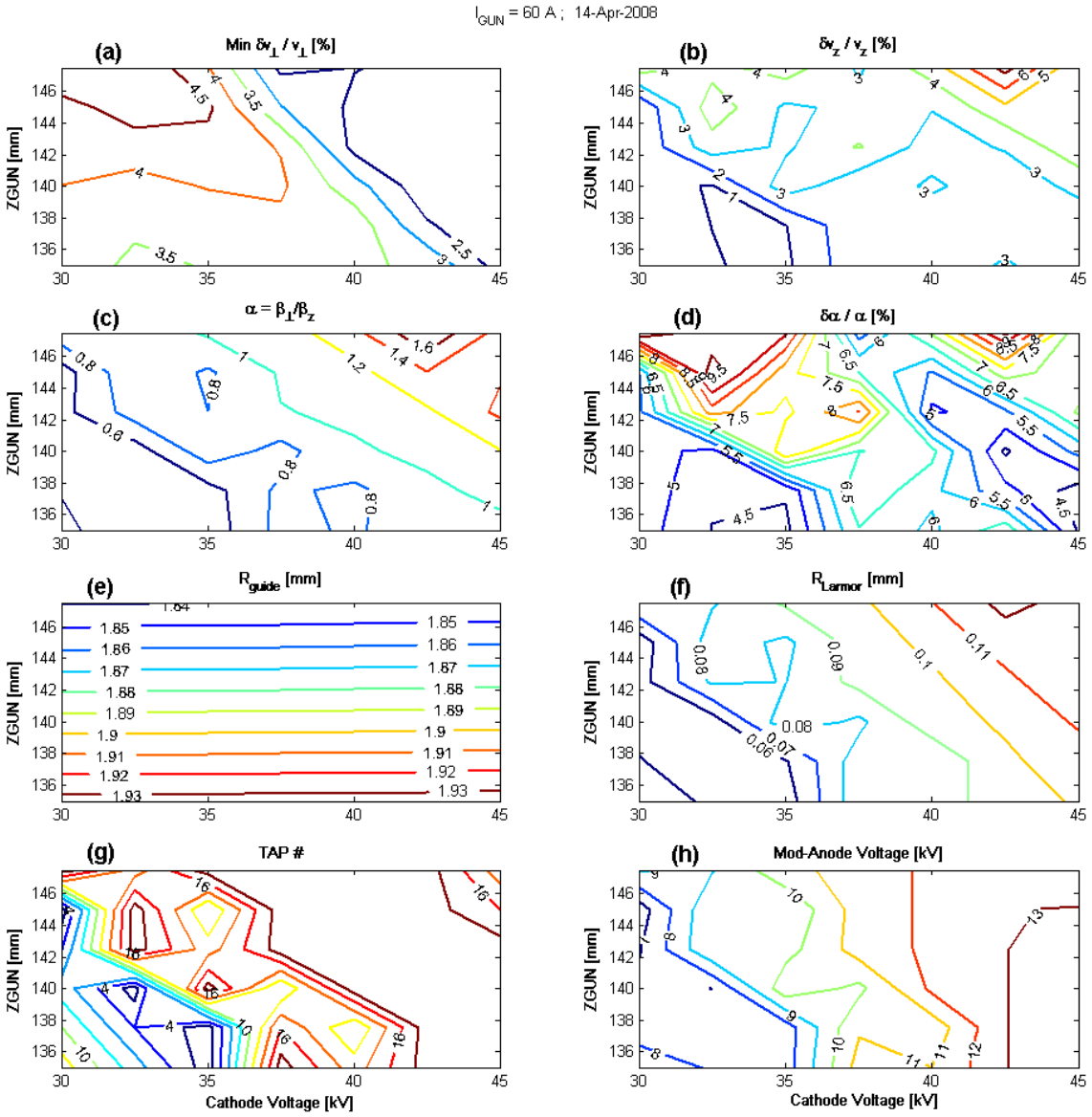

Figure C-6: Gun coil current = +60 A. Contour plots of (a) optimal perpendicular velocity spread, and (b) corresponding parallel velocity spread, (c) alpha value, (d) alpha spread (in percent), (e) guiding center radius, (f) average Larmor radius, (g) Mod-anode voltage Tap number, and (h) corresponding Mod-anode voltage.

References

[1] D. Arnone, C. Ciesla, A. Corchia, S. Egusa, M. Pepper, J. Chamberlain, C. Bezant, E. Linfield, R. Clothier, and N. Khammo, "Applications of terahertz (THz) technology to medical imaging," *Proceedings of the SPIE - The International Society for Optical Engineering*, vol. 3828, pp. 209 – 19, 1999.

[2] C. Longbottom, D. A. Crawley, B. E. Cole, D. D. Arnone, V. P. Wallace, and M. Pepper, "Potential uses of terahertz pulse imaging in dentistry: Caries and erosion detection," *Lasers in Dentistry VIII*, vol. 4610, no. 1, pp. 109–112, 2002.

[3] "Terahertz imaging brings new capabilities to QC applications," *Laser Focus World (USA)*, vol. 41, no. 7, pp. 109 – 12, 2005/07.

[4] N. Karpowicz, H. Zhong, J. Xu, K.-I. Lin, J.-S. Hwang, and X.-C. Zhang, "Non-destructive sub-THz CW imaging," *Terahertz and Gigahertz Electronics and Photonics IV*, vol. 5727, no. 1, pp. 132–142, 2005.

[5] M. Kempkes, T. Hawkey, M. Gaudreau, and R. Phillips, "W-band transmitter upgrade for the Haystack ultra wideband satellite imaging radar (HUSIR)," *2006 IEEE International Vacuum Electronics Conference held jointly with 2006 IEEE International Vacuum Electron Sources (IEEE Cat. No.06EX1278)*, pp. 2–3, 2006.

[6] L-3 Communications, "ProVision: Active Whole-Body Imaging," *Fact sheet: http://www.dsxray.com/pdf/ProVision%5fFactSheetJUN08.pdf, Web page: http://www.dsxray.com/products/mmwave.htm*, 2008.

[7] D. Zimdars, J. White, S. Williamson, and G. Stuk, "High-speed time domain terahertz security imaging," *Proceedings of the SPIE - The International Society for Optical Engineering*, vol. 5790, no. 1, pp. 131 – 6, 2005.

[8] M. Choi, A. Bettermann, and D. van der Weide, "Biological and chemical sensing with electronic THz techniques," *Proceedings of the SPIE - The International Society for Optical Engineering*, vol. 5268, no. 1, pp. 27 – 35, 2003.

[9] W. Menninger, R. Benton, X. Zhai, K. Ching, S. Aldana-Gutierrez, and W. McGeary, "High efficiency, 250 W - 300 W S-band and 100 W K-band traveling wave tubes for satellite communications," *2007 8th IEEE International Vacuum Electronics Conference (IVEC 2007)*, pp. 63 – 4, 2007.

[10] T. Machida, T. Kanamoto, K. Tomikawa, and K. Tsutaki, "Development of Ka-band 500 W peak power helix TWT," *2007 8th IEEE International Vacuum Electronics Conference (IVEC 2007)*, pp. 25 – 6, 2007.

[11] L. Lake, "Millimetric waveband frequency planning," *Electronics and Communication Engineering Journal*, vol. 3, pp. 171–174, Aug 1991.

[12] F. Ulaby, "Absorption in the 220 GHz atmospheric window," *Antennas and Propagation, IEEE Transactions on*, vol. 21, pp. 266–269, Mar 1973.

[13] B. G. Danly, M. Blank, J. P. Calame, S. Cooke, B. Levush, W. Manheimer, A. McCurdy, K. T. Nguyen, D. E. Pershing, J. Petillo, R. K. Parker, T. A. Hargreaves, A. Theiss, R. B. True, K. L. Felch, T. S. Chu, H. Jory, P. Borchard, W. G. Lawson, and T. M. Antonsen, "Development of a W-band gyroklystron for radar applications," *22nd Int. Conf Infrared and Millimeter Waves, VA*, 1997.

[14] K. Mizuno, Y. Wagatsuma, H. Warashina, K. Sawaya, H. Sato, S. Miyanaga, and Y. Yamanaka, "Millimeter-wave imaging technologies and their applications," *2007 8th IEEE International Vacuum Electronics Conference (IVEC 2007)*, pp. 13–14, 2007.

[15] A. V. Gaponov-Grekhov and V. L. Granatstein, *Applications of high-power microwaves*. Boston: Artech House, 1994.

[16] K. L. Felch, B. G. Danly, H. R. Jory, K. E. Kreischer, W. Lawson, B. Levush, and R. J. Temkin, "Characteristics and applications of fast-wave gyrodevices," *Proc. IEEE*, vol. 87, pp. 752–781, 1999.

[17] L. R. Becerra, G. J. Gerfin, R. J. Temkin, D. J. Singel, and R. G. Griffin, "Dynamic nuclear polarization with a cyclotron resonance maser at 5 tesla," *Physical Review Letters*, vol. 71, no. 21, pp. 3561–3564, 1993.

[18] G. Bar, M. Bennati, T. Nguyen, J. Ge, J. Stubbe, and R. G. Griffin, "High frequency (140 GHz) time domain EPR and ENDOR spectroscopy: The tyrosyl radical-diiron cofactor in ribonucleotide reductase from yeast," *Journal of the American Chemical Society*, vol. 123, no. 15, pp. 3569–3576, 2001.

[19] V. S. Bajaj, M. K. Hornstein, K. E. Kreischer, J. R. Sirigiri, P. P. Woskov, M. L. Mak-Jurkauskas, J. Herzfeld, R. J. Temkin, and R. G. Griffin, "250 GHz CW gyrotron oscillator for dynamic nuclear polarization in biological solid state NMR," *Journal of Magnetic Resonance*, vol. 189, no. 2, pp. 251 – 279, 2007.

[20] D. Lewis III, M. A. Imam, A. W. Fliflet, R. W. Bruce, L. K. Kurihara, A. K. Kinkead, M. Lombardi, and S. H. Gold, "Recent advances in microwave and millimeter-wave processing of materials," *Materials Science Forum*, pp. 3249 – 3254, 2007.

[21] T. Tatsukawa, A. Doi, M. Teranaka, H. Takashima, F. Goda, T. Idehara, T. Kanemaki, S. Nishizawa, and T. Namba, "Characteristics of a teflon rod antenna for millimeter- and submillimeter-wave irradiation on living bodies," *Jpn. J. Appl. Phys. 1, Regul. Pap. Short Notes Rev. Pap. (Japan)*, vol. 42, no. 11, pp. 7147 – 7150, 2003.

[22] S. Cauffman, M. Blank, K. Felch, P. Borchard, P. Cahalan, and H. Jory, "Initial testing of a 95 GHz, 2.5 MW gyrotron," *Infrared and Millimeter Waves, 2007*

and the 2007 15th International Conference on Terahertz Electronics. IRMMW-THz. Joint 32nd International Conference on, pp. 94–95, Sept. 2007.

[23] L. Agusu, H. Tsuchiya, H. Mori, T. Idehara, T. Saito, I. Ogawa, and S. Mitsudo, "The experimental results and theoretical analysis of a THz gyrotron using a 21 T pulse magnet at FIR FU," *Eighth IEEE International Vacuum Electronics Conference, Kitakyushu, Japan*, vol. 07EX1526, pp. 1–2, 15-17 May, 2007.

[24] V. L. Granatstein, R. K. Parker, and C. M. Armstrong, "Vacuum electronics at the dawn of the twenty-first century," *Proceedings of the IEEE*, vol. 87, no. 5, pp. 702–716, 1999.

[25] J. Tucek, K. Kreischer, D. Gallagher, and R. Mihailovich, "A compact, high power 0.65 THz source," *Ninth IEEE International Vacuum Electronics Conference, Monterey, CA*, vol. CFP08VAM-PRT, pp. 16–17, April 22-24, 2008.

[26] V. Bratman, V. Gintsburg, Y. Grishin, B. Dumesh, F. Rusin, and A. Fedotov, "Pulsed wideband orotrons of millimeter and submillimeter waves," *Radiophysics and Quantum Electronics*, vol. 49, no. 11, pp. 866 – 71, 2006.

[27] V. Radisic, X. Mei, W. Deal, W. Yoshida, P. Liu, J. Uyeda, M. Barsky, L. Samoska, A. Fung, T. Gaier, and R. Lai, "Demonstration of sub-millimeter wave fundamental oscillators using 35-nm InP HEMT technology," *IEEE Microwave and Wireless Components Letters*, vol. 17, no. 3, pp. 223 – 5, 2007.

[28] C. Tóth, J. van Tilborg, C. G. R. Geddes, G. Fubiani, C. B. Schroeder, E. Esarey, J. Faure, G. Dugan, and W. P. Leemans, "Powerful pulsed THz radiation from laser-accelerated relativistic electron bunches," vol. 5448, pp. 491–504, SPIE, 2004.

[29] T. Maly, G. T. Debelouchina, V. S. Bajaj, K.-N. Hu, C.-G. Joo, M. L. Mak-Jurkauskas, J. R. Sirigiri, P. C. A. Van Der Wel, J. Herzfeld, R. J. Temkin, and R. G. Griffin, "Dynamic nuclear polarization at high magnetic fields," *Journal of Chemical Physics*, vol. 128, no. 5, pp. 052211 –, 2008.

[30] S.-T. Han, R. G. Griffin, K.-N. Hu, C.-G. Joo, C. D. Joye, I. Mastovsky, M. A. Shapiro, J. R. Sirigiri, R. J. Temkin, A. C. Torrezan, and P. P. Woskov, "Continuous-wave submillimeter-wave gyrotrons," *Proceedings of SPIE - The International Society for Optical Engineering*, vol. 6373, pp. 63730 –, 2006.

[31] K.-N. Hu, C. Song, H.-H. Yu, T. M. Swager, and R. G. Griffin, "High-frequency dynamic nuclear polarization using biradicals: A multifrequency EPR lineshape analysis," *The Journal of Chemical Physics*, vol. 128, no. 5, p. 052302, 2008.

[32] V. Bajaj, C. Farrar, M. Hornstein, I. Mastovsky, J. Vieregg, J. Bryant, B. Elena, K. Kreischer, R. Temkin, and R. Griffin, "Dynamic nuclear polarization at 9T using a novel 250 GHz gyrotron microwave source," *Journal of Magnetic Resonance*, vol. 160, no. 2, pp. 85 – 90, 2003.

[33] C. D. Joye, R. G. Griffin, M. K. Hornstein, K.-N. Hu, K. E. Kreischer, M. Rosay, M. A. Shapiro, J. R. Sirigiri, R. J. Temkin, and P. P. Woskov, "Operational characteristics of a 14-W 140-GHz gyrotron for dynamic nuclear polarization," *IEEE Trans. Plasma Sci.*, vol. 34, no. 3, pp. 518–23, 2006.

[34] S.-T. Han, R. G. Griffin, K.-N. Hu, C.-G. Joo, C. D. Joye, J. R. Sirigiri, R. J. Temkin, A. C. Torrezan, and P. P. Woskov, "Spectral characteristics of a 140-ghz long-pulsed gyrotron," *IEEE Transactions on Plasma Science*, vol. 35, no. 3, pp. 559 – 564, 2007.

[35] M. Hornstein, "Design of a 460 GHz second harmonic gyrotron oscillator for use in dynamic nuclear polarization," Master's thesis, Massachusetts Institute of Technology, Elec. Engrg. and Comp. Sci., 2001.

[36] A. C. Torrezan, S.-T. Han, M. A. Shapiro, J. R. Sirigiri, and R. J. Temkin, "CW operation of a tunable 330/460 GHz gyrotron for enhanced nuclear magnetic resonance," *Infrared and Millimeter Waves Conference*, September, 2008. Submitted for publication.

[37] K. E. Kreischer, C. Farrar, R. Griffin, and R. Temkin, "The use of a 250 GHz gyrotron in a DNP/NMR spectrometer," *Proc. 23rd Int. Conf. Infrared Millimeter Waves*, pp. 341–357, 1998.

[38] M. K. Hornstein, V. S. Bajaj, R. G. Griffin, and R. J. Temkin, "Continuous-wave operation of a 460-GHz second harmonic gyrotron oscillator," *IEEE Transactions on Plasma Science*, vol. 34, pp. 524–533, 2006.

[39] M. Hornstein, *A continuous wave second harmonic gyrotron oscillator at 460 GHz.* PhD thesis, Massachusetts Institute of Technology, Elec. Engrg. and Comp. Sci. Dept., 2005.

[40] R. Q. Twiss, "Radiation transfer and the possibility of negative absorption in radio astronomy," *Aust. J. Phys.*, vol. 11, pp. 567–579, 1958.

[41] R. H. Pantell, "Electron beam interaction with fast waves," *Proc. of Symposium on Millimeter Waves, Brooklyn, NY, March 31-April 3*, pp. 301–311, 1959.

[42] A. V. Gaponov and V. K. Yulpatov, "Interaction of electron beams with electromagnetic fields in resonators," *Radiotekhn, I Elektron.*, vol. 7, pp. 631–642, 1962.

[43] V. L. Granatstein, B. Levush, B. G. Danly, and R. K. Parker, "A quarter century of gyrotron research and development," *IEEE Transactions on Plasma Science*, vol. 25, no. 6, pp. 1322–1335, 1997.

[44] M. Blank, B. G. Danly, B. Levush, K. T. Nguyen, D. E. Pershing, K. Felch, B. James, P. Borchard, P. Cahalan, T. Chu, H. Jory, and J. Calame, "Development and demonstration of high-average power w-band gyro-amplifiers for radar applications," *IEEE Transactions on Plasma Science*, vol. 30, no. 3 I, pp. 865 – 875, 2002.

[45] V. Bratman, Y. Kalynov, V. Manuilov, and S. Samsonov, "Submillimeter-wave large-orbit gyrotron," *Radiophysics and Quantum Electronics*, vol. 48, no. 10-11, pp. 731 – 736, 2005.

[46] D. B. McDermott, N. C. Luhmann, Jr., A. Kupiszewski, and H. R. Jory, "Small-signal theory of a large-orbit electron-cyclotron harmonic maser," *Physics of Fluids*, vol. 26, no. 7, pp. 1936–1941, 1983.

[47] V. L. Granatstein and I. Alexeff, *High power microwave sources*. Boston: Artech House, 1987. and references therein.

[48] M. V. Kartikeyan, E. Borie, and M. K. A. Thumm, *Gyrotrons*. New York: Springer, 2004.

[49] K. Felch, M. Blank, P. Borchard, T. S. Chu, J. Feinstein, H. Jory, J. Lorbeck, C. Loring, Y. Mizuhara, J. Neilson, R. Schumacher, and R. Temkin, "Long-pulse and CW tests of a 110-GHz gyrotron with an internal, quasi-optical converter," *Plasma Science, IEEE Transactions on*, vol. 24, no. 3, pp. 558–569, June 1996.

[50] K. E. Kreischer, B. G. Danly, J. B. Schutkeker, and R. J. Temkin, "The design of megawatt gyrotrons," *IEEE Transactions on Plasma Science*, vol. PS-13, no. 6, pp. 364–373, 1985.

[51] K. Koppenburg, A. Arnold, G. Dammertz, H. O. Prinz, M. Thumm, and X. Yang, "Recent results of the step-tunable 105-140 GHz, 1 MW gyrotron development at Forschungszentrum Karlsruhe," *Infrared and Millimeter Waves and 13th International Conference on Terahertz Electronics, 2005. IRMMW-THz 2005. The Joint 30th International Conference on*, vol. 1, pp. 291–292 vol. 1, 19-23 Sept. 2005.

[52] S. Cauffman, "Preliminary design of a 105-140 GHz step-tunable 1 MW gyrotron," *Eighth IEEE International Vacuum Electronics Conference (IVEC 2007), Kitakyushu, Japan*, vol. 07EX1526, pp. 255 – 256, 2007.

[53] K. R. Chu, L. R. Barnett, H. Y. Chen, S. H. Chen, C. Wang, Y. S. Yeh, Y. C. Tsai, T. T. Yang, and T. Y. Dawn, "Stabilizing of absolute instabillities in gyrotron traveling-wave amplifier," *Phys. Rev. Lett.*, vol. 74, pp. 1103–1106, 1995.

[54] M. Garven, J. Calame, B. Danly, K. Nguyen, B. Levush, F. Wood, and D. Pershing, "A gyrotron-traveling-wave tube amplifier experiment with a ceramic loaded interaction region," *IEEE Transactions on Plasma Science*, vol. 30, no. 3, pp. 885 – 893, 2002.

[55] M. Blank, P. Borchard, S. Cauffman, and K. Felch, "Development and demonstration of a broadband W-band gyro-TWT amplifier," *Int. Conf. Infrared and Millimeter Waves Joint with Int. Conf. THz Elec.*, pp. 652–3, 2005.

[56] J. Sirigiri, M. Shapiro, and R. Temkin, "A high power 140 GHz quasioptical gyro-TWT," *IEEE International Conference on Plasma Science*, p. 257, 2003.

[57] J. Sirigiri, *A Novel Wideband Gyrotron Traveling Wave Amplifier*. PhD thesis, Massachusetts Institute of Technology, Elec. Engrg. and Comp. Sci. Dept., 2003.

[58] M. Blank, P. Borchard, S. Cauffman, and K. Felch, "Demonstration of a broadband W-band gyro-TWT amplifier," *Vacuum Electronics Conference, 2006 held Jointly with 2006 IEEE International Vacuum Electron Sources., IEEE International*, pp. 459–460, 25-27 April 2006.

[59] L. Barnett, W. Tsai, H. Hsu, N. Luhmann Jr., C. Chiu, K. Pao, and K. Chu, "140 kW W-band TE01 ultra high gain gyro-TWT amplifier," *2006 IEEE International Vacuum Electronics Conference held jointly with 2006 IEEE International Vacuum Electron Sources, IVEC/IVESC 2006*, pp. 461 – 462, 2006.

[60] V. L. Bratman, G. G. Denisov, S. V. Samsonov, A. W. Cross, A. D. R. Phelps, and W. Xe, "High-efficiency wideband gyro-TWTs and gyro-BWOs with helically corrugated waveguides," *Radiophysics and Quantum Electronics*, vol. 50, no. 2, pp. 95 – 107, 2007.

[61] G. Singh, M. V. Kartikeyan, and G. S. Park, "Gain and bandwidth analysis of a vane-loaded gyro-TWT," *International Journal of Infrared and Millimeter Waves*, vol. 27, no. 3, pp. 333–342, 2006.

[62] G. Park, S. Park, R. Kyser, C. Armstrong, A. Ganguly, and R. Parker, "Broadband operation of a Ka-band tapered gyro-traveling wave amplifier," *Plasma Science, IEEE Transactions on*, vol. 22, no. 5, pp. 536–543, Oct 1994.

[63] L. R. Barnett, J. M. Baird, Y. Y. Lau, K. R. Chu, and V. L. Granatstein, "A high gain single stage gyrotron traveling wave amplifier," *IEDM Tech. Dig.*, pp. 314–317, 1980.

[64] K. R. Chu, H. Y. Chen, C. L. Hung, T. H. Chang, L. R. Barnett, S. H. Chen, and T. T. Yang, "Ultrahigh gain gyrotron traveling-wave amplifier," *Phys. Rev. Lett.*, vol. 81, pp. 4760–4763, 1998.

[65] K. R. Chu, H. Y. Chen, C. L. Hung, T. H. Chang, L. R. Barnett, S. H. Chen, T. T. Yang, and D. Dialetis, "Theory and experiment of ultrahigh gain gyrotron traveling-wave amplifier," *IEEE Trans. Plas. Sci.*, vol. 27, pp. 391–404, 1999.

[66] T. M. Tran, B. G. Danly, K. E. Kreischer, J. B. Schutkeker, and R. J. Temkin, "Optimization of gyroklystron efficiency," *Physics of Fluids*, vol. 29, no. 4, pp. 1274–1281, 1986.

[67] G. S. Nusinovich, B. Levush, and B. Danly, "Gain and bandwidth in stagger-tuned gyroklystrons and gyrotwystrons," *IEEE Transactions on Plasma Science*, vol. 27, no. 2, pp. 422–428, 1999.

[68] G. S. Nusinovich, T. M. Antonsen, Jr., H. Guo, and V. L. Granatstein, "Theory of clustered-cavity gyroklystrons," *Physics of Plasmas*, vol. 9, no. 9, pp. 4032–4039, 2002.

[69] X. Xu, W. Lawson, C. Liu, J. Cheng, B. Hogan, V. L. Granatstein, and M. Reiser, "Design of a new concept cavity for high power gyroklystrons," *IEEE International Conference on Plasma Science*, vol. 3P27, p. 198ff, 1998.

[70] J. D. McNally, D. B. McDermott, Q. S. Wang, F. V. Hartemann, and N. C. Luhmann, Jr., "High performance, 70 kV third-harmonic smooth-bore gyroklystron

amplifier," *IEEE Transactions on Plasma Science*, vol. 22, no. 5, pp. 932–938, 1994.

[71] G. S. Nusinovich, M. T. Walter, M. Kremer, M. E. Read, and D. Boehme, "Submillimeter-wave gyroklystron: theory and design," *IEEE Transactions on Plasma Science*, vol. 28, no. 3, pp. 936–944, 2000.

[72] P. E. Latham, "AC space-charge effects in gyroklystron amplifiers," *IEEE Transactions on Plasma Science*, vol. 18, no. 3, pp. 273–285, 1990.

[73] E. V. Zasypkin, M. A. Moiseev, E. V. Sokolov, and V. K. Yulpatov, "Effect of penultimate cavity position and tuning on three-cavity gyroklystron amplifier performance," *International Journal of Electronics*, vol. 78, no. 2, pp. 423–433, 1995.

[74] G. S. Nusinovich, B. Levush, and B. Danly, "Theory of multi-beam stagger-tuned gyroklystrons," *IEEE Transactions on Plasma Science*, vol. 26, pp. 475–481, 1998.

[75] G. S. Park, V. L. Granatstein, P. E. Latham, C. M. Armstrong, A. K. Ganguly, and S. Y. Park, "Phase stability of gyroklystron amplifier," *IEEE Trans. Plas. Sci.*, vol. 19, no. 4, pp. 632–640, 1991.

[76] M. Blank, P. Cahalan, K. Felch, B. Danly, B. Levush, D. Pershing, K. Nguyen, and J. Calame, "Demonstration of a wide-band 94 GHz gyrotwystron amplifier," *IEEE International Conference on Plasma Science*, p. 256, 2003.

[77] A. Kesar and E. Jerby, "Phase and gain measurements in a distributed-loss cyclotron-resonance maser amplifier," *Physical Review E*, vol. 65, p. 036503ff, 2001.

[78] J. Calame, M. Garven, B. Danly, B. Levush, and K. Nguyen, "Gyrotron-traveling wave-tube circuits based on lossy ceramics," *Electron Devices, IEEE Transactions on*, vol. 49, pp. 1469–1477, Aug 2002.

[79] G. D. Boyd and J. P. Gordon, "Confocal multimode resonator for millimeter through optical wavelength masers," *The Bell System Technical Journal*, vol. 40, pp. 489–508, 1961.

[80] G. D. Boyd and H. Kogelnik, "Generalized confocal resonator theory," *The Bell System Technical Journal*, pp. 1347–1369, July, 1962.

[81] G. S. Nusinovich, *Introduction to the Physics of Gyrotrons*. Baltimore, MD: The Johns Hopkins University Press, 2004.

[82] H. A. Haus, *Waves and Fields in optoelectronics*. Englewood Cliffs, NJ, 07632: Prentice-Hall, 1984. ISBN 0-13-946053-5.

[83] P. Varga and P. Török, "Exact and approximate solutions of Maxwell's equations for a confocal cavity," *Optics Letters*, vol. 21, no. 11, pp. 1523–1525, 1996.

[84] W. Hu, K. E. Kreischer, M. Shapiro, and R. J. Temkin, "Preliminary measurement of a novel 140 GHz gyro-TWT amplifier," *IEEE Conference Record - Abstracts. 1997 IEEE International Conference on Plasma Science*, p. 225, 1997.

[85] T. Nakahara and N. Kurauchi, "Guided beam waves between parallel concave reflectors," *IEEE Trans. on Microwave Theory and Techniques*, vol. MTT-15, no. 2, pp. 66–71, 1967.

[86] G. Gorbau and F. Schwering, "On the guided propagation of electromagnetic wave beams," *IRE Trans. on Antennas and Propagation*, vol. AP-9, pp. 248–156, 1961.

[87] L. A. Weinstein, *Open Resonators and Open Waveguides*. Boulder, CO: The Golem Press, 1969.

[88] R. J. Barker, N. C. Luhmann, J. H. Booske, and G. S. Nusinovich, *Modern Microwave and Millimeter-Wave Power Electronics*. Wiley-IEEE Press, 2005.

[89] High Frequency Structure Simulator (HFSS). Version 11.0, Ansoft Corporation, Pittsburg, PA, 2007.

[90] A. W. Fliflet, "Linear and non-linear theory of the Doppler-shifted cyclotron resonance maser based on TE and TM waveguide modes," *Int. Journ. Electronics*, vol. 61, no. 6, pp. 1049–1080, 1986.

[91] K. R. Chu and A. T. Lin, "Gain and bandwidth of the gyro-TWT and CARM amplifiers," *IEEE Trans. Plas. Sci.*, vol. 16, no. 2, pp. 90–104, 1988.

[92] G. S. Nusinovich and H. Li, "Theory of gyro-travelling-wave tubes at cyclotron harmonics," *Int. Journ. Electronics*, vol. 72, no. 5 and 6, pp. 895–907, 1992.

[93] V. K. Yulpatov, "Nonlinear theory of the interaction between a periodic electron beam and an electromagnetic wave," *Radiophysics and Quantum Electronics*, vol. 10, pp. 471–476, 1967.

[94] G. S. Nusinovich and H. Li, "Large-signal theory of gyro-traveling wave tubes at cyclotron harmonics," *IEEE Transactions on Plasma Science*, vol. 20, no. 3, pp. 170–175, 1992.

[95] O. Dumbrajs and J. P. T. Koponen, "Generalized gyrotron theory with inclusion of electron velocity and energy spreads," *Physics of Plasmas*, vol. 6, no. 6, pp. 2618–2621, 1999.

[96] C. S. Kou, "Starting oscillation conditions for gyrotron backward wave oscillators," *Physics of Plasmas*, vol. 1, no. 9, pp. 3093–3099, 1994.

[97] J. M. Wachtel and E. J. Wachtel, "Backward wave oscillation in the gyrotron," *Appl. Phys. Lett.*, vol. 37, no. 12, pp. 1059–1061, 1980.

[98] S. H. Chen, K. R. Chu, and T. H. Chu, "Saturated behavior of the gyrotron backward-wave oscillator," *Phys. Rev. Lett.*, vol. 85, pp. 2633–2636, 2000.

[99] G. S. Nusinovich and O. Dumbrajs, "Theory of gyro-backward wave oscillators with tapered magnetic field and waveguide cross section," *IEEE Transactions on Plasma Science*, vol. 24, no. 3, pp. 620–629, 1996.

[100] H. R. Johnson, "Backward-wave oscillators," *Proc. of the Inst. of Radio Engineers*, vol. 43, pp. 684–687, 1955.

[101] W. B. Hermannsfeldt, "EGUN - an electron optics and gun design program," Technical report SLAC-331, UC-28, Stanford Linear Accelerator Center, October 1988.

[102] S. E. Tsimring, "On the spread of velocities in helical electron beams," *Radiophysics of Quantum Electronics*, vol. 15, pp. 952–961, 1972.

[103] C. J. Edgecomb, *Gyrotron Oscillators*. Taylor and Francis, Inc., 1993.

[104] M. Born and E. Wolf, *Principles of Optics*. Cambridge University Press, 1999. ISBN: 978-0521642224.

[105] J. A. Kong, *Electromagnetic Wave Theory*. Cambridge, MA, 02139: EMW Publishing, 2000. ISBN 0-9668143-9-8.

[106] W. C. Guss, T. L. Grimm, K. E. Kreischer, J. T. Polevoy, and R. J. Temkin, "Velocity ratio measurements of a gyrotron electron beam," *American Institute of Physics*, vol. 69, no. 7, pp. pp3789–3795, 1991.

[107] Pyrocam III. Model PY-III-C-B, Spiricon Inc., Logan, UT, 2001.

[108] G. G. Denisov, A. N. Kuftin, V. I. Malygin, N. P. Venediftov, D. V. Vinogradov, and V. E. Zapevalov, "110 GHz gyrotron with built-in high-efficiency converter," *International Journal of Electronics*, vol. 72, no. 5, pp. 1079–1091, 1992.

[109] J. Neilson, "Optimal synthesis of quasi-optical launchers for high-power gyrotrons," *IEEE Transactions on Plasma Science*, vol. 34, no. 3, pp. 635–641, 2006.

[110] M. A. Shapiro and S. N. Vlasov, "Study of combined transmission line for high power wave generated by a gyrotron in the millimetre wavelength range," *Int. J. Electronics*, vol. 72, no. 5, pp. 1127–1133, 1992.

[111] K. R. Chu and J. L. Hirshfield, "Comparative study of the axial and azimuthal bunching mechanisms in electromagnetic cyclotron instabilities," *Phys. Fluids*, vol. 21, no. 3, pp. 461–466, 1978.